REPORT DOCUMENTATION PAGE

Form Approved
OMB NO. 0704-0188

Public Reporting burden for this collection of information is estimated to average 1 hour per response, including the time for reviewing instructions, searching existing data sources, gathering and maintaining the data needed, and completing and reviewing the collection of information. Send comment regarding this burden estimates or any other aspect of this collection of information, including suggestions for reducing this burden, to Washington Headquarters Services, Directorate for information Operations and Reports, 1215 Jefferson Davis Highway, Suite 1204, Arlington, VA 22202-4302, and to the Office of Management and Budget, Paperwork Reduction Project (0704-0188,) Washington, DC 20503.

1. AGENCY USE ONLY (Leave Blank)	2. REPORT DATE 3/19/2004	3. REPORT TYPE AND DATES COVERED Final Report, 5/1/2001-1/31/2004

4. TITLE AND SUBTITLE

Assembly of Functional Porous Solids in Complex Hybrid Composites

5. FUNDING NUMBERS

Agreement Number:
DAAD 19-01-1-0512

6. AUTHOR(S)

Andreas Stein, Rick Schroden, Mohammed Al-Daous, Dan Yu, Sergey Sokolov

7. PERFORMING ORGANIZATION NAME(S) AND ADDRESS(ES)

Department of Chemistry, University of Minnesota
139 Smith Hall, 207 Pleasant St. SE, Minneapolis, MN 55455

8. PERFORMING ORGANIZATION REPORT NUMBER

U of M Proposal Number:
100092.32/0109105

9. SPONSORING / MONITORING AGENCY NAME(S) AND ADDRESS(ES)

U. S. Army Research Office
P.O. Box 12211
Research Triangle Park, NC 27709-2211

10. SPONSORING / MONITORING AGENCY REPORT NUMBER

ARO Proposal Number:
41714-CH

° | O

11. SUPPLEMENTARY NOTES

The views, opinions and/or findings contained in this report are those of the author(s) and should not be construed as an official Department of the Army position, policy or decision, unless so designated by other documentation.

12 a. DISTRIBUTION / AVAILABILITY STATEMENT

Approved for public release; distribution unlimited.

12 b. DISTRIBUTION CODE

13. ABSTRACT (Maximum 200 words)

Three-dimensionally ordered macroporous (3DOM) materials with periodic arrays of solid walls possess interesting optical, photonic and reactive properties of interest for camouflage, sensing, sorption, and controlled release. These materials are prepared by colloidal crystal templating techniques. This project was aimed at developing methods for functionalizing 3DOM solids, improving their processibility into shaped structures, forming polymer composites with 3DOM solids, optimizing their optical properties, and evaluating their mechanical properties. Methods were developed for preparing 3DOM oxides and hybrid materials as particles on a multiple gram scale, as supported films, monoliths, and composites with polymers and binders. 3DOM oxides were functionalized with monomeric and polymeric surface groups and with inorganic nanoparticles. 3DOM particles were optimized for optical effects, including tunable colors and control of color intensity. The mechanical properties of the highly porous materials were evaluated by depth sensing indentation, and a parameter was described that allows comparison of mechanical strengths of these materials. Combinations of templating and surface modification methods permitted the preparation of multifunctional systems that combined optical effects with sorption and photocatalytic properties. Other applications that were investigated included adsorption of toxic heavy metals, reactivity of bioactive glass compositions, and a bifunctional catalyst system.

14. SUBJECT TERMS

Colloidal crystal templating, photonic crystals, macroporous solids, pigment, paint, hybrid materials, surface modification, heavy metal sorption, titania, zirconia, silica, alumina, carbon, bioglass, hydrogel, grain size control, nanocomposites, nanoindentation, photooxidation

15. NUMBER OF PAGES

67

16. PRICE CODE

17. SECURITY CLASSIFICATION OR REPORT UNCLASSIFIED	18. SECURITY CLASSIFICATION ON THIS PAGE UNCLASSIFIED	19. SECURITY CLASSIFICATION OF ABSTRACT UNCLASSIFIED	20. LIMITATION OF ABSTRACT UL

NSN 7540-01-280-5500

Standard Form 298 (Rev.2-89)
Prescribed by ANSI Std. 239-18
298-102

Enclosure 1

Assembly of Functional Porous Solids in Complex Hybrid Composites

Final Report

Andreas Stein

University of Minnesota

April 2, 2004

Table of Contents

List of Tables

List of Figures

1. Introduction

In the last few years a number of methods have been developed to structure materials with periodic features on a submicrometer scale ("photonic crystals"), allowing them to interact strongly with visible light. Modulation of the dielectric constant of the structure causes multiple interferences between waves scattered from each unit cell. As a result, materials that are normally white can exhibit tunable colors. Under relatively stringent conditions, photonic crystals exhibit photonic bandgaps (PBG)—a range of frequencies where no propagation of electromagnetic waves occurs in any direction—properties of interest for optical waveguides and microcavity lasers.[1-6] To develop a PBG, a material requires a specific geometry, a high refractive index contrast in the periodic features, and near perfection in the positioning and uniformity of its components. Optical filtering effects of interest in the preparation of *photonic crystal pigments* (PCPs) for potential camouflage applications are much less demanding.

Suitable materials can be prepared by chemical syntheses relatively easily and economically, using a process called colloidal crystal templating to produce three-dimensionally ordered macroporous (3DOM) solids.[7,8] In this method, colloidal crystals are formed by assembling uniform spheres (polymer latex spheres or silica spheres a few hundred nanometers in diameter) into close-packed arrays, which resemble natural opals in structure.[9-38] The interstitial space between the spheres is then filled by a fluid that is subsequently converted into a solid skeleton (Figure 1). Solidification may occur by precipitation, sol-gel chemistry, polymerization, chemical conversion, and other suitable methods. In a final step, the spheres are removed, typically creating interconnected voids where the spheres were originally located and a solid skeleton in the location of the former interstitial spaces. The resulting structures can therefore be regarded as inverse replicas of the template array, or inverse opals. They consist of inorganic, organic, or hybrid walls that surround periodic arrays of voids with uniform diameters in the range of a few hundred nanometers. This colloidal crystal templating approach is very general and can be applied to produce a large number of inorganic, polymeric and hybrid compositions.[14-18,35,36,39-74]

Infiltrate Process

Colloidal Crystal "Opal"

3-Dimensionally Ordered Macroporous Solid "Inverse Opal"
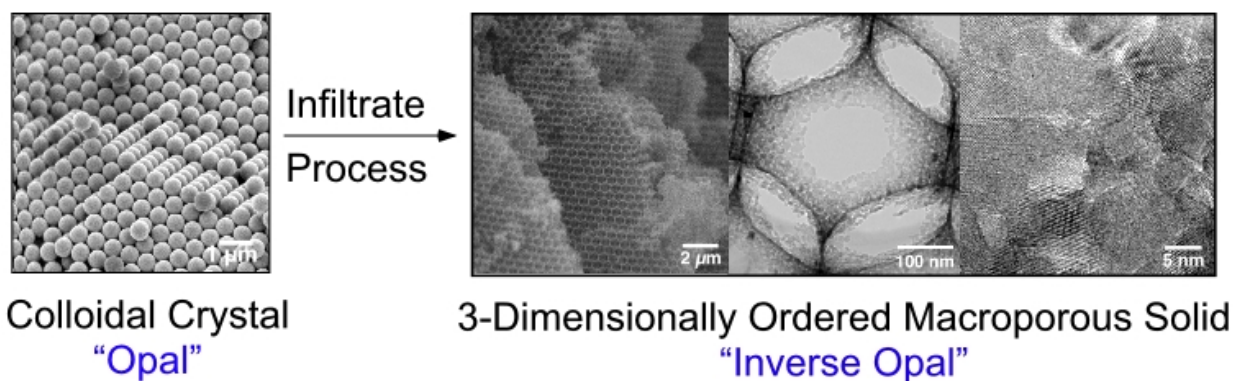
Figure 1. From left to right: SEM images of a colloidal crystal of polymer latex spheres, calcined 3DOM titania, and TEM images of 3DOM titania showing one macropore and the nanograins which form the wall skeleton.

2. Relevance to Army

The foreseen benefits of *photonic crystal pigments* (PCPs) for the army relate to optical and thermal camouflage of soldiers, equipment and infrastructure. Particular advantages are expected for shielding of radiative heat-emitting sources, which include the soldier's body heat, electronic gear, combustion engines, etc. PCPs possess several advantages over traditional pigments, including the possibility of tuning their optical absorptions (colors) over most of the UV-visible-near IR-IR range during pigment synthesis. Such materials may absorb, for example in the infrared region to prohibit heat transfer, while being translucent in the visible region, providing heat-shading without darkening the environment. Colors may vary with the angle of the viewer. PCPs can be obtained without using any toxic heavy metals, which are present in many inorganic pigments. Inorganic PCPs can have high heat stability, chemical stability, weather resistance and little reactivity. In the case of three-dimensional (3D) PCPs, based on 3D ordered macroporous (3DOM) solids, it is possible to modify pigment colors dynamically by filling pores with fluids that alter the refractive index contrast throughout the pigment, or if applicable, by deforming the pigment. This can allow adaptive chameleon-type camouflage. The porous structure permits breathability if it is incorporated in clothing materials. Furthermore, the pigment composition is very flexible, permitting incorporation of multifunctionality in the material. For example, suitable surface functionalization of the porous pigment can facilitate sorption of toxic substances, which may further lead to a change in color. If a photooxidation catalyst is incorporated in the pigment, it can promote photodecomposition of toxins or pollutants. Electronically conducting PCP compositions are possible, which may add electromagnetic shielding capabilities to thermal shielding. In composite form, 3DOM PCPs may ultimately be incorporated in soldiers' protective clothing or surfaces of equipment to impart these materials with "smart" properties and multifunctionality (variable visual appearance, camouflage or optical signature modification, detection of chemical or biological agents that alter optical properties of the material upon adsorption, drug release with concurrent color changes, detection of structural failure, absorption/degradation of hazardous materials, power sources in the clothing, thermal insulation, etc.).

3. Accomplishments during the funding period covered in this report:
- We developed methods for preparing 3DOM oxides and hybrid materials as particles on a multiple gram scale, as supported films, monolithic forms and composites with polymers and binders.
- We developed a range of methods to functionalize 3DOM materials with inorganic and organic surface groups. Surface groups provide anchors for additional functionalization and for attachment of polymer strands. They also permit adjustment of the wall thickness, porosity and strength, as well as adjustment of surface and bulk properties.
- We examined several strategies for forming polymer composites with 3DOM particles.
- We optimized 3DOM materials for non-PBG optical effects, including tunable colors, refractive index-control through phase selection and organic/inorganic modification, control of color intensity through processing and formation of composites, and paint formation by processing 3DOM pigments of various particle sizes with binders. These properties are important in potential applications of 3DOM materials as responsive pigments, which can change colors upon interactions with guest substances occupying the pores, and also for non-responsive, non-toxic pigments of tunable colors, some of which

are difficult to achieve in the absence of potentially toxic components (e.g., certain transition metals).

- We developed methods to test the mechanical properties of the highly porous materials by depth sensing indentation and described a parameter that allows comparison of mechanical strength in these materials.
- We investigated structure-property relationships of these complex structures, with an emphasis on optical, mechanical, sorption, release, bioactivity, and catalytic/ photocatalytic properties. These properties were affected by composition and surface functionalization of the 3DOM structure, the wall texture, presence of specific crystallographic phases, surface area, and pore sizes.

Results are summarized below briefly for work that has now been published or submitted for publication and in a little more detail for unpublished work.

4. Synthesis of 3DOM materials

The general synthesis of 3DOM materials by colloidal crystal templating has been outlined in the introduction. A large variety of strategies exist, based on sol-gel chemistry, polymerization, salt-precipitation and chemical conversion, chemical vapor deposition, spray pyrolysis, ion spraying, laser spraying, nanocrystal deposition and sintering, oxide and salt reduction, electrodeposition, electroless deposition, fabrication from core-shell spheres, and patterning techniques. These are outlined in an extensive review paper by Schroden and Stein.[75] We focussed mainly on titania, zirconia, silica and hybrid-organosilica compositions, all of which are wide-bandgap materials and are white in nontemplated bulk form. We have developed methods to produce these 3DOM materials on a multiple gram scale with controllable crystallographic phases (TiO_2: amorphous, anatase, rutile; ZrO_2: tetragonal, monoclinic;[76] SiO_2: amorphous, mesoporous, zeolitic[48,77]). In principle, the steps involved in the preparation of functional 3DOM materials can be scaled up to much larger amounts.

Two new 3DOM compositions were also prepared: 3DOM α-alumina, and 3DOM γ-lithium aluminate.[78,79] The α-alumina material combines the thermal and chemical stability of the corundum phase with a very open structure of uniform macropores that can permit facile transport of guest molecules in potential catalysis, filtration, and sensing applications; while γ-lithium aluminate exhibits good thermochemical and irradiation stability, making it a potential candidate in molten carbonate fuel cells and tritium-breeding blankets in fusion reactors. Details about preparations and characterization of these materials have been published.[78,79]

4.1 Thin film growth of 3DOM solids

Thin film morphologies of 3DOM materials are desirable for testing the mechanical properties of these materials by nanoindentation techniques, as well as for various applications. We have employed two methods for deposition of colloidal crystal templates and 3DOM precursors, a blade deposition technique which permits rapid deposition, and an evaporation technique on slanted substrates, which produces more ordered products.

Thin films of 3DOM silica, alumina and other metal oxides were prepared by blade deposition methods (Figure 2). An uncoated or Pt-coated glass or quartz microscope slide was placed on a silicon wafer and a "smearing" knife with an adjustable slit width (GARDCO) was placed above the slide. A drop of a latex sphere suspension was placed in front of the blade, and the knife was

dragged across the slide at a constant speed to spread the suspension on the slide surface. Air drying resulted in ordering of the spheres. Typical layer thicknesses of ca. 6-10 sphere layers were obtained. After brief annealing of the thin films, a precursor solution for the inorganic 3DOM material was applied by the same blade deposition method and the slide was processed as in the preparation of bulk materials. The procedures were optimized by varying the slit width between knife and surface, dragging rates, precursor concentrations, solvents and additives (such as wetting agents). A typical film of 3DOM $LiNiO_2$ is shown in Figure 2. One can see multiple layers of pores, as well as some defects and cracks. The crack density and width appears to be a function of the calcination temperature. Even though the resulting films are less perfect than those obtained by vertical deposition methods, the technique is significantly faster, and films are suitable for testing of the preparation/templating chemistry, the mechanical properties of the films, as well as for a range of applications that do not require perfect periodicity.
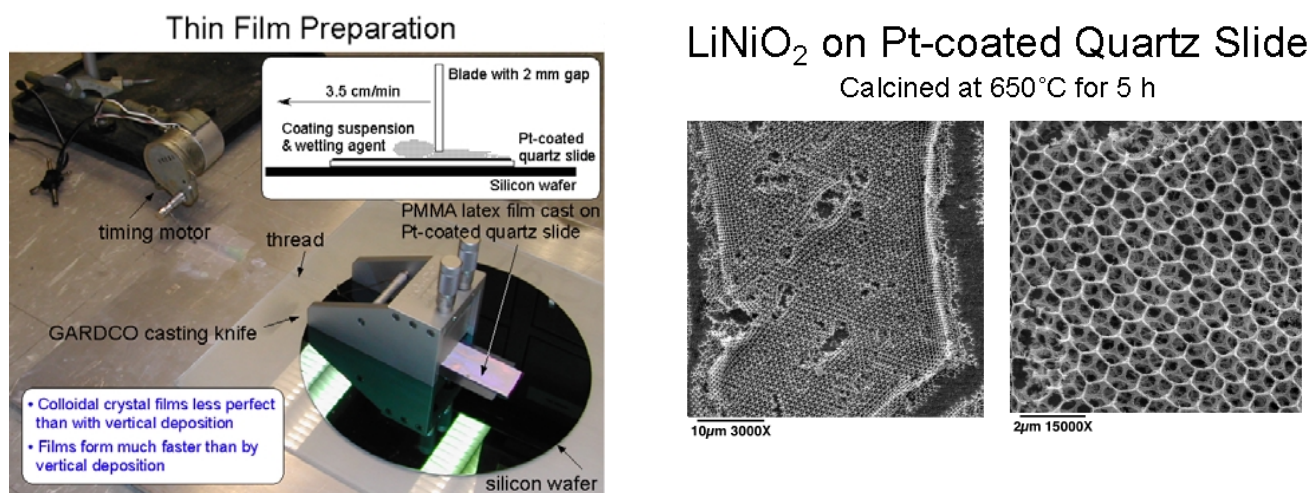
Figure 2. Left: diagram showing the equipment for blade deposition of thin films. Right: SEM images of calcined $LiNO_2$ thin films prepared by blade deposition.

While the blade deposition technique allowed for rapid formation of 3DOM films, it had a number of disadvantages, including partially reduced order in the structure and the presence of significant "mud-cracks" after processing. For applications requiring greater order, we adopted another technique for thin-film formation, a modification of the vertical deposition technique described by Colvin et al.[34] A slanted deposition method proved to be advantageous for our samples, a technique in which colloidal crystal films were grown on a planar substrate positioned at an angle in a colloidal dispersion (see Figure 3). As the colloidal dispersion evaporated under controlled temperature conditions, uniform films of close-packed spheres were deposited. These were then infiltrated with precursors for the 3DOM solid and processed as in the blade deposition methods. The resulting structures were much more ordered than those produced with blade deposition (see an example in Figure 4). However, mud-cracks were still present; these were introduced during calcination, as the thin films shrunk.

9
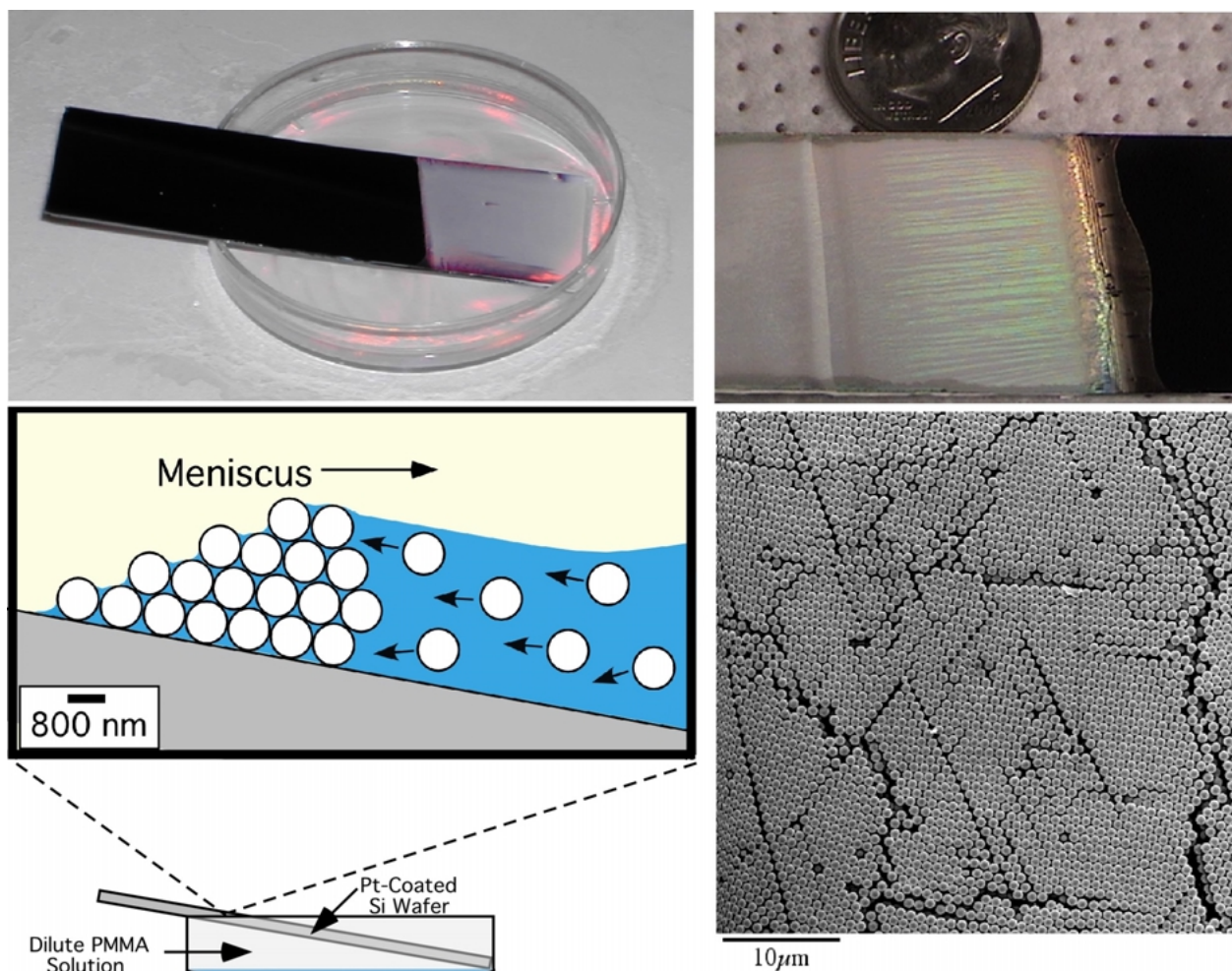
Figure 3. Images showing the preparation of silica colloidal crystal films by slanted deposition techniques. A petri dish containing an ethanol suspension of 460 nm diameter silica spheres (2 wt% silica) was set on a hot plate controlled at 40 ˚C. A Si wafer or glass slide (uncoated or Pt-coated) was placed on the edge of the dish so that it was partly immersed in the sphere suspension at an angle of ca. 10˚. As the suspension slowly evaporated, an ordered colloidal crystal film deposited on the substrate. The supported thin films were opalescent to the eye. However, SEM images showed defects surrounding ordered regions 10s of μm in size.
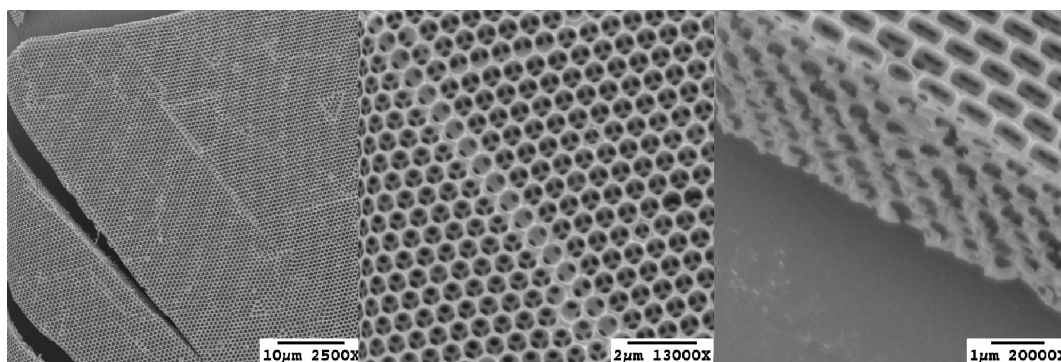
Figure 4. SEM images of a thin film of 3DOM SnO₂, prepared by slanted deposition on Pt-coated silicon substrates.

4.2 Synthesis of 3DOM carbon monoliths

We have been able to prepare non-graphitizable, amorphous 3DOM carbon monoliths from carbonized resorcinol-formaldehyde sol, using chemistry similar to that used for templating mesoporous carbon[69,80-84] combined with PMMA sphere templating. These particles, an example of which is shown in Figure 5, are well ordered and hence colored. They are mechanically more robust and exhibit much less cracking than 3DOM oxides.
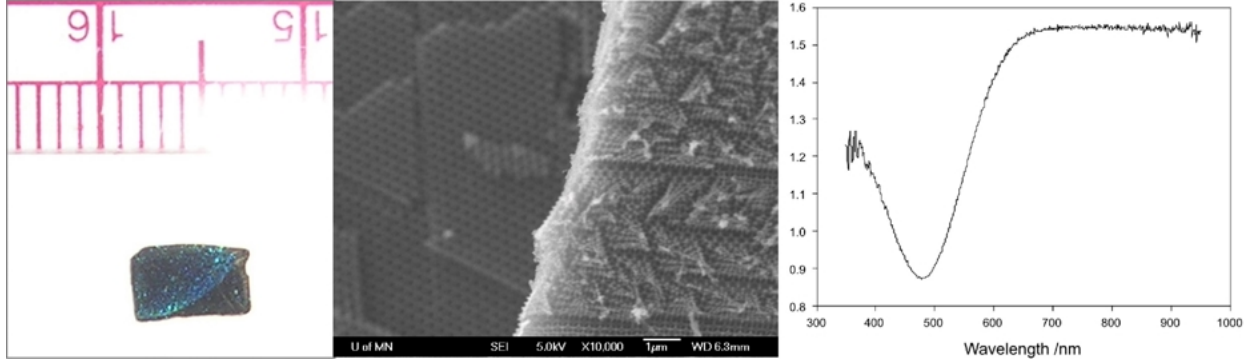
Figure 5. Left: photograph of millimeter-sized 3DOM carbon monolith. Center: SEM image of this particle. Right: UV-visible spectrum showing the stop-band of this particle.

5. Optical properties of 3DOM materials

5.1 Tunable colors

The color of 3DOM solids is a function of the pore size (controlled by the choice of template dimensions), refractive index of the walls (controlled through composition), refractive index of the substance occupying the pores (controlled through pore filling, e.g. with various solvents), and the thickness of the walls (established during the synthesis or by post-synthesis wall modification). For light reflected perpendicularly to a powdered 3DOM sample, relationships between the absorption wavelength and these parameters can be approximated by combining Bragg's law with Snell's law according to:

$$\lambda = \frac{2d_{hkl}}{m}[\phi n_{walls} + (1-\phi)n_{voids}]$$

or by invoking dynamic diffraction theory to give:

$$\lambda = \frac{2d_{hkl}}{m}[\phi n_{walls} + (1-\phi)n_{voids}]\left(1+\frac{\psi}{2}\right)$$

Here λ is the wavelength of the stop band (optical reflection) minimum, d_{hkl} the interplanar spacing, m the order of Bragg diffraction, ϕ the solid fraction of the material (related to wall thickness), n_{walls} the refractive index of the wall material, n_{voids} the refractive index of the substance occupying the voids, $\psi = 3\phi(r^2-1)/(r^2+2)$, and $r = n_{walls}/n_{voids}$.[8]

Normally, one to two stop bands are observed for powder 3DOM samples in the UV-visible range. However, under appropriate conditions more bands can be seen. Figure 6 shows the diffuse-reflectance UV-vis spectrum of a powdered sample of 3DOM mercaptopropyl silica filled with 2-propanol. This polycrystalline photonic crystal exhibits stop bands corresponding to the (111), (200), (220), and (311) sets of planes. The spectrum is analogous to a powder X-ray diffraction pattern for materials with periodicity on an atomic scale (i.e., crystalline materials). Figure 7 shows the effect of pore size on color of 3DOM titania samples and Figure 8 effects of pores size and pore filling with solvents for 3DOM zirconia powders.

11
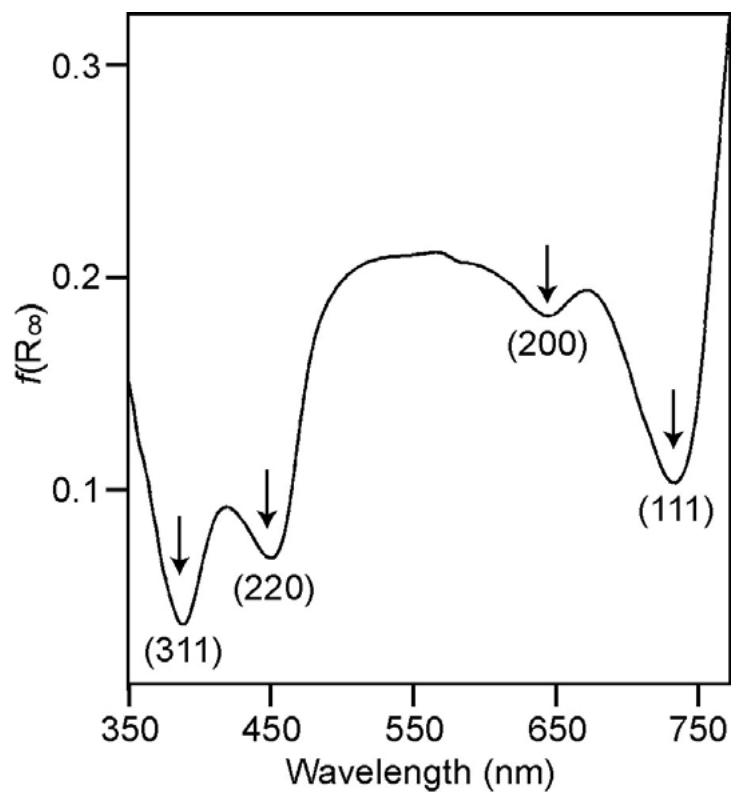
Figure 6. Diffuse-reflectance UV-vis spectrum of 3DOM mercaptopropyl silica filled with 2-propanol.

3DOM Titania

S = 250 nm, M = 310 nm, L = 375 nm, XL = 425 nm diameter
PMMA spheres as template

Figure 7. Vials containing 3DOM titania (anatase), obtained with spheres of increasing size (clockwise, starting at S). The samples in the middle are sample S/M filled with methanol or toluene. Note that bulk titania is white.

Inorganic Pigments

Figure 8. Colors of 3DOM ZrO_2 compared to industrial pigments. The three 3DOM ZrO_2 samples on the bottom left have increasingly larger pore sizes. The pore sizes depend on the size of the PMMA latex spheres used as templates. The two samples on the right correspond to the first two, filled with ethanol.

5.2 Refractive index tuning through organic functionalization

The colors of the materials can be tuned over wide ranges of the spectrum by filling pores with solvents of various refractive index. To vary the refractive index of the walls we investigated modifications of silica walls with organic functional groups, such as mercaptopropyl groups, using mixed silica precursors (tetramethoxysilane and mercaptopropyl trimethoxysilane). Variation of the effective refractive index of the walls in these samples over more than 0.1 refractive index units was possible by incorporating between 0–10 wt% sulfur in these samples, as shown in Figure 9. Because surface functional groups can interact with specific guest molecules, which can also modify the effective refractive index of the walls, refractive index tuning through host-guest interactions may be employed in sensing applications.
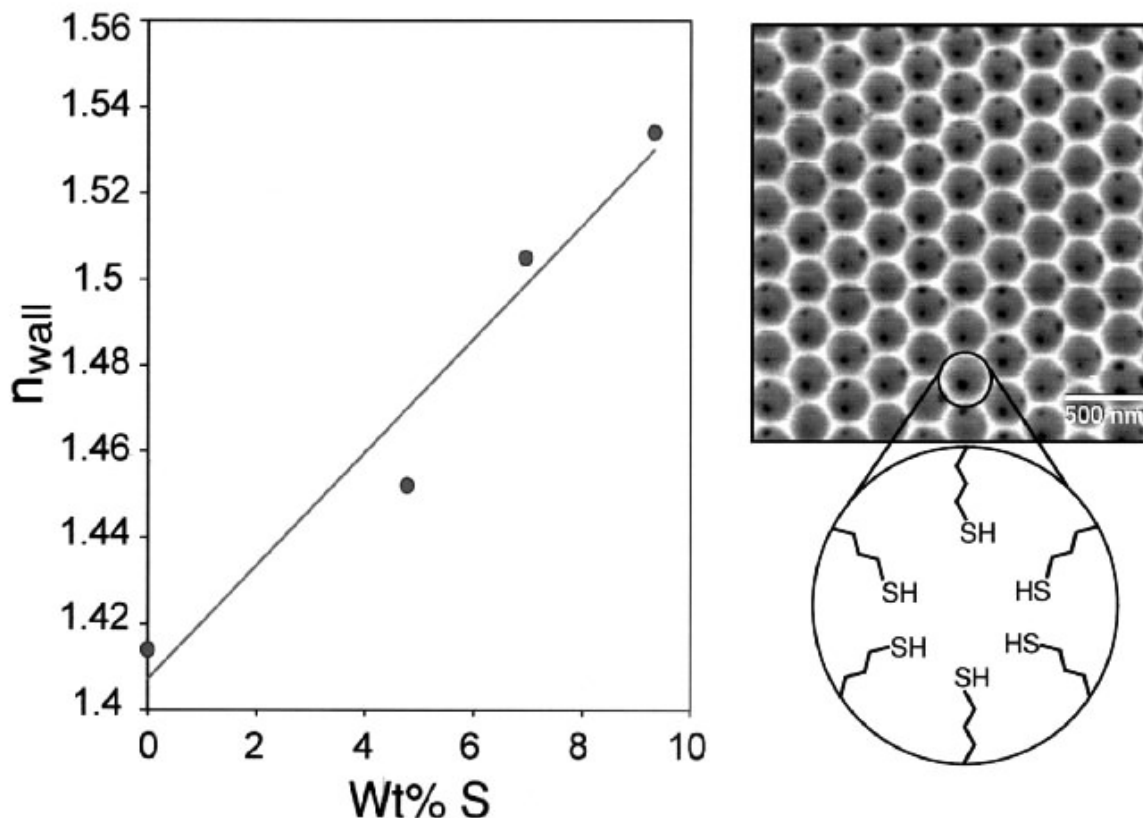
Figure 9. Plot of effective refractive index of the walls for 3DOM mercaptopropyl silica prepared with various loadings of sulfur. An SEM of one of these samples and a schematic illustrating the functionalization of the silica walls are also shown.

5.3 Refractive index control through composite formation (3DOM-polymer/titania nano-composites)

Because of their greater processibility and flexibility, 3DOM polymers provide an attractive alternative to inorganic 3DOM materials. Templated 3DOM films and sheets can be formed with polymers.[35,36,68-70] However, optical applications are limited in part by the relatively low refractive index of polymers. To enhance the refractive index contrast in a polystyrene-based 3DOM film, we incorporated preformed titania nanoparticles in the film. The nanoparticles were modified with organic sulfonate surface groups to permit dispersion in PS/toluene solutions. Figure 10 shows the UV-visible absorption spectrum of the toluene/polystyrene solution containing the surface-stabilized titania nanoparticles. The absorption edge due to the titania nanoparticles is observed.
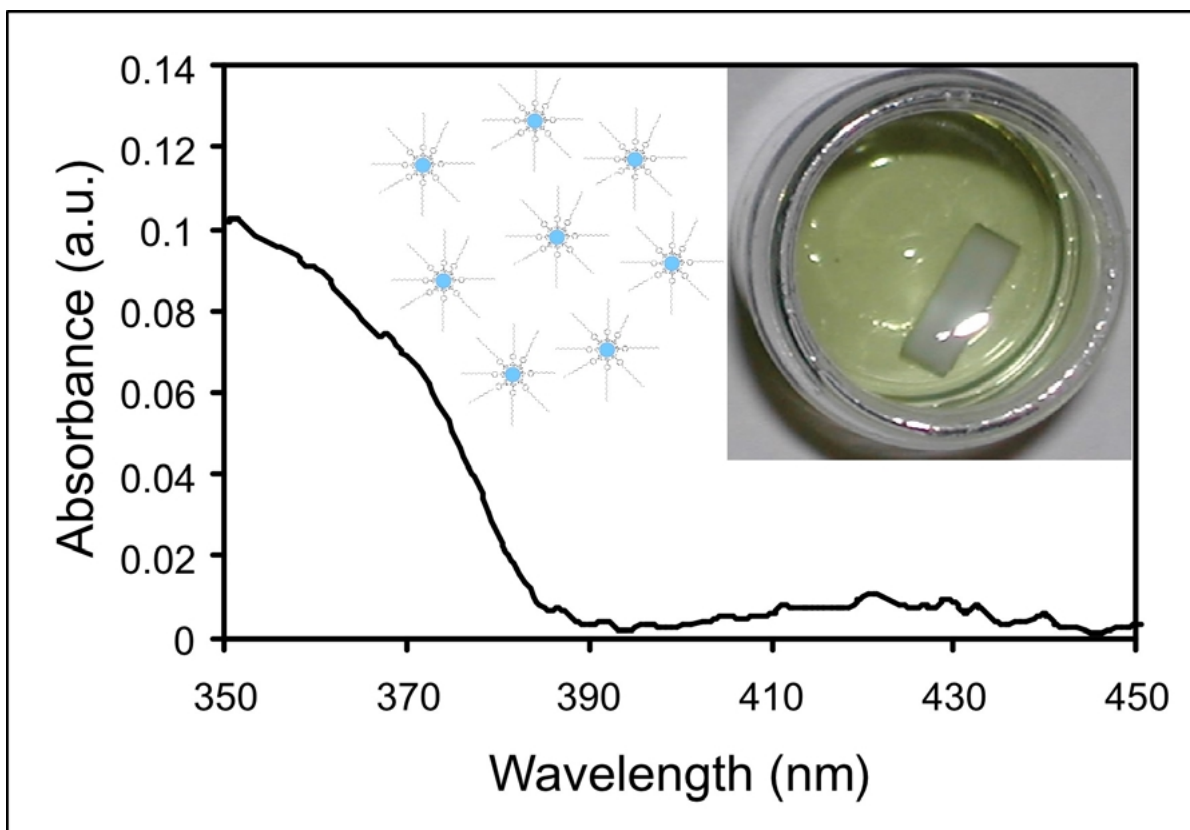
Figure 10. UV-vis spectrum of a toluene/polystyrene solution containing titania nanoparticles whose surface were stabilized with dodecylbenzenesulfonic acid. The inset shows a photograph of this solution. (TiO$_2$ nanoparticles were synthesized by adding 14 mL TiCl$_4$ dropwise to an ice-cold solution of 14 ml 37% HCl in 350 mL H$_2$O. After complete addition, the solution was heated to 60 ˚C and aged for 60 min at that temperature; then 0.7 mL dodecylbenzenesulfonic acid (DBSA) was added to avoid further particle growth. The coated nanoparticles were extracted into dichloromethane. The solution was concentrated by rotary evaporation, forming a yellow gel. The gel was then dried in air under ambient conditions to form a yellow powder (14.5 wt% titania, based on TGA, no XRD reflections). The yield of titania nanoparticles: ca. 2% after drying (based on product mass and corrected for titania content in product calculated from TGA data).)

Figure 11 shows the UV-visible absorption spectrum of the infiltrated and partially extracted colloidal crystal. The titania absorption edge is still present, confirming the incorporation of titania nanoparticles in the material, in agreement with the observations of nanoparticles in the TEM image of the wall skeleton (Figure 12). A stop band is not seen in this particular sample, because extraction of silica spheres was only partial as indicated in the SEM images shown in Figure 12. Nonetheless, the periodic structure of the nanocomposite is clearly visible. We are continuing to improve extraction methods to remove the silica spheres more completely. We plan to optimize dispersion conditions to increase the TiO$_2$ loading to higher values than we have achieved to this point and expect similar color intensities as for the TiO$_2$-modified 3DOM SiO$_2$ samples, with the advantage of better processability than for silica.
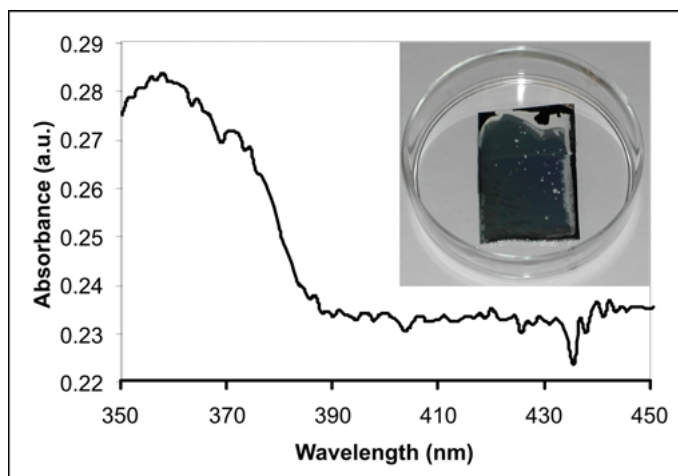
Figure 11. UV-vis spectrum of thin 3DOM polystyrene film containing ca. 5 wt% titania nanoparticles. (A dry silica colloidal crystal film on a planar substrate was infiltrated dropwise with a solution containing 0.04 g polystyrene (PS, M_w = 230,000) and 0.02 g coated TiO_2 nanoparticles in 10 mL toluene. The resulting film was dried in air at 25 ˚C for 12 h. The silica template was removed by multiple treatments in which the film was immersed in 8% aqueous HF solution for ca. 3 minutes at a time. The product was carefully washed with water and dried in air for 24 h.)
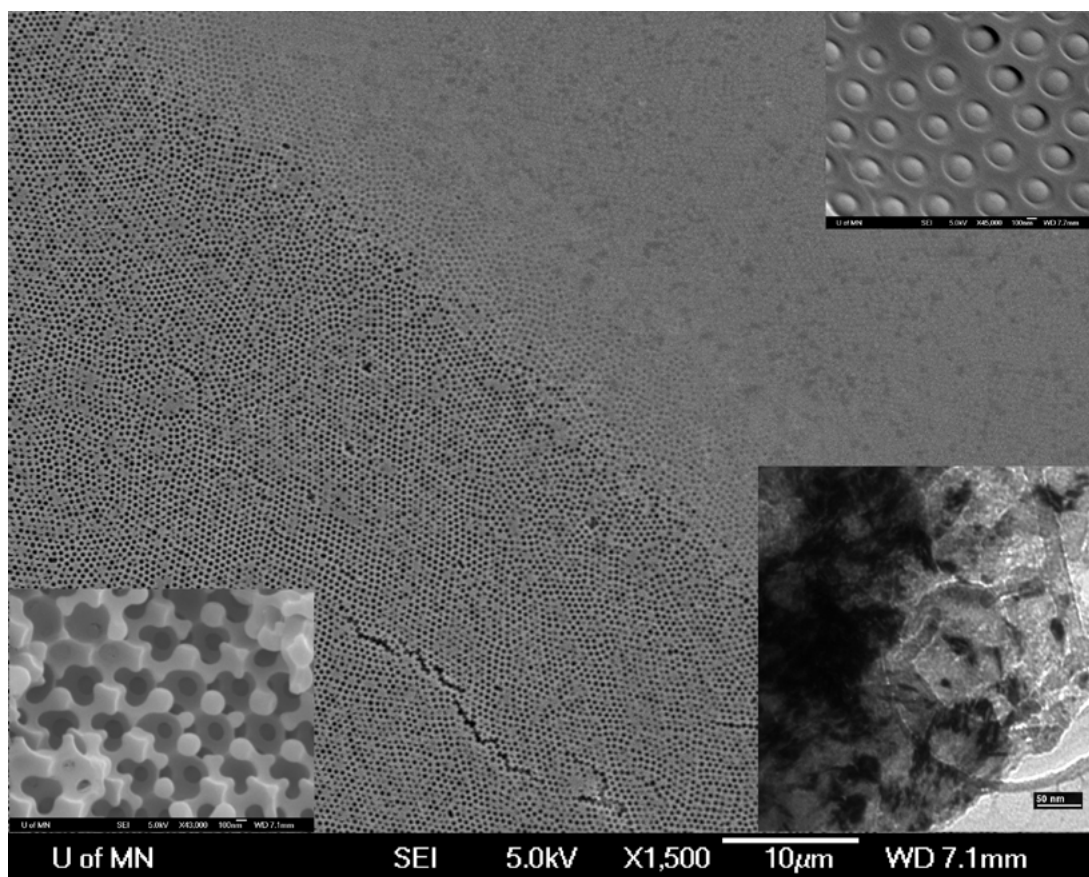
Figure 12. SEM image of a 3DOM polystyrene/titania nanocomposite film after partial extraction of the silica template with an aqueous HF solution. The "smoother" area on the upper right is incompletely extracted, and the SEM image of that region (inset) shows that silica spheres are still present. The porous area on the lower left consists of interconnected macropores without the templating spheres (inset). The inset on the bottom right is a TEM image of the skeletal wall. Darker spots arise from the titania nanoparticles dispersed in the polymer matrix.

5.4 Refractive index optimization through phase control

As noted earlier, photonic band gap materials require high refractive indices in the walls. Titania exhibits one of the highest refractive indices among oxides which are transparent in the visible range. (Many semiconductor materials have even higher refractive indices, but they absorb strongly in the visible.) 3DOM titania is most readily synthesized in the form of anatase, a phase with an average bulk refractive index of 2.55. It has been demonstrated that 3DOM anatase does not form a full PBG, but stop bands extend over 55% of the full solid angle, i.e., the propagation of selected wavelengths of light is only partially inhibited.[85] The average bulk refractive index of rutile is higher, 2.76,[86] and at a wavelength of 500 nm approaches a value of 3.0, potentially high enough to achieve a PBG. It has been difficult to form 3DOM rutile by a thermal transformation of 3DOM anatase, because this phase transformation is associated with excessive grain growth which leads to loss of the periodic structure. We have developed several methods to obtain 3DOM rutile using appropriate precursors and employing rutilizing agents to reduce the phase transformation temperature and inhibit grain growth.

In general, it is known that amorphous TiO_2 crystallizes into anatase below 400 °C, which is further converted to rutile at temperatures in the range from 600 to 1100 °C.[87] The rate of this transformation is markedly influenced by particle size or the presence of impurities. Yoldas reported that reducing the extent of hydrolytic polycondensation of the titanium alkoxide might lower the anatase-rutile conversion temperature.[88] That is, the smaller the initial size of particles undergoing transformation the lower the required transformation temperature. One of the possible ways to inhibit the condensation reaction of titanium alkoxides is through the addition of inorganic acids, the simplest of which are protons.[88] In addition, for a given hydrolysis catalyst, the concentration and stabilization of the different titania phases might also be affected by doping the sol with oxides or oxide precursors.[89] For example, when titania is prepared with hydrochloric acid as a hydrolysis catalyst, the main phase in the fresh sample is anatase,[90] but if platinum acetylacetonate is added to the sol, the main phase is rutile.[91] Similar results are reported when a tin[92] or copper[93] compound is added. In these processes it is assumed that the rutile-former acts as a nucleus for epitaxial growth of the rutile phase of titania on it, but the actual mechanism is still unclear.[92] Other routes to obtain nanocrystalline rutile titania involve the use of aqueous solutions of $TiCl_4$ and salts like NH_4Cl or $NaCl$ in acidic media.[92,94,95] In this case, the chloride salts play the role of the common ion effect used to limit the extent of hydrolysis of the $TiCl_4$ and the acid limits the rate of the oxolation reaction; both inhibitions are beneficial for the formation of a rutile phase.[95] One further possible method involves the use of $TiCl_4$ in low temperature non-hydrolytic sol-gel reactions.[96] In this method, alcoholysis of titanium tetrachloride by anhydrous ethanol in the presence of HCl, upon condensation has produced a small-particle precipitate with the formula $TiCl_x(OR)_y.ROH$.[96] Here, the presence of the residual unhydrolyzed ethoxy groups was presumed to inhibit the formation of the anatase phase.[96]

Based on this information, we attempted to prepare 3DOM rutile structures by the use of a high concentration of nitric acid with isopropanol/titanium isopropoxide mixture, the use of 1 wt % platinum in a mixture of titanium tetrabutoxide and butanol, the use of ~1 wt % of $CuCl_2/Br_2$ in acidic aqueous solutions of $TiCl_4$ or $TiBr_4$, and finally the alcoholysis of $TiCl_4$ in acidic dry ethanol. Under optimized conditions, pure rutile phases were obtained and a periodic macroporous structure was obtained.
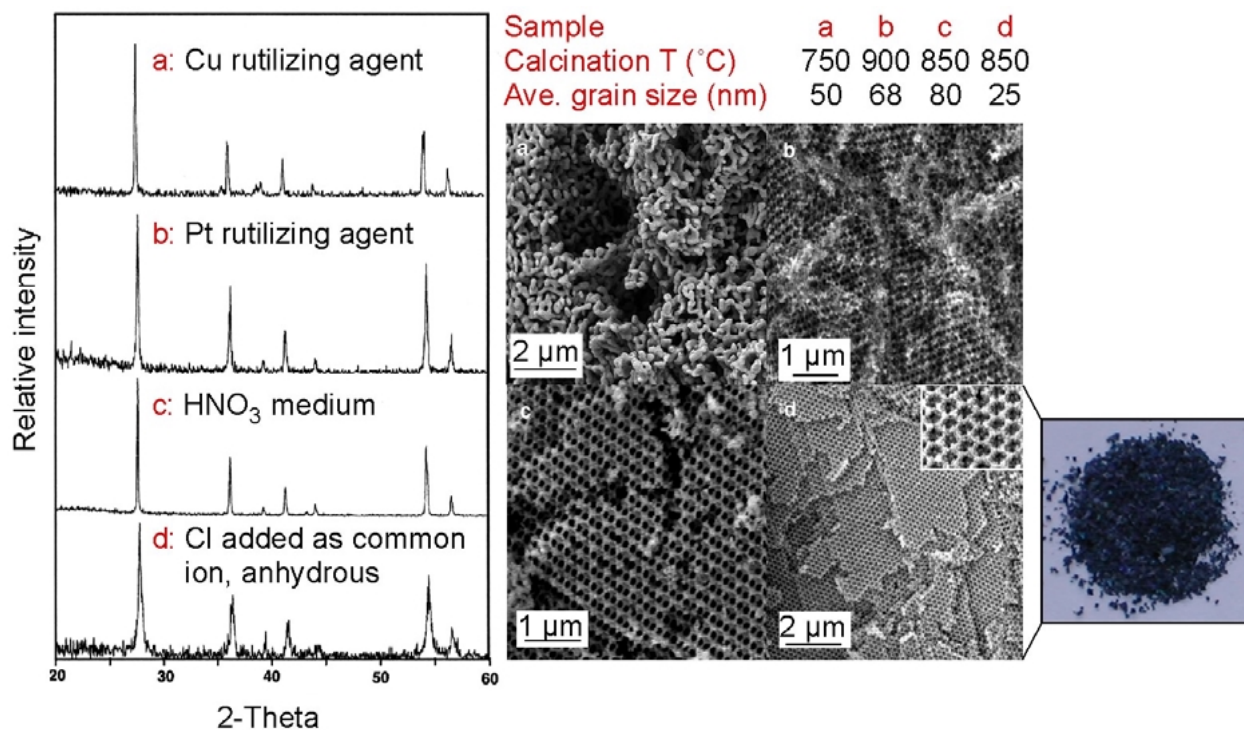
Figure 13. X-ray powder patterns and SEMs of macroporous titania prepared by infiltrating PMMA colloidal crystals with the following precursor solutions. a) Precursor for sample TiO_2-Cu was prepared by dissolving 0.1 g $CuBr_2$ in 15 mL anhydrous methanol followed by the addition of 1 mL of acetyl bromide. The solution was stirred for about 2 hours before the addition of 4.0 g of $TiBr_4$. The clear solution was stirred overnight at room temperature before using it to soak the colloidal latex. b) Precursor for sample TiO_2-Pt was synthesized by dissolving 0.015 g platinum acetylacetonate in a solution of 2.0 g glacial acetic acid and 10.0 g 1-butanol. 3.0 g titanium butoxide was added dropwise to the clear-yellow solution with stirring. The clear solution was stirred for 24 hours before using it to soak the PMMA latex. c) Precursor for sample TiO_2-NO_3 was synthesized by adding 0.35 g nitric acid to 7.5 g isopropanol before the addition of 4.0 g of titanium isopropoxide to the mixture. The clear solution was stirred for 2 hours before adding 0.5 g of water and then stirred for another 24 hours. d) Precursor for TiO_2-Cl was prepared by adding 2.5 mL acetyl chloride to 24 mL dry ethanol under an argon atmosphere. To the clear solution, 2.5 mL $TiCl_4$ was added dropwise with stirring under flowing argon. The solution was stirred for an additional 6 h before using it to soak the latex. Calcination temperatures and average grain sizes based on X-ray line broadening are indicated. The dark blue color of sample d as shown in the photograph is a reflection of the periodic structure of the material.

Based on the results shown in Figure 13, sample **a** (TiO_2-Cu) transformed into rutile at 750°C with a grain size of ~50 nm. However, the resulting material exhibited a worm-like structure. Variations in the synthesis conditions such as changing the concentration of the titanium in the solution, pH, the amount of Cu added, and the type of solvent used did not produce the desired periodic structure. This synthesis led to extensive agglomeration among the grains that prevented the formation of an open, periodic structure. Sample **b** (TiO_2-Pt) transformed to rutile with an average grain size of ~68 nm at the relatively high temperature of 900 °C, yet it produced a macroporous structure. The degree of order in the structure, however, was low. This was probably due to the high temperature used that caused enough sintering to prevent the formation of an ordered structure. It is to be noted that samples made under the same synthesis conditions, but without the addition of a source of platinum, gave worm structures even at lower calcinations temperatures. Sample **c** (TiO_2-NO_3), obtained by calcination at 850 ˚C, formed a 3DOM structure with a rather large average grain size of ~80 nm. The material, however, showed extensive

18

cracking, i.e., the average size of the ordered domains was relatively small, on the order of a few micrometers. The preparation of this particular sample was difficult to reproduce. For example, the total amount of water had to be carefully controlled, where excess moisture caused formation of a precipitate, and excess acid did not lead to the formation of the rutile phase at a reasonable calcination temperature. In addition, the solution had to be aged long enough (one day), in order to form sols. Sample **d** (TiO$_2$-Cl) was the simplest to prepare and reproduce. In this case, rutile formation occurred at a calcination temperature of 850 °C and led to an average grain size of ~25 nm. The periodic order of the material was rather extensive and the average size of the ordered domains was relatively large.

5.5 Control of color intensity through processing

Control of synthesis conditions during the formation of 3DOM solids is paramount for producing bright colors for pigments. In particular, the texture of the walls plays an important role in affecting the color intensity. This is illustrated for the case of 3DOM zirconia in Figure 14, below. For a synthesis carried out at higher temperature, the crystalline zirconia grains in the walls were monoclinic with grain sizes between 10–30 nm. Even though the product was relatively well ordered on the macropore scale, the roughness of the walls induced secondary scattering, and the product was white. A synthesis using a source of sulfate as an additive prevented a transformation from tetragonal to monoclinic zirconia and produced very smooth walls with 1–2 nm grains. These materials were brightly colored and even had a metallic appearance.[7,8,76]. Because of the importance of grain size and phase control in 3DOM zirconia, this material was studied in detail as outlined below and reported in reference [76]. A similar dependence of color intensity on processing conditions was found for 3DOM titania samples (see below).

Precursor: Zr[O*n*-C$_3$H$_7$]$_4$ in C$_3$H$_7$OH
PS colloidal crystal, 575 °C
Grain size: 10–30 nm
Monoclinic

Precursors: [CH$_3$CO$_2$]$_4$Zr,
HO$_2$CCO$_2$H, H$_2$SO$_4$, solvents
PMMA colloidal crystal, 500 °C
Grain size: 1–2 nm
Tetragonal
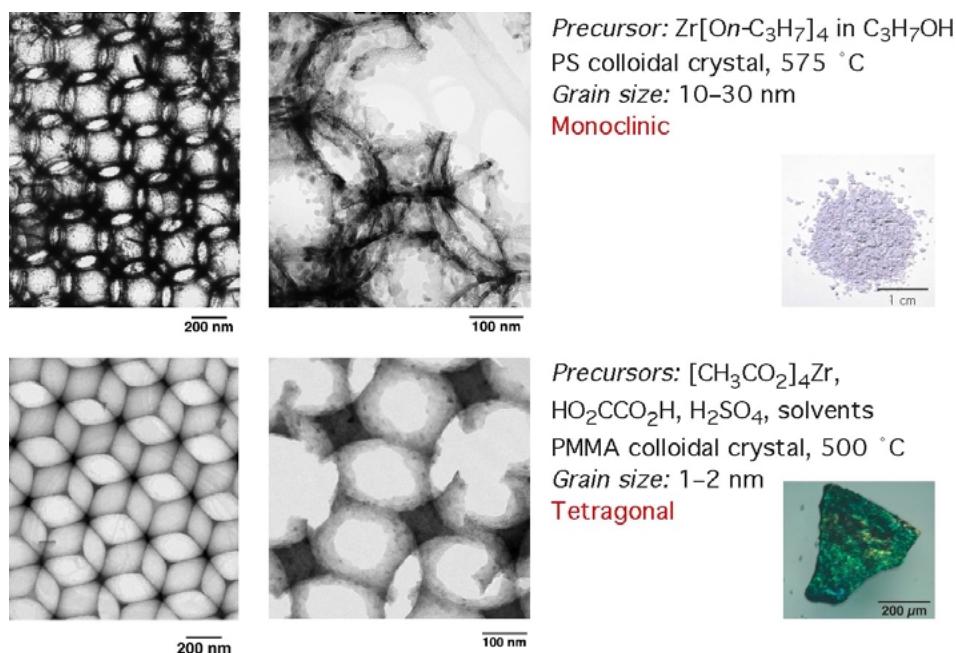
Figure 14. TEM images of 3DOM zirconia samples prepared by the infiltration of colloidal crystals using the methods indicated. Photographs of the bulk products are also shown.

19

5.5.1 Processing of 3DOM zirconia[76]

Ordered arrays of uniformly sized poly(methyl methacrylate) latex spheres were infiltrated with clear precursor solutions containing varying SO_4/Zr molar ratios. After solidification of the material in the void space between the spheres, the polymer templates were removed by calcination at various temperatures producing crystalline sulfated zirconia with a 3DOM structure. The effects of changing sulfate content and calcination temperature on the physicochemical properties of the material (including shrinkage, grain size, surface area, and composition) were systematically studied. The sulfate ions were initially present as species trapped in the bulk of the amorphous precipitate. Coincident with crystallization of the zirconia support, the sulfate was expelled onto the surface and transformed into an "activated" sulfate species. This transformation was concurrent with some loss of sulfate from the sample and continued loss with further heating. The presence of sulfate, however, retarded the crystallization and crystal growth, which enabled greater control of macropore shrinkage and periodic order of the material. The combined effects of crystal growth inhibition and inherent porosity of the PMMA latex were believed to be the major factors contributing to the BET surface area of the material, which was almost an order of magnitude larger than that of their non-templated counterparts and passed through a maximum as a function of calcination temperature and initial SO_4/Zr ratio. The maximum value of 119 m^2/g was attained by a sample with $SO_4/Zr = 2$, calcined at 625 °C, which retained a near monolayer sulfate surface coverage of 3.1 nm^{-2}. On the other hand, the behavior of the *n*-butane isomerization activity of the material, which also passed through a maximum as a function of calcination temperature and SO_4/Zr ratio, reached its maximum value for a sample with $SO_4/Zr = 2$, calcined at 600 °C, and with an apparent sulfate surface density of ~7 nm^{-2}, indicating that certain amounts of bulk sulfate species contributed to the catalytic activity of the material.

5.5.2 Processing of 3DOM titania

For 3DOM titania, too, the precursors and synthesis conditions strongly influenced the brilliance of the sample colors. Figure 15 shows optical images of 3DOM titania samples prepared from the three different precursors indicated. With $Ti(OPr)_4$ and nitric acid, condensation of titania was not well controlled, resulting in rapid grain growth within the skeletal walls. In spite of its relatively good pore order, the material was white. Pastel colored materials were produced when nitric acid was replaced by hydrochloric acid. Chloride ions can complex to the alkoxide precursor, slowing down condensation and grain growth. The most strongly colored samples were obtained by using the bis(ammonium lactato)$Ti(OH)_2$ precursor, which is water soluble and in which titanium is already in the octahedral coordination found in the product structure. This precursor had previously been employed in the synthesis of titania nanoparticles[97] and also appears to benefit the regularity of 3DOM materials.

$Ti(OPr)_4$, HNO_3, EtOH, H_2O
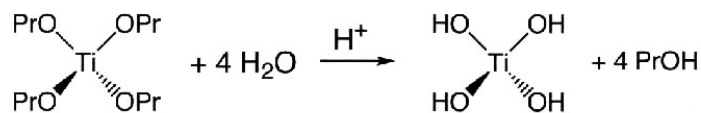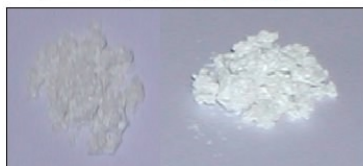
$Ti(OPr)_4$, HCl, EtOH, H_2O
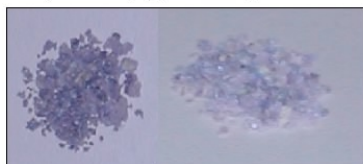
Condensation:
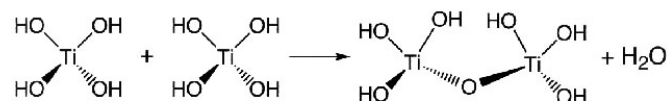
Bis(ammonium lactato)Ti(OH)$_2$, HCl, EtOH
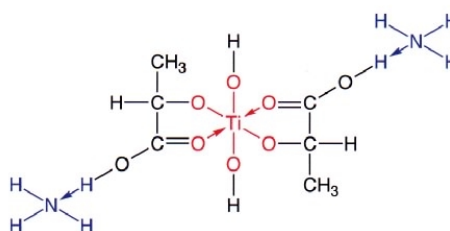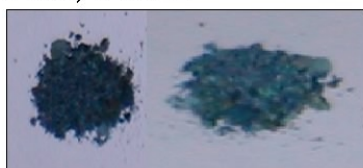
Figure 15. Images of 3DOM titania samples prepared from the indicated precursors, showing the differences in achievable color intensities. Each set shows two images of the same sample photographed from two different angles.

5.6 Control of color intensity through composite formation

3DOM silica is one of the most easily formed 3DOM materials and is also easily functionalized by co-condensation or grafting with organoalkoxysilanes. The walls of 3DOM silica are amorphous and very smooth, conditions that favor an optical filtering effect: well-ordered samples display one color in reflected light and the complementary color in transmitted light (see Figure 16).

Reflected Light   Transmitted Light
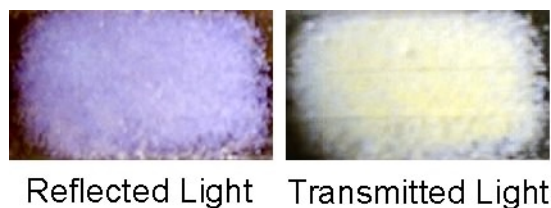
Figure 16. Images of 3DOM silica with 263 nm diameter macropores, photographed with light above the sample (left) and light behind the sample (right). Complementary colors are observed. Complementary colors were also observed in reflection and transmission modes for differently colored 3DOM silica samples having other pore sizes.

However, because of the relatively low refractive index of silica (in the bulk, n = 1.45), 3DOM silica is not intensely colored. We were able to increase the color intensity significantly by incorporating hydrothermally prepared rutile/anatase nanoparticles (<15 nm) within the walls of 3DOM silica, varying the titania content from ca. 0.5-20 wt%. Figure 17 shows examples of the

resulting samples. These inorganic composites have color intensities comparable to those of the 3DOM zirconia samples discussed above. Other advantages of these composites are that

- the effective refractive index of the walls can be controlled by the volume fraction of nanocrystals embedded in the silica walls,
- 3DOM structures can be obtained for compositions that are otherwise difficult to template with colloidal crystals,
- functionalization of the composite walls with organic groups is possible by methods that are well established for silica, and that
- the embedded nanoparticles can add further functionality (such as catalytic activity) to the material.

These composites combine the processability and chemistry of silica with other advantages of the nanoparticles, therefore allowing for complex compositions and structures.
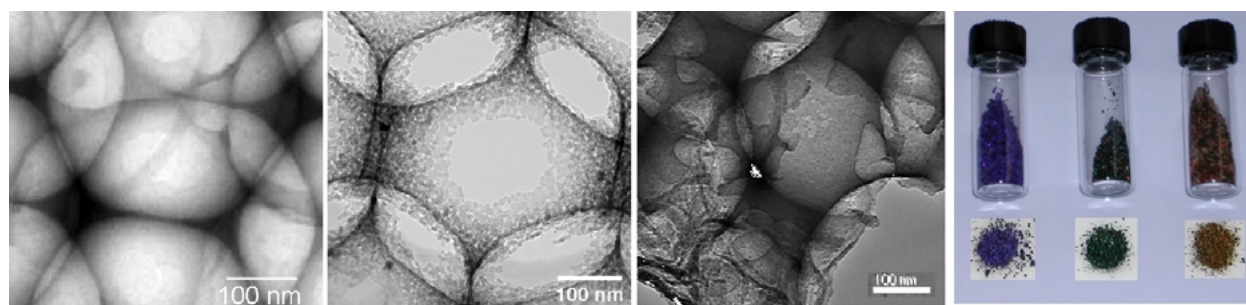
3DOM silica   3DOM anatase   3DOM silica composite with rutile nanocrystals

Figure 17. Left three images: TEM images showing the wall texture of 3DOM silica with very smooth walls, 3DOM anatase with nanocrystalline wall particles, and a 3DOM silica composite with titania nanocrystals, which provide some surface texture. Right image: Photographs of 3DOM silica samples with embedded titania nanoparticles showing the bright colors that can be obtained and varied through synthesis parameters.

5.7 Effects of 3DOM particle sizes on optical properties

The sizes of 3DOM particles become important in pigment applications. For glossy paints, particles of micrometer size or smaller are required. By necessity, 3DOM particles cannot be this small, because typical unit cells have dimensions on the order of half a micrometer (and larger for IR-active PCPs) and multiple cells are required to produce diffraction effects. However, other applications can be based on larger pigment particles, including textured paints and thick coatings. Commercially used interference pigments in metallic paints[98,99] can be up to 30–60 µm in size to achieve the brightest effects.[100] We have begun to investigate the optical properties (appearance to the eye and UV-visible spectra) of 3DOM zirconia particles with different particle sizes. A masterbatch of brightly colored, blue 3DOM zirconia was prepared. The 3DOM zirconia was templated with amine-functionalized PMMA spheres using a solution of zirconium acetate in dilute acetic acid and methanol. The template was removed by calcination at 450 ˚C. The calcined products were brightly colored and consisted of tetragonal zirconia walls surrounding periodic arrays of pores with average diameters 235±15 nm. These particles were ground and sized by sieving through bronze meshes (mesh openings of 420, 250, 180, 148, 74 and 20 µm). We were unable to grind samples to sufficiently small sizes to pass them through a mesh with 5 µm holes. This observation is consistent with TEM images of ground samples which typically show fragments containing multiple pores. Images of the sieved blue samples are

22

shown in Figure 18 and UV-vis reflectance spectra of the air or ethanol-filled samples in Figure 19. Analyses of the wavelengths of stop band minima and intensities are provided in Figure 20.
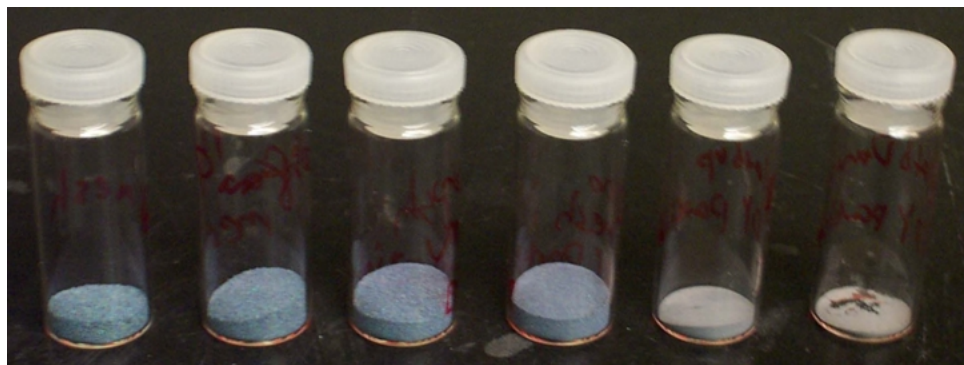
Figure 18. Images of 3DOM zirconia samples with 235 nm pores and particle size ranges of 420–250 µm, 250–180 µm, 180–148 µm, 148–74 µm, 74–20 µm, and <20 µm, from left to right.
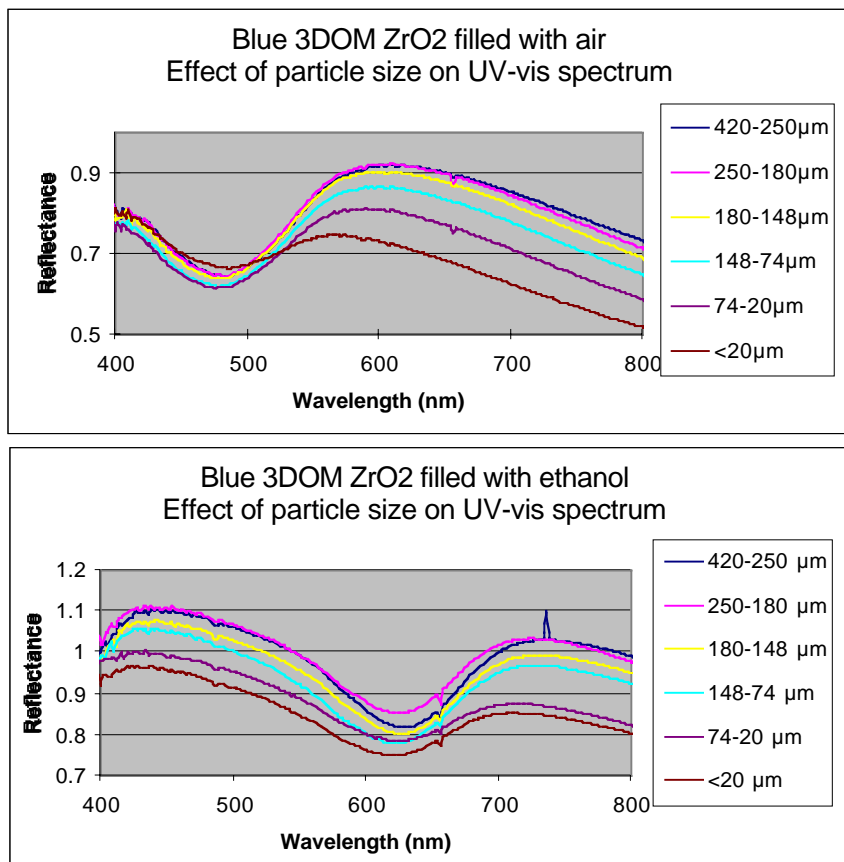
Figure 19. UV-visible reflectance spectra of 3DOM zirconia powders that had been sieved to the particle size ranges indicated in the legend. The spectra on the top correspond to dry samples, those on the bottom to samples whose pores were filled with ethanol.
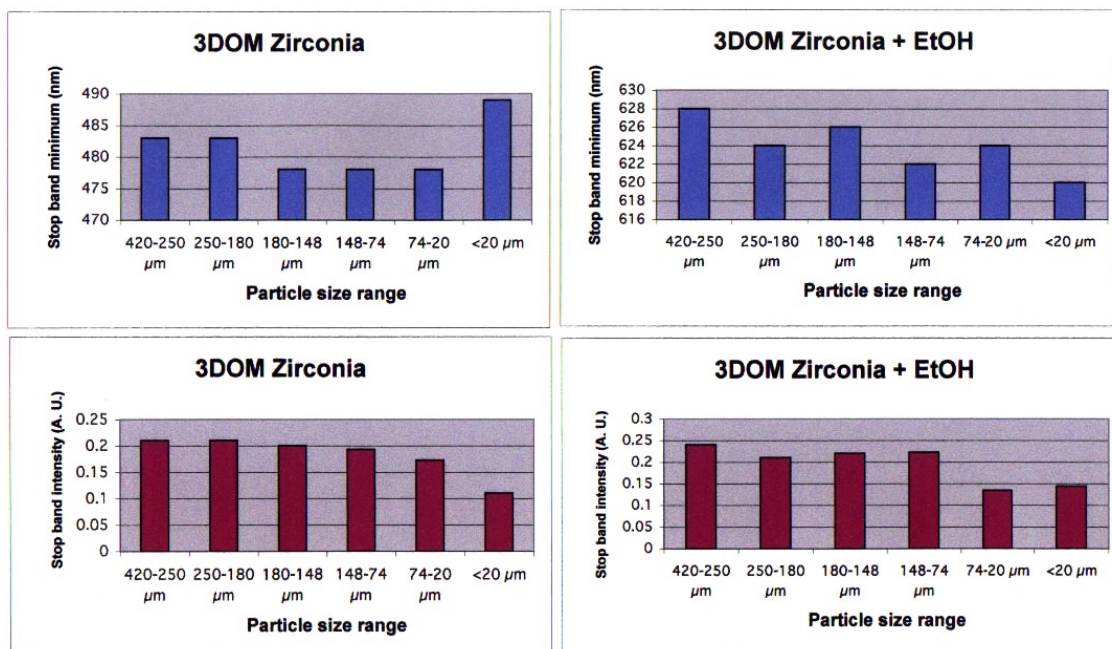
Figure 20. Effects of particle sizes of 3DOM zirconia and the positions of the stop band minima (top) and the stop band intensities (bottom) for samples whose pores were filled with air (left) or with ethanol (right).

These data show that stop bands were present even for the more finely ground samples. Stop bands varied within about a 2% range from 478–489 nm for the dry samples and a narrower 1% range from 620–628 nm for the ethanol-filled samples, where the refractive index of the walls and the voids was more closely matched so that less particle scattering occurred. Stop band intensity data and visual observations showed a distinct decrease in intensity as particle size ranges dropped below 75 μm, suggesting that pigment applications would be most effective for particles larger than 75 μm, which corresponds to ca. 280 periods. Similar observations were made for green 3DOM zirconia particles.

For camouflage coating applications, it is important to understand factors controlling the color and color intensity, or more generally the reflectance, transmission, and scattering properties of 3DOM pigments, as well as the absorption of the bulk composition making up the 3DOM skeleton. For practical reasons, the influence of pigment size on optical properties is also critical, as particle size affects minimum coating thicknesses. This factor is particularly important for 3DOM pigments, as their function relies on arrays of multiple pores, each of which can be between 200 nm and >5 μm in size for the visible and infrared ranges. The observation that color intensity dropped significantly for particles smaller than about 280 periods in each direction *demands a closer look at factors determining stop band intensities, band widths and positions,* so that one can identify ways of minimizing pigment sizes without sacrificing stop band intensities.

Optical properties of 3DOM pigments can be described in a manner analogous to that of their templating counterparts, crystalline colloidal arrays. As noted earlier, combinations of Bragg theory with Snell's law of refraction can therefore be applied as a first approximation to estimate stop band positions. Correcting for the interaction strength of the light and the photonic crystal, dynamical diffraction theory (DDT)[101] has been shown to improve the agreement with experiment. For thick polystyrene (PS) colloidal crystals immersed in water, DDT has been

24

applied successfully to describe effects of colloidal crystal structure, sphere size, and refractive index contrast on positions, intensities and diffraction peak half-widths.[102-104] In that system, 50 layer-thick arrays were shown to diffract essentially all incident light that satisfies the Bragg condition.[105] However, because DDT is derived with the assumption that dielectric contrast is small, it does not provide accurate predictions for the 3DOM crystals considered here, in particular when voids are filled with air.[106] This can be seen when Spry and Kosan's model,[105] which combines DDT with optical scattering theory[107] is applied to 3DOM ZrO_2. This calculation predicts that less than 20 layers should be sufficient to achieve full reflectivity values, in clear disagreement with our experimental observations for 3DOM ZrO_2. The scalar wave approximation (SWA) is more appropriate for systems with any significant dielectric contrast (such as 3DOM PCPs). This theory focusses on dispersion of photons caused by lattice planes along a single directions, such as the highly symmetric [111] axis in a face-centered cubic photonic crystal. For colloidal crystal layers, good agreement between smaller crystals and the bulk was observed using the SWA when the crystal thickness was larger than 200 sphere layers.[108,109] Mittleman et al. recently provided an elegant comparison between DDT and the scalar wave approximation (SWA), and demonstrated that for opals and inverse opals, SWA provides more accurate predictions of optical stop band widths, but that neither of the two methods predicts absorption intensities well.[106] The study suggested that failure of DDT and SWA simulations to accurately predict absorption intensities appears to be related to crystalline defects in the samples. Notably, it was stated that *an accurate calculation to predict intensities is still lacking in the literature*.[106] Furthermore, these models have so far been tested mostly on extended films, not on relatively small 3DOM particles suitable for pigments.

All the above models assume a perfect lattice. For actual, imperfect 3DOM particles with large index contrasts, a number of factors can affect line broadening and intensities.[110] These include homogeneous broadening caused by finite thickness of individual domains (i.e., particle size effects),[35] inhomogeneous broadening from multiple domains, broadening due to incoherent scattering caused by distortions of the templated microstructure and other structural irregularities, and Raleigh scattering[111] by the microcrystals in the 3DOM walls skeleton. These interactions become particularly complex in the vicinity of the stop band where resonance enhancement may occur.[110] Bulk defects, such as stacking disorders[112] and scattering by the wall crystallites should be similar in large 3DOM particles and smaller particles derived from these by grinding. Parameters that will differ significantly though, include particle shape, particle size, and surface roughness. Figure 21 shows an example of particles, indicating the uneven surface topology and random shape of particles. Because of the rapid attenuation of radiation as it passes through the 3DOM crystals with high dielectric contrast, the major diffuse scattering effects are to be expected at crystal edges and within a few lattice planes at the surface of the material.[35,102,111,113] Such effects become more predominant for smaller 3DOM particles with higher external surface-to-volume ratios and can lead to the observed reduction in color intensity for the smaller particles.
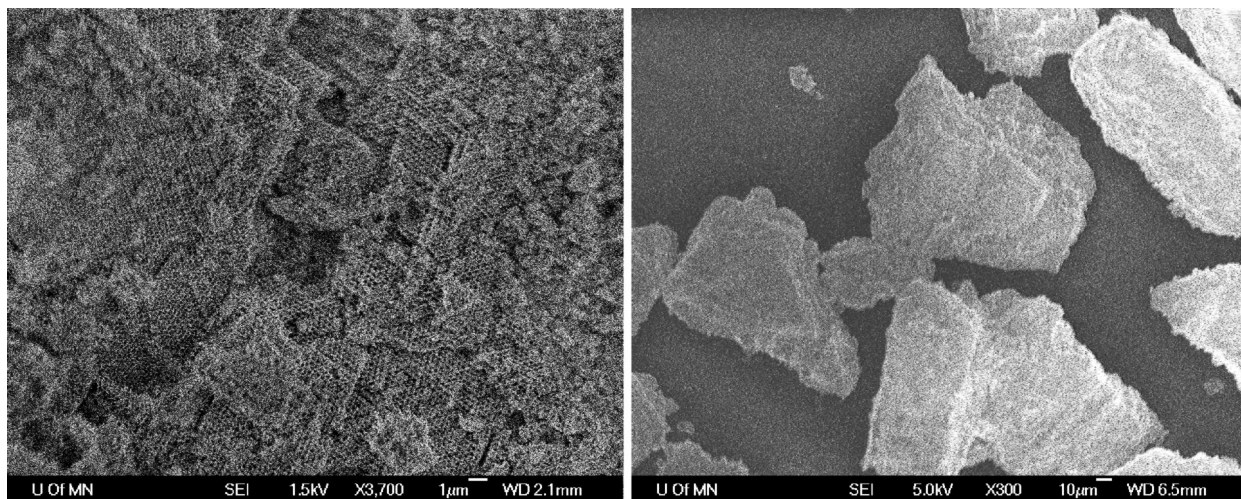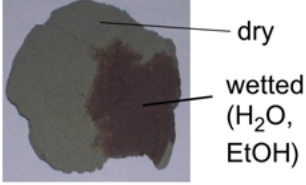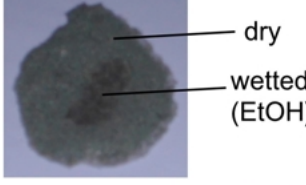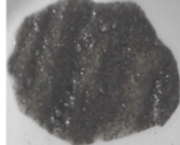
Figure 21. SEM images of 3DOM ZrO$_2$ samples that had been ground and sieved through a 74 µm nominal pore size sieve. The images show rough surface texture and random shapes with an average aspect ratio of 1.5, based over 60 particles observed in multiple images.

6. Composite formation with 3DOM pigments for coatings

We have performed screening experiments that enable formation of coatings by preparing various composites of 3DOM zirconia particles. The objectives were to bind particles together, allowing them to be stabilized and shaped, while maintaining the interesting properties of the 3DOM materials, such as accessible pores or color changes with penetration of guest molecules. In these investigations, opalescent green 3DOM zirconia particles were homogenized by slight grinding, sized and then mixed with a commercial acrylic latex paint base, a precursor for silica sol-gel glasses, polydimethyl siloxane (PDMS), or a polyvinylalcohol (PVA)-based hydrogel. Each of these matrices exhibited different properties related to dispersion of the pigments, flexibility of the coating, alteration of the color and accessibility of pores in the pigments. Several limitations were observed, which included uneven dispersion of 3DOM particles in the matrix; penetration of matrix material into pores causing a shift in the stop band absorption and sometimes reduction in color intensity; dilution of pigments in binders reducing color intensity; blocking of pores in certain binders, so that they were no longer accessible and colors could not be modified dynamically. The issue of pore infiltration and blocking was addressed by filling the pores with wax before mixing pigments with binder. For temperature-stable binders, such as sol-gel glasses and PDMS, the wax could be partially or completely removed, restoring the original color of the pigment. Pores in the composite with PVA hydrogel remained accessible even without a temporary pore filler, permitting the color of the composite to be varied by infiltration with alcohol. Processing conditions and properties of composites containing 3DOM zirconia are summarized in Table 1.

26

Table 1. Processing conditions and properties of composites containing 3DOM zirconia.

Matrix	Processing temperature	3DOM/matrix volume fraction	Temporary pore filler	Pores remain accessible	Properties
PVA/Na$_2$B$_4$O$_7$ — dry, wetted (H$_2$O, EtOH)	70°C	high	no pore filler	yes EtOH: sec H$_2$O: min	pliable when wet / brittle when dry
PDMS (Sylgard 184) — dry, wetted (EtOH)	150°C	high	wax added	partially (used needle to penetrate PDMS)	flexible
Sol-gel silica glass	250°C	low	no pore filler	no	brittle fragments
	250°C	low	wax added	no	brittle fragments
Latex paint base	30°C	intermediate	wax added	no	flexible

6.1 Processing 3DOM pigments with binders

The sized 3DOM zirconia particles were mixed with a commercial paint base (Behr's Premium Plus No. 3300 deep base, 100% acrylic latex) at an approximate weight ratio of 1 g solids to 5 g base. These mixtures were painted on a polystyrene plastic surface and allowed to dry. Figure 22 shows images of the painted surfaces together with the original pigment particles and Figure 23 shows the UV-visible spectra of these samples. The colors of the dried paint were different from those of the original pigments because components of the paint base were able to enter the macropores and deposited on the macropore surfaces. As a result, the effective wall thickness and refractive indices were modified to yield the color shift. Red shifts of the stop bands were more predominant for the smaller particles, which were infiltrated by a relatively larger fraction of paint base. Stop band intensities were also reduced as the uniformity of the pore structure was diminished. To minimize such effects it may be possible to reduce apertures in photonic crystal particles or to employ a paint base which contains latex particles large enough that they will not enter the macropores.
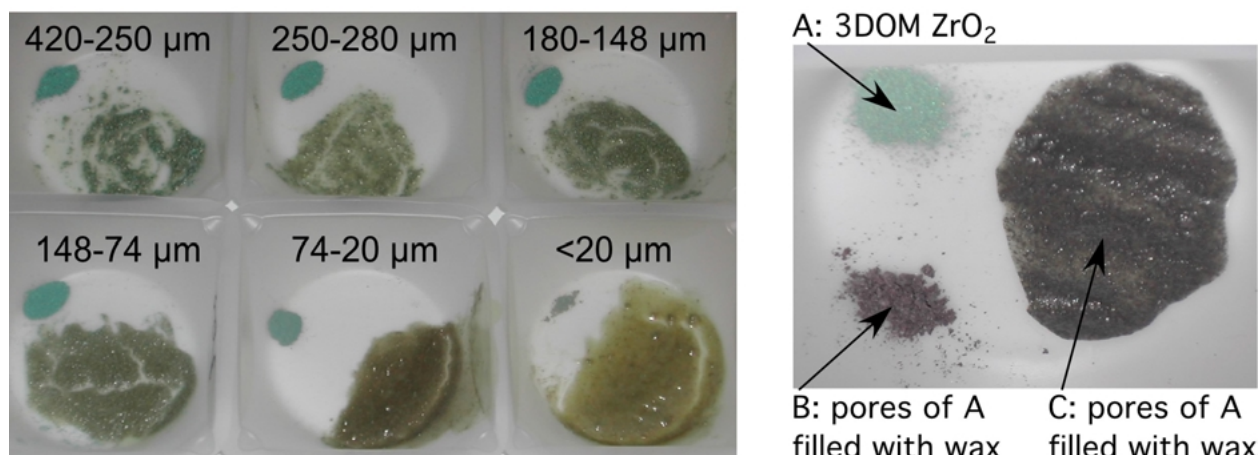
Figure 22. Left: images of 3DOM zirconia samples with the indicated particle size ranges, as pure samples (top left corner of each image) and mixed with a latex paint base, then dried. Because the base penetrates 3DOM particles, it alters their spectral properties. Right: images of (A) pure 3DOM zirconia, (B) 3DOM zirconia whose pores have been filled with parrafin wax to block pores and prevent their penetration by paint base, and (C) a dried coating of the wax-filled material with latex paint base.
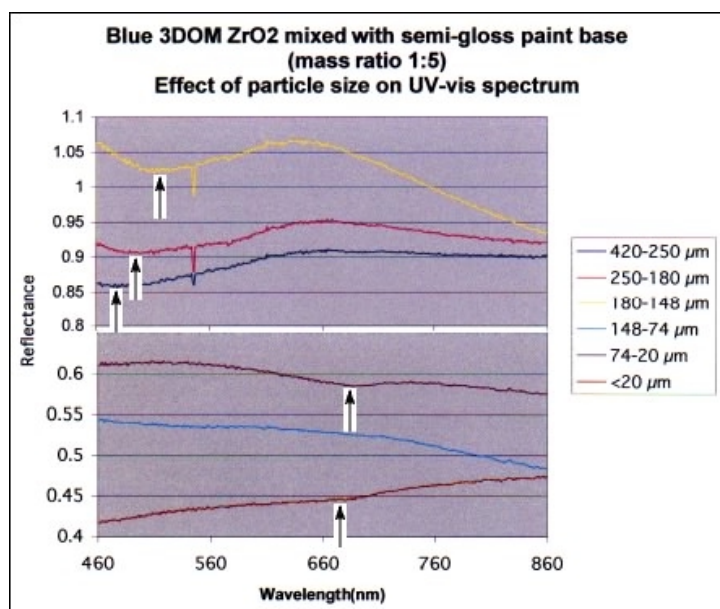
Figure 23. UV-visible reflectance spectra of dried paint prepared from 3DOM zirconia powders that had been sieved to the particle size ranges indicated in the legend and mixed with paint base. Arrows indicate the stop band minima.

6.2 Polymer solution filling

- In-situ "slime" formation: One batch of 3DOM ZrO_2 particles was filled with an aqueous polyvinyl alcohol (PVA) solution, another batch of particles with aqueous sodium borate solution. Both batches were penetrated by the solutions as indicated by an immediate color change from green to purple. Upon mixing of the two batches, hydrogen bonding between PVA chains held the particles together. The composite could be shaped and dried and held together relatively well. The dried composite could still be penetrated by water or alcohol, leading to reversible color changes. Excessive pressure led to crushing of the composite.

28

- Filling with a PMMA solution: 3DOM zirconia was filled with a 10% solution of PMMA in toluene. The solution penetrated the 3DOM structure as indicated by the color changes fom green to purple (wet) and brown/grey (dry). However, the composite could not be penetrated well by EtOH, due to pore blockage by the polymer.

6.3 In-situ anionic chain polymerization

Filling with methyl 2-cyanoacrylate ($H_2C=C(CN)C(=O)OCH_3$, superglue): pores of 3DOM ZrO_2 particles were readily filled with superglue as evidenced by an immediate color change form green to purple. Particles adhered well to each other. The dried composite was grey and appeared to be harder than the original particles; however, the composite was brittle. Pores in the composite could be penetrated by MeOH, EtOH, acetone, but not by water. See Figure 24.
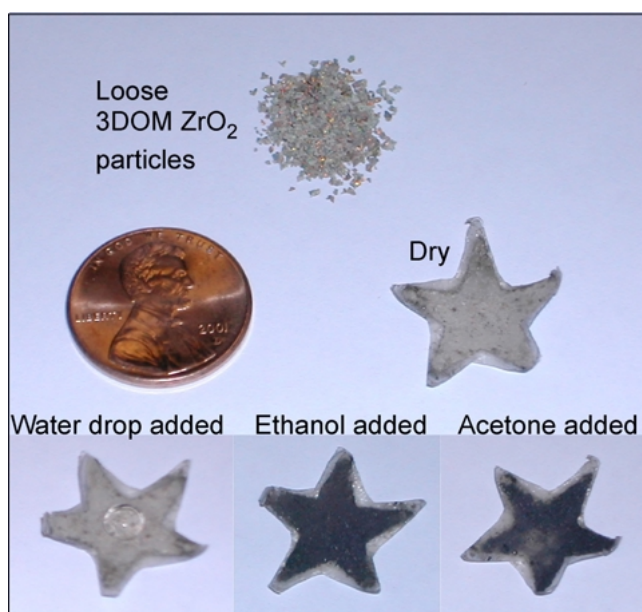
Figure 24. Star-shaped films of 3DOM ZrO_2/superglue composites supported on transparency film. The opalescent green color of the loose 3DOM particles did not reproduce well in the figure. The light grey film samples turned dark grey/purple upon wetting with ethanol or acetone. The lighter colored areas in the acetone-filled sample are due to rapid solvent evaporation.

6.4 In-situ condensation polymerization

- In-situ nylon formation: One batch of 3DOM zirconia particles was filled with a solution of hexanediamine, $H_2N(CH_2)_6NH_2$, in aqueous base, and another batch of particles with a solution of sebacoyl chloride, $ClOC(CH_2)_8COCl$, in hexane. Both batches were penetrated by the solutions as indicated by an immediate color change from green to purple. Before the two batches were mixed, particles agglomerated after wetting with the monomer solution. Mixing of the two batches did not improve adhesion between particles. The dried product was green again. The agglomerate was very brittle and crumbled apart when handled.
- Filling with tetraethylorthosilicate (TEOS, $Si(OEt)_4$): TEOS penetrated the sample as indicated by a color change from green to purple. The dried sample was grey and could be wetted by water. However, the particles did not adhere well to each other.

29

7. Formation of Hybrid Organic-Inorganic 3DOM Materials

7.1 Functionalization with molecular surface groups

Macroporous hybrid materials with organosulfonate, organophosphonate, and organosiloxane groups incorporated into titania and zirconia were prepared. We established optimum conditions for precursor solutions that can efficiently penetrate a PMMA colloidal crystal template and lead to periodic macroporous structures. Relative loadings of organic groups obtained by direct synthesis and grafting methods (see Figure 25) were compared. Previously, 3DOM silicates with organic functional groups had been prepared by direct synthesis and grafting. Because of their interesting optical properties, we investigated functionalization of 3DOM TiO_2 and ZrO_2 samples.
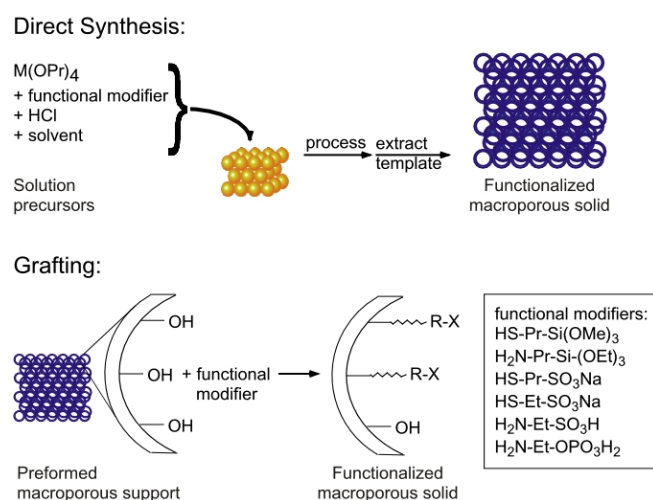
Figure 25. Schematic of methods for functionalizing 3DOM supports with molecular surface groups.

7.1.1 Direct synthesis

Clear precursor solutions were prepared by the addition of alkoxide (either titanium(IV) propoxide, $Ti(OPr)_4$, or zirconium(IV) propoxide, $Zr(OPr)_4$ as a 70 wt% solution in 1-propanol) and functional group precursors (see Table 2) to EtOH/HCl solutions. PMMA colloidal crystals were infiltrated with these clear solutions. Infiltrated colloidal crystals were dried and heated at 80 ˚C for 10 h to aid wall solidification.

Table 2. Commercially available precursors for functional group attachment.

Functional Group Class	Compound	Formula	FW (density)
Thiol-silicate	3-mercaptopropyl-trimethoxysilane	$HS-Pr-Si(OMe)_3$	196.34 (1.039)
Amino-silicate	3-aminopropyl-triethoxysilane	$H_2N-Pr-Si-(OEt)_3$	221.37 (0.946)
Thiol-sulfonic acid	3-mercapto-1-propane-sulfonic acid, Na salt	$HS-Pr-SO_3Na$	178.21
Thiol-sulfonic acid	2-mercapto-ethane-sulfonic acid, Na salt	$HS-Et-SO_3Na$	164.18
Amino-sulfonic acid	2-amino-ethane-sulfonic acid	$H_2N-Et-SO_3H$	125.15
Amino-phosphonic acid	2-amino-ethyl di-hydrogen-phosphate	$H_2N-Et-OPO_3H_2$	141.07

Successful syntheses of hybrid 3DOM materials with covalently grafted organic groups were achieved with single precursor solutions for the following compositions: TiO_2-Si-Pr-SH, TiO_2-Si-Pr-NH_2, TiO_2-SO_3-Pr-SH, TiO_2-SO_3-Et-SH, ZrO_2-Si-Pr-SH, ZrO_2-Si-Pr-NH_2. Some products are shown in Figure 26.
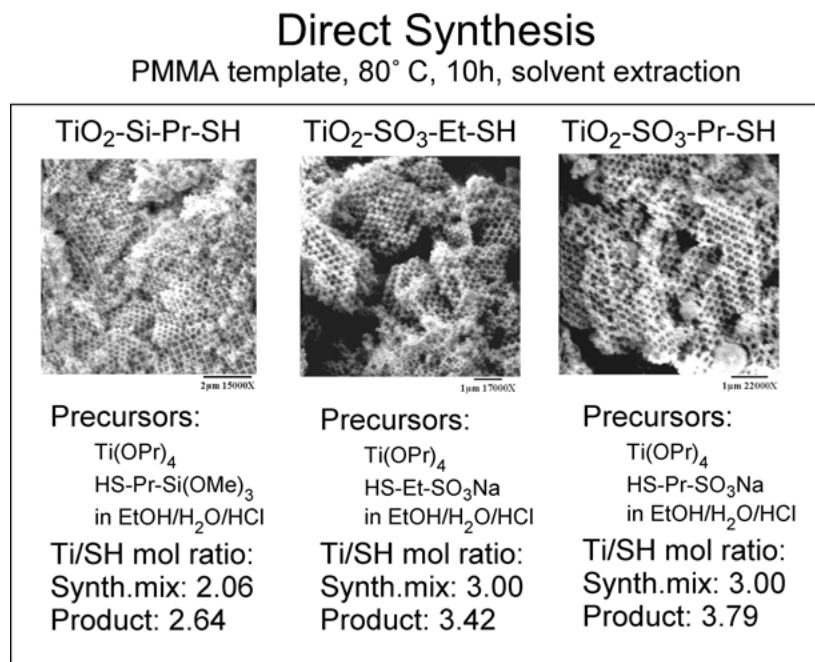
Figure 26. SEM images and precursor/product compositions of direct synthesis products.

The order of addition of reagents to the reaction vial was found to be very important to prevent immediate precipitation of the solid and permit penetration into the template. Highly acidic solutions were necessary in all cases involving the addition of water. To preserve the organic functional groups, the PMMA template was removed by multiple solvent extraction with THF/acetone under reflux.

A two-step direct templating synthesis was employed when immediate precipitation of precursors in a single precursor solution prevented template penetration (in the cases of TiO_2-OPO_3-Et-NH_2 and ZrO_2-SO_3-Pr-SH). In this procedure, a solution of the organic functional group salt was first added to the sphere template, followed by addition of the alkoxide after the sample had dried.

In general, all of the syntheses for which precursor solutions could be made yielded hybrid porous materials with covalently grafted organic groups. The IR spectra of these materials exhibited bands for the organic groups (Si-O, S-O, and P-O) of approximately the same intensity as the M-O bands (M = Ti, Zr), indicating high incorporation levels of the organic groups. In addition, the spectra indicated that linking had occurred, as the positions of the bands shifted compared to the positions of these bands in the precursors. The two-step direct synthesis (samples TiO_2-OPO_3-Et-NH_2 and ZrO_2-SO_3-Pr-SH), for which a single precursor solution could not be made, also produced porous materials with high levels of grafted organic groups. The

31

relevant IR bands for the precursors and for products, as well as their structural properties, are listed in Table 3 below.

Following the synthesis of the co-condensed materials, we subsequently examined their performance in the uptake of toxic heavy metals, including mercury and lead ions. These results have been published.[114] The original motivation for absorbing these and related ions (e.g., Cd^{2+}) on the surfaces of the macroporous supports was to increase the effective refractive index of the walls upon absorption and thereby having a detection mechanism for these heavy metals. This effect was tested with a thiol-modified 3DOM silica support. While the color of this material changed upon adsorption of the metal ions, the shift was not only due to the compositional change in the wall, but (mainly) due to dimensional changes as the 3DOM mercaptosilica continued to condense and shrink during exposure to the ion-containing solution. One reason for the condensation was the necessity to maintain low processing temperatures to avoid loss of the thiol groups; due to the low processing temperatures, many uncondensed silanol groups remained in the material and could react later. Nonetheless, the ability of the hybrid macroporous materials to remove mercury(II) and lead(II) can be of interest in wastewater clean-up, and the open macropore structure can offer improved mass transport in flow-systems.

The ability of the hybrid macroporous materials to remove the heavy metal ions mercury(II) and lead(II) from solution was tested by stirring the adsorbents in aqueous solutions of the metal ions. Structural data on the samples are provided in Table 3. Results of the metal ion adsorption tests are summarized in Table 4. The adsorption capacity of the hybrid macroporous materials for mercury(II) ions ranged from 0.33–1.41 mmol of Hg(II) ions adsorbed per gram of adsorbent. The Hg(II) loading was similar for each class of functional group, with the best results obtained for the thiol-metal oxides with propyl-sulfonate linkages. The adsorption efficiencies ranged from 0.19–0.82 mol of Hg(II) ions adsorbed per mol of thiol groups in the adsorbents. Less than stoichiometric adsorption is most likely due to a limited accessibility of the thiol groups in the interior of the walls. The adsorption capacity for lead(II) ions ranged from 0.27–1.24 mmol g^{-1}, with the thiol-titania samples containing sulfonate linkages exhibiting the highest loadings. The adsorption efficiencies for Pb(II) ions ranged from 0.21–0.72 mol of Pb(II) ions adsorbed per mol of thiol groups. The heavy metal ion loading capacities achieved with the hybrid macroporous titania and zirconia adsorbents are competitive with results of ca. 0.10–3.00 mmol g^{-1} for Hg(II) and 0–0.35 mmol g^{-1} for Pb(II) obtained for various porous silica-based adsorbents. It should be noted that absorption efficiences for lead(II) ions on thiol-derivatized titania samples were particularly high, exceeding those reported for porous silica-based adsorbents. This may be due to non-specific lead adsorption on the titania support in addition to binding to thiol groups. Titania is known to adsorb lead(II) through surface Ti-OH groups, in particular at pH>5.[115]

To test the reusability of the hybrid macroporous adsorbents, the Hg(II) ion loaded samples were treated with 1 M hydrochloric acid to remove the heavy metal ions. The leached materials were then subjected to a second round of metal ion adsorption testing. The results for metal ion adsorption using the regenerated adsorbents are summarized in Table 5. All of the hybrid macroporous materials maintained greater than 50% of the original metal ion loading capacity. The regenerated thiol-zirconia samples generally retained higher loading capacities than the thiol-titania samples, giving average capacities of 74% and 58% of the original loading, respectively.

Table 3. Physical characterization of the hybrid macroporous materials and precursors.

Material	IR (S-O) or (Si-O)/cm^{-1}	Pore size nm	Template size nm	Surface area m^{2}g^{-1}	Thiol density mmol g^{-1}
(MeO)$_3$Si-Pr-SH gel	1119, 1039	–	–	–	–
T1, TiO$_2$-O$_3$Si-Pr-SH	1141, 1040	265	300	37	2.24
Z1, ZrO$_2$-O$_3$Si-Pr-SH	1125, 1037	415	480	18	1.38
NaO$_3$S-Et-SH	1206, 1168, 1139, 1058	–	–	–	–
T2, TiO$_2$-O$_3$S-Et-SH	1232, 1155, 1047	270	300	12	1.78
Z2, ZrO$_2$-O$_3$S-Et-SH	1243, 1151, 1047	450	480	20	1.29
NaO$_3$S-Pr-SH	1221, 1198, 1168, 1065	–	–	–	–
T3, TiO$_2$-O$_3$S-Pr-SH	1223, 1149, 1047	275	300	12	1.71
Z3, ZrO$_2$-O$_3$S-Pr-SH	1241, 1147, 1044	460	480	14	1.35

Table 4. Metal ion adsorption data for the hybrid macroporous materials.

Material	M/SH (M=Ti,Zr) mol/mol	Hg(II) adsorbed mmol g^{-1}	Pb(II) adsorbed mmol g^{-1}	Adsorption efficiency mol/mol Hg/SH	Pb/SH
T1, TiO$_2$-O$_3$Si-Pr-SH	2.61	0.43	0.47	0.19	0.21
T2, TiO$_2$-O$_3$S-Et-SH	3.28	0.33	0.82	0.19	0.46
T3, TiO$_2$-O$_3$S-Pr-SH	3.63	1.41	1.24	0.82	0.72
Z1, ZrO$_2$-O$_3$Si-Pr-SH	3.41	0.54	0.36	0.39	0.26
Z2, ZrO$_2$-O$_3$S-Et-SH	3.52	0.45	0.27	0.35	0.21
Z3, ZrO$_2$-O$_3$S-Pr-SH	3.66	0.87	0.36	0.64	0.27

Table 5. Metal ion adsorption data for the regenerated hybrid macroporous materials.

Material	Hg(II) adsorbed/mmol g^{-1} Initial test	2nd test	% Original metal ion loading capacity
T1, TiO$_2$-O$_3$Si-Pr-SH	0.43	0.27	63
T2, TiO$_2$-O$_3$S-Et-SH	0.33	0.19	58
T3, TiO$_2$-O$_3$S-Pr-SH	1.41	0.75	53
Z1, ZrO$_2$-O$_3$Si-Pr-SH	0.54	0.37	69
Z2, ZrO$_2$-O$_3$S-Et-SH	0.45	0.34	76
Z3, ZrO$_2$-O$_3$S-Pr-SH	0.87	0.67	77

7.1.2 Grafting
Grafting reactions to attach functional groups were carried out on 3DOM zirconia, which was prepared from zirconium acetate solution in dilute acetic acid by penetration of PMMA colloidal crystals (ca. 450 nm diameter). The material was calcined at 500-600°C to obtain a product with walls composed of tetragonal zirconia nanograins. In tetragonal zirconia, Zr atoms are coordinated to eight lattice oxygen atoms. This type of coordination imparts the tetragonal phase with a higher concentration of surface hydroxyl groups than is present in other denser ZrO_2 phases. These supports had a typical surface area of 33 m^2/g and a typical average grain size of 6.7 nm. For samples in which the organic groups were incorporated by post-synthesis grafting involving silicate or sulfonate linkages (ZrO_2-Si-Pr-SH, ZrO_2-SO_3-Pr-SH), the infrared bands for the organic groups were very weak, indicating only small levels of organic incorporation by grafting.

The organic content in 3DOM zirconia samples modified by grafting could be increased by using zirconia calcined at a lower temperature (450 °C, 3 h) and by employing more reactive chlorosiloxanes instead of alkylsiloxanes as functional group precursors. For example, when 3DOM zirconia (450 °C) was modified with *p*-chloromethylphenyltrichlorosilane, the organic content, based on TGA, was as high as 5.3 wt% (0.4 mmol of functional group/g). This compares with ca. 10 wt% (1.4 mmol of functional group/g) for directly synthesized samples.

To investigate phosphonate linkages, we synthesized the bifunctional $H_2O_3P(CH_2)_6PO_3H_2$ (C6BP) and $HOOCC_6H_4CH_2PO_3H_2$ (BMP) as coupling agents to connect zirconia nanograins within the wall structure. 3DOM ZrO_2 was refluxed in solutions containing excess of these modifiers at varying pH levels between pH 3.5 to 8. Phosphonation with C6BP occurred only under mildly alkaline conditions (pH 8). A single resonance in the ^{31}P solid-state NMR spectrum at 13 ppm (upfield from the free acid by 17 ppm) indicated attachment of phosphonic acid to the zirconia surface, apparently through both ends of the bisphonic acid. To avoid double-attachment of a single functionalizing molecule, a carboxyl phosphonic acid agent (BMP) was synthesized and used in the phosphonation of 3DOM ZrO_2. Attachment was achieved at pH 7.3, as indicated by a single resonance in the ^{31}P solid-state NMR spectrum at 16.5 ppm (upfield from the free acid by 12 ppm).

7.2 Surface functionalization of 3DOM oxide supports with polyelectrolytes and nanoparticles of another oxide *(This section is adapted from the Ph.D. thesis of Mohammed A. Al-Daous, University of Minnesota, 2003.)*
Because of their relatively large pores, 3DOM oxide supports are capable of being coated with nanoparticles to integrate multiple functionalities within a continuous system. We investigated the concept of nanoparticle coating on 3DOM supports using 3DOM zirconia as the backbone and zeolite seeds for the nanoparticle coating. While this combination was chosen to target a dual catalyst system capable of combined activities in Fischer-Tropsch reactions with hydroisomerization for the direct conversion of synthesis gas to isoalkanes, the synthetic concepts are more general and can be extended to other materials compositions. Zeolite coatings can be of particular interest to needs of the Army, because these microporous aluminosilicates display unique, selective sorption and catalysis properties.[116] They can be useful, for example, for selective adsorption and decomposition of contaminants. In 3DOM coatings, the sorptive/catalytic properties could function in addition to the unique optical and reactive

properties of the 3DOM architecture. The well established syntheses of a variety of 3DOM materials offer the possibility of preparing composite/hybrid catalysts comprising a layer of microporous zeolites hydrothermally grown on top of an existing catalytic framework such as that of 3DOM zirconia modified with oxoanions.[76] The synthesis of such a system is accomplished by first coating the initial 3DOM metal oxide framework with multilayers of polyelectrolytes alternating in charge,[117] where the charge of the final layer is matched favorably for nucleation and growth of zeolites nanocrystals from a clear precursor solution.[118,119] We synthesized nano-ZSM-5 and nano-NaY zeolite coated on a 3DOM sulfated or tungstated zirconia catalysts (SZ or WZ, respectively), which are known to be highly active isomerizing systems.[120]

The structures of the 3DOM SZ and WZ products are shown in Figure 27. The BET-surface areas of the samples were 125 m^2/g and 137 m^2/g for SZ and WZ, respectively. The wall structures of these macroporous solids are polycrystalline. The average crystal size, estimated from XRD line broadening, was ~7.2 nm for SZ and ~7.9 nm for WZ. XRD patterns for the samples (Figure 28) show crystallization of the amorphous precipitate into a tetragonal zirconia phase (PDF#42-1164).
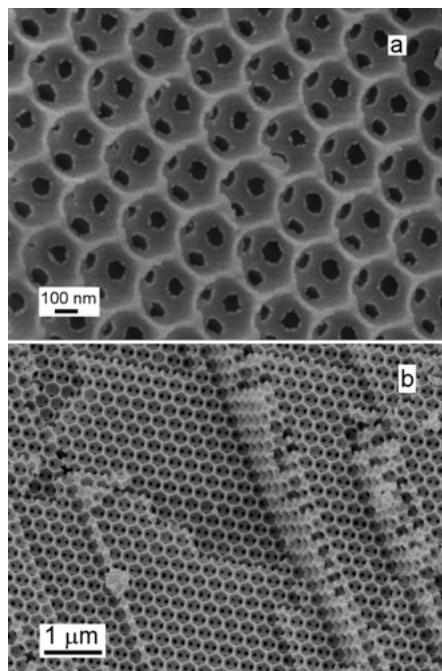
Figure 27. SEM images of (a) 3DOM sulfated zirconia (SZ) calcined at 600 °C and (b) 3DOM tungstated zirconia (WZ) calcined at 675 °C. (Metal promoted 3DOM zirconia supports were synthesized using PMMA colloidal crystal templates. For 3DOM Pt/Sulfated-Zirconia (SZ, 0.5 wt% Pt), the template was impregnated with a precursor solution containing sulfuric acid, zirconyl nitrate, hydrogen hexachloroplatinate, and methanol. For 3DOM Pt/Fe/WO$_x$/ZrO$_2$ (WZ, 0.5 wt. % Pt, 1.0 wt. % Fe, and 19.0 wt. % W), the precursor solution contained zirconium acetate, ammonium metatungstate, hydrogen hexachloroplatinate and iron nitrate in water/methanol. The composite sample was allowed to dry in air at room temperature before calcination in air at 600-675 ˚C.)
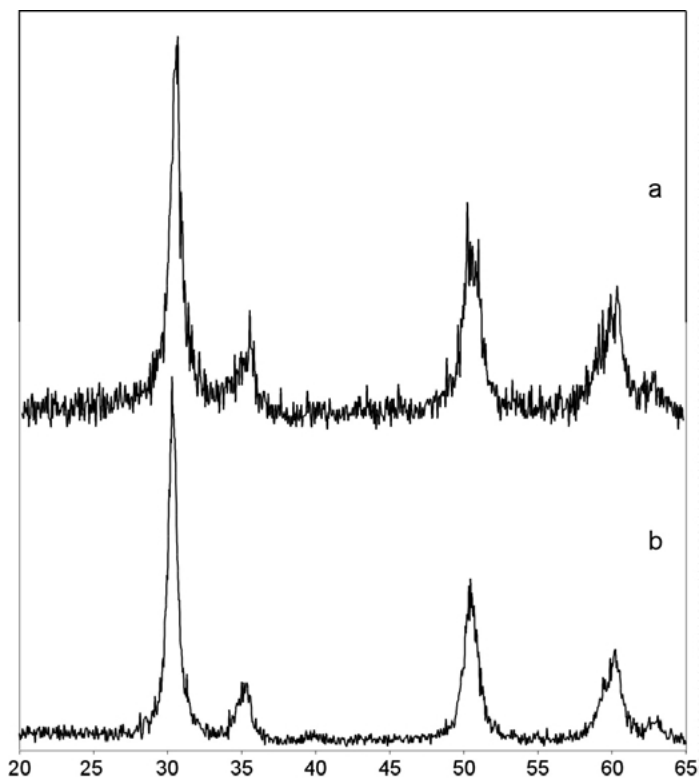
Figure 28. Powder XRD patterns of 3DOM (a) SZ and (b) WZ. Reflections from the tetragonal phase matched PDF#42-1164.

Crystallization of nano-crystal zeolites on the samples was initially carried out without using polyelectrolyte coatings. In this case, the zeolite precursor crystallized into loose zeolitic particles with an average size range of 100-120 nm, resting within the macropores of the material. Figure 29a is an SEM image of ZSM-5 zeolite grown on uncoated 3DOM SZ. It appears that crystallization occurred in the solution filling the pores and the resulting zeolite crystals were retained in the material after filtering and washing the sample.

Because of these observations, the 3DOM zirconia samples were coated with multiple layers of polyelectrolytes before zeolite deposition.[121] Coating the 3DOM zirconia samples with polyelectrolyte layers in the order PSS-PDDA-PSS-PDDA-PSS-PDDA (PDDA = cationic poly(diallyldimethylammonium chloride, PSS = anionic poly(sodium 4-styrenesulfonate) served two important purposes: first to provide a cushion for zeolite nucleation to occur on the surface of the solid; second to provide a positively charged surface to favor the electrostatic interaction with the negatively charged zeolite nuclei and/or precursor. If the last polyelectrolyte layer deposited was negatively charged PSS, zeolite crystals were found only on certain patches of the zirconia surface as shown in Figure 29b.
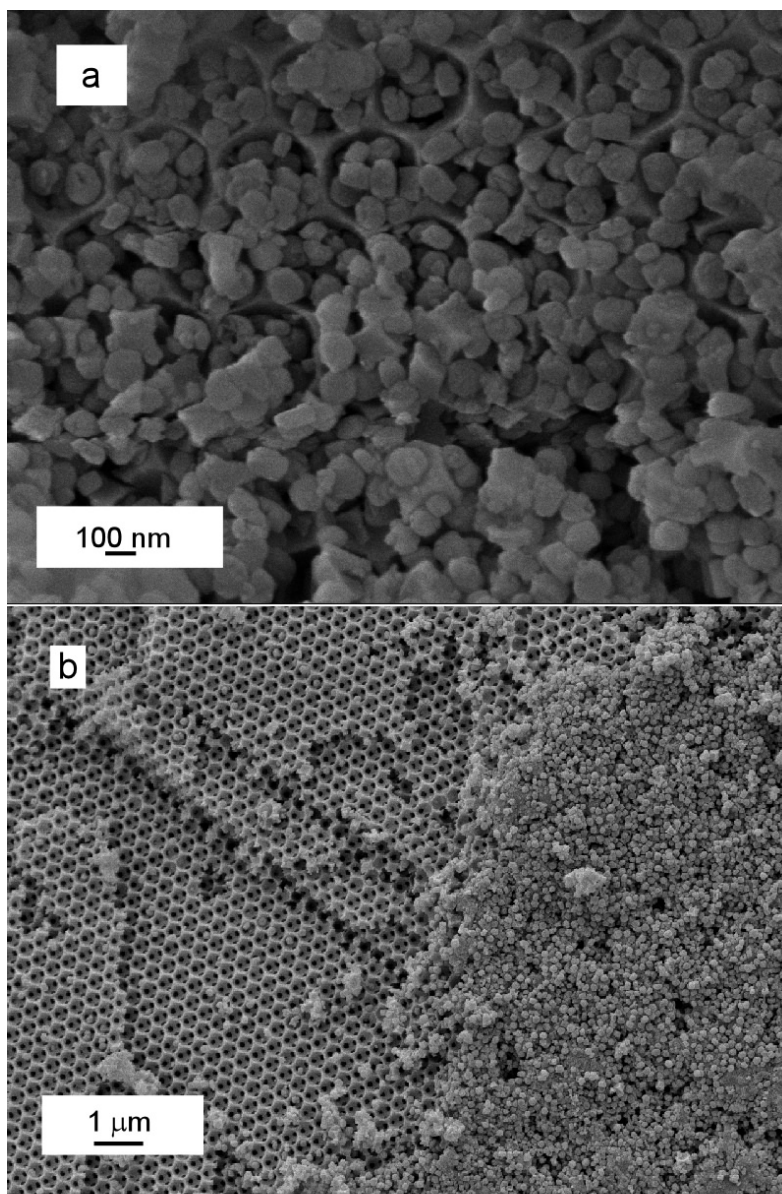
Figure 29. (a) ZSM-5 zeolite crystal growth on 3DOM SZ without polyelectrolyte multilayers. (b) Growth of ZSM-5 crystals with an unfavorable outer-layer charge, provided by negatively charged PSS polyelectrolyte.

Following the above criteria, it was possible to grow continuous and uniform zeolitic layers on top of the 3DOM zirconia samples. Figure 30 shows the product of the as-synthesized zeolitic particles attached to the SZ surface, prepared by using a ZSM-5 precursor solution. The specific surface area of the as synthesized zeolite/SZ sample was found to decrease to about ~87 m^2/g, which can be explained by the possible filling of the structural mesoporsity of the 3DOM material with zeolitic particles. The specific surface area of the calcined sample, however, increased to ~210 m^2/g, as expected due to the increased microporosity in the sample upon removal of the amine template.
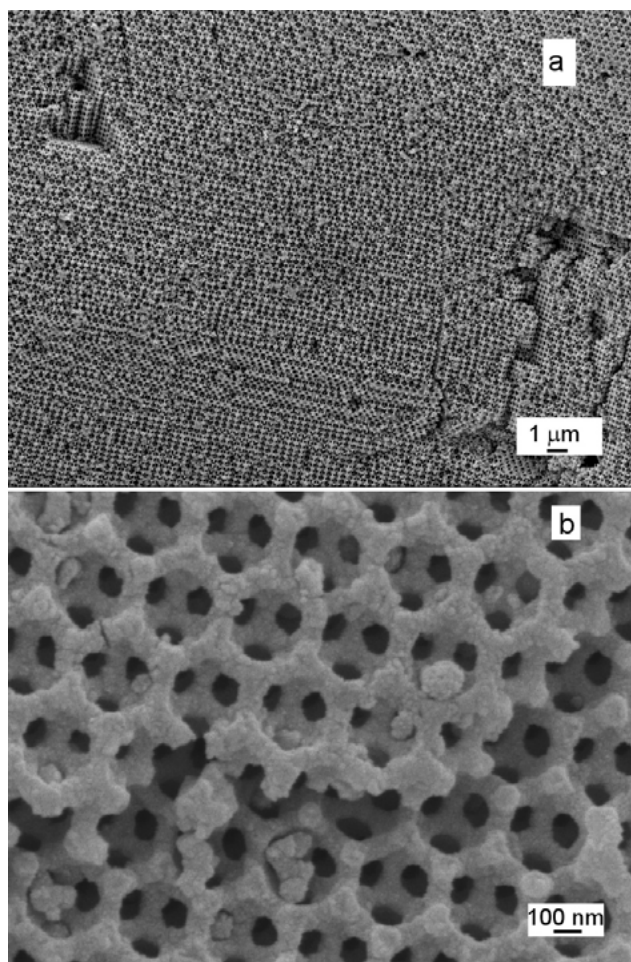
Figure 30. (a) Expanded view of ZSM-5 coated 3DOM SZ. (b) ZSM-5 nanocrystal zeolites appear to cover the 3DOM structure in a uniform and continuous manner with the occasional growth of external particles. (A positively charged outer layer of the zirconia catalysts was prepared by depositing six layers of polyelectrolytes of cationic poly(diallyldimethylammonium chloride) PDDA and anionic poly(sodium 4-styrenesulfonate) PSS in the order PSS-PDDA-PSS-PDDA-PSS-PDDA. The polyelectrolyte-coated zirconia supports were then soaked in clear zeolite precursor solutions, first at room temperature for 1 d, then at 100 °C for 1–3 d. The molar ratios in the clear precursor solutions were 100 SiO_2 : 0.6 Al_2O_3 : 42 TPAOH : 1233 H_2O. The dried products were calcined in air at 550 °C.)

The growth of zeolite-Y nanocrystals on the zirconia samples required the same polyelectrolyte pretreatment used to grow the ZSM-5 layer. Figure 31 shows the resulting samples obtained after hydrothermal crystallization for 24 h, 48 h, and 72 h. Initially, zeolite nucleation was observed only at certain spots on the zirconia surface, as shown by the formation of sparingly dispersed zeolitic particles on the surface after 24 h of hydrothermal reaction. After 48 h, however, well-developed zeolite crystals covered the surface in a uniform fashion, without closing the macropores. Some excess zeolite crystallization and growth occured in cracks that are normally found in 3DOM structures (Figure 31c). It is likely that more precursor solution was deposited in these cracks, leading to the formation of excess zeolite particles. After 72 h of hydrothermal reaction, the size and amount of deposited zeolite began to close the macropores.
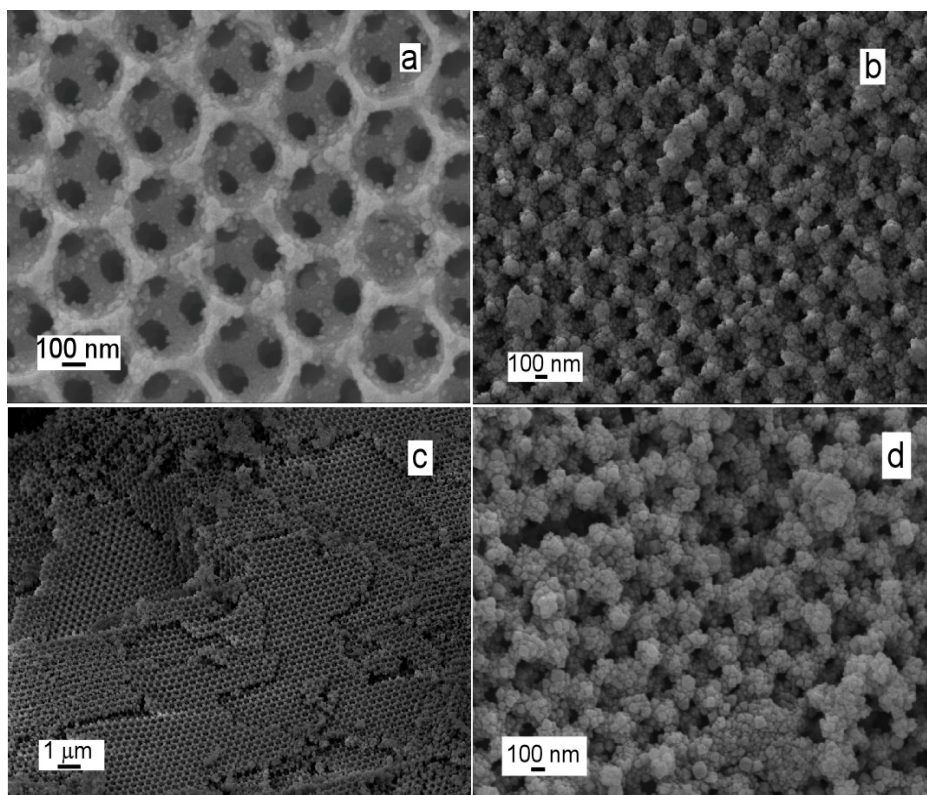
Figure 31. SEM images of zeolite-Y coated 3DOM WZ. (a) After 24 h of hydrothermal reaction, (b) after 48 h of hydrothermal reaction, (c) expanded view of sample (b), and (d) after 72 h of hydrothermal reaction. (The molar ratios in the clear precursor solutions were 0.5 Na_2O : 5.5 TMAOH : 10 SiO_2 : 2.3 Al_2O_3 : 570 H_2O. The dried products were calcined in air at 450 ˚C.)

At this stage, seed solutions for zeolites were induced to crystallize and grow on top of 3DOM SZ and WZ via a polyelectrolyte interface. The absence of such polyelectrolyte multilayers and the incorrect choice of the final surface charge (negatively charged PSS) led to formation of larger zeolite particles, which are proposed to grow in the liquid phase. The growth of the zeolite layer led to a measurable increase in the surface area of the 3DOM structures, a result expected based on the increased microporosity of the material. To verify the zeolitic phase of the coatings, other physicochemical investigations remain to be carried out, including [27]Al solid-state to ascertain the presence of framework (tetrahedral) aluminum species in the material, transmission electron microscopy and electron diffraction to analyze the zeolite layer on top of the crystalline zirconia, elemental analysis to determine the amount of zeolite deposited, and XRD to show the presence of both crystalline species.

7.3 Functionalization with polymeric guests (hydrogels) in the voids

One functional macroporous material, which was studied with partial funding by the ARO, was a periodic structure of macroporous hydroxyapatite-containing calcium phosphates.[122] Hydroxyapatite, $Ca_5(PO_4)_3OH$, is a bioceramic analogous to the mineral component of bone. Its biocompatibility and osteoconductive properties make it desirable as an implant material and drug delivery agent. We prepared 3DOM materials containing the bioceramic hydroxyapatite, as well as other calcium phosphate and carbonate phases. The interstitial spaces of the colloidal crystal were penetrated by a water-alcohol co-solvent solution of calcium nitrate and phosphoric

acid. Calcination in the range 475–1000 ˚C removed the polymer and promoted crystallization of calcium phosphate phases in the pore walls. The best combination of composition and three-dimensional order was found in a crystalline hydroxyapatite/tricalcium phosphate templated with 375 nm size spheres and calcined at 700 ˚C. An *in vitro* antibiotic drug (norfloxacin) release application was tested using this product. The porous sample was charged in a saturated solution of norfloxacin in simulated body fluid. The UV-visible absorbance spectrum of the filtrate was noticeably lower in intensity compared to that of the original charging solution, suggesting an adsorption of 5.9 wt%. A distinct release curve was obtained from exposure of the charged sample to simulated body fluid at 37 ˚C (Figure 32). However, release of norfloxacin occurred very quickly, within one hour.
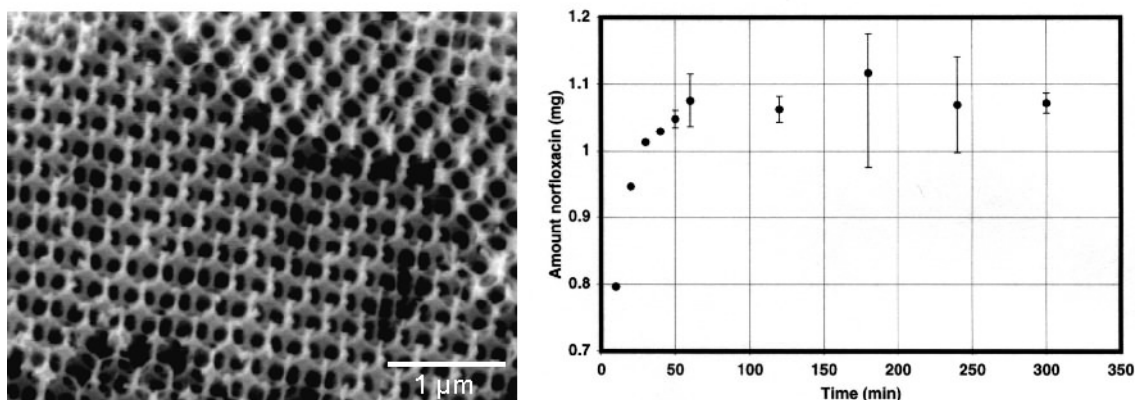
Figure 32. Left: SEM image of a 3DOM hydroxyapatite-containing calcium phosphate prepared at 700 ˚C. Right: Time-release curve of norfloxacin from the charged material shown on the left in simulated body fluid at 37 ˚C.

This result motivated us to investigate functionalization of 3DOM materials with surface groups or other modifiers that can better control the release of drugs and other guest species. In particular we investigated the use of hydrogels to coat the surface of 3DOM materials, because hydrogels can expand and contract in response to external stimuli, including pH, ionic strength, solvent composition, temperature, electric fields, and light.[123,124] Volume changes of a hydrogel coating on the porous support are expected to affect guest transport through the support. 3DOM zirconia was chosen as the support for modification, because it could be more easily synthesized with a high degree of order than hydroxyapatite, because it is chemically stable over a wide pH range, and because of our extensive experience with 3DOM zirconia.

The hydrogel poly(2-hydroxyethyl methacrylate) (PHEMA) from the monomer 2-hydroxyethyl methacrylate (HEMA, Figure 33) was chosen for this study, since expansion of PHEMA due to water uptake has been previously studied.[125]
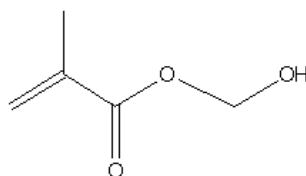
Figure 33. The structure of monomer 2-hydroxyethyl methacrylate (HEMA).

40

HEMA was dissolved in a chloroform/methanol mixture, followed by addition of *N,N'*-methylenebisacrylamide crosslinker and 2,2'-azobisisobutyronitrile (AIBN) initiator. 3DOM zirconia was placed into the homogenized solution and was immediately wetted as air was replaced by fluid within the voids. The color of the 3DOM zirconia was simultaneously red-shifted, indicating that a fluid with a higher index of refraction had filled the voids. The resulting cloudy dispersion was stirred at 50°C for 30 min, then filtered and air-dried. It was subsequently heated to 105°C for 12 h to complete the polymerization of PHEMA inside the pores. Using this general technique, two separate coating strategies were investigated. In the first strategy, up to four multiple coatings of an 8% HEMA solution were applied to as-synthesized 3DOM zirconia. In the second method, coatings of varying concentrations of HEMA were made in a single step. The presence of PHEMA in the samples was confirmed by FT-IR spectroscopy. Thermal analysis of a typical sample (single coating of 8% PHEMA solution) in air indicated that ca. 7.5 wt% PHEMA was present, which was lost by combustion between 300 and 400 °C.

Optical measurements were employed to determine whether PHEMA was adsorbed on the external surface of the particles or whether it formed a coating inside the pores. Continuous red shifts of the stop band positions with increasing PHEMA loading indicated that internal coating must have occurred (Figures 34 and 35).
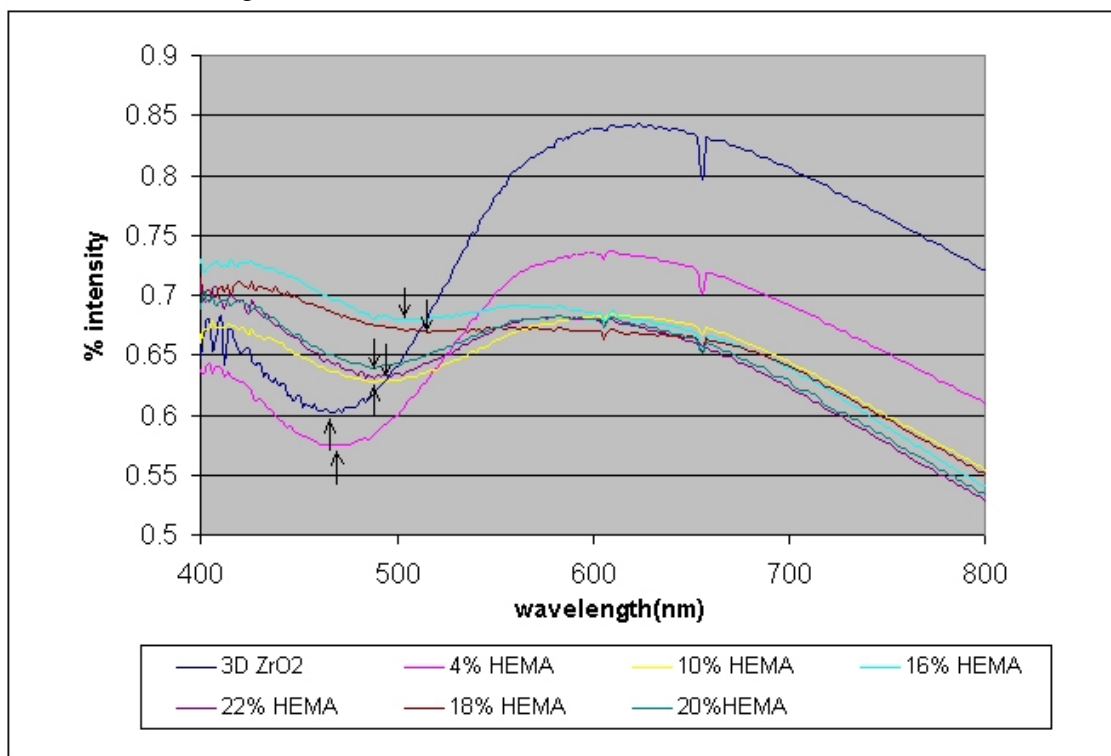
Figure 34. UV-vis reflectance spectra of 3DOM zirconia samples coated with varying concentrations of HEMA.
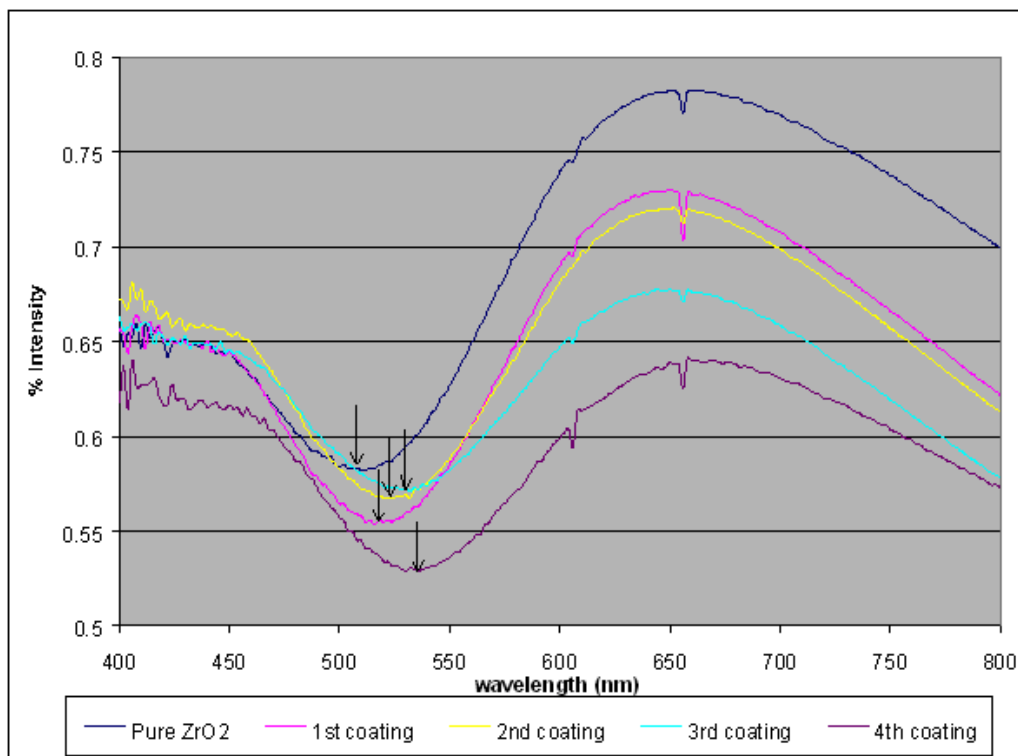
Figure 35. UV-vis reflectance spectra of 3DOM zirconia showing the red shift of the (111) stop band for increasing numbers of PHEMA coatings.

7.3.1 Hydrogel coatings on 3DOM supports by ATRP

In the above procedure, the loading of PHEMA and the associated shift in stop-band position were controlled by varying HEMA concentrations in the precursor solution. Better control over coating formation was achievable by employing atom transfer radical polymerization (ATRP), a living polymerization reaction based on well-defined alkyl halide end groups, which favors steady growth of polymer chains on an appropriately functionalized surface.[126] 3DOM ZrO_2 or 3DOM SiO_2 were first surface modified with *p*-chloromethyl phenyltrichlorosilane groups, resulting in covalently attached surface groups with alkyl chloride-terminal functionality. The ATRP method ensured that subsequent exposure to monomers (HEMA, methyl methacrylate, or N-isopropylacrylamide) in the presence of a catalyst (CuBr or CuCl with pentanemethyldiethylenetriamine or 2,2'bipyridine) led to a uniform coating without additional polymerization away from the surface. Further advantages of this method were the lower reaction temperature to form a hydrogel coating (room temperature vs. 60–105 ˚C), the ability to control polymer loading by reaction time rather than precursor concentration (see Figure 36), and the possibility to incorporate more hydrogel in the pore system, resulting in a larger stop band shift (see Figure 37).
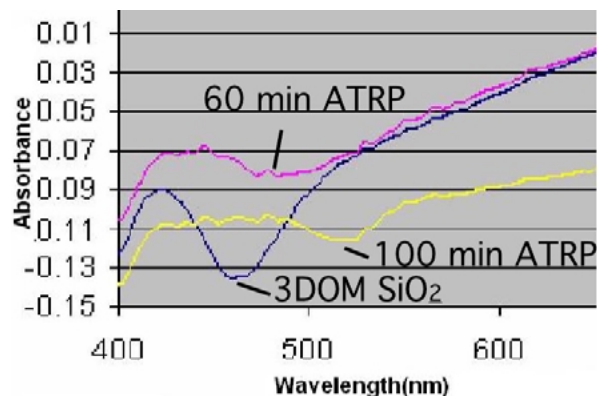
Figure 36. UV-vis reflectance spectra of 3DOM SiO₂ functionalized with *p*-chloromethyl phenylsiloxane groups (blue) and then reacted with an *N*-isopropylacrylamide-based ATRP solution for 60 min (pink) or 100 min (yellow). The stopbands shifted toward the red as the reaction time and polymer loading increased. (A solution of 6 g *N*-isopropylacrylamide, 3 mL water, 3 mL methanol and 0.35 mL pentamethyldiethylenetriamine was outgassed by three cycles of freezing and thawing, then cannulated into a mixture of 0.1 g surface-functionalized 3DOM SiO₂ and 0.08 g CuCl. The reaction was terminated by exposure to air.)

— 3DOM ZrO₂
— 3DOM ZrO₂, functionalized with *p*-CMPTS
— 3DOM ZrO₂ after 60 min ATRP with HEMA
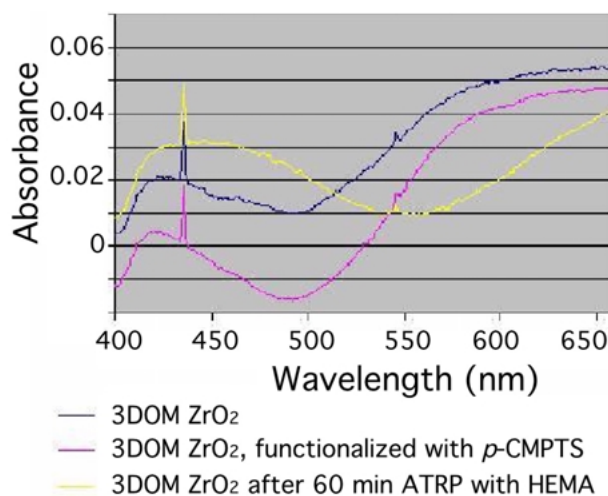
Figure 37. UV-vis reflectance spectra of 3DOM ZrO₂ (blue curve), 3DOM ZrO₂, functionalized with *p*-chloromethyl phenyltrichlorosilane (pink curve) and then coated with PHEMA in a 60 min ATRP reaction (yellow curve). The 65 nm red-shift of the stopband is significantly larger than any red-shift obtainable by the previous coating method, due to greater incorporation of PHEMA in the voids (43 wt% based on TGA analysis). (A solution of 7 g HEMA, 7 mL water, 0.28 mL pentamethyldiethylenetriamine was outgassed by three cycles of freezing and thawing, then cannulated into a mixture of 0.2 g surface-functionalized 3DOM ZrO₂ and 0.065 g CuBr. The reaction was terminated by exposure to air after 60 min room temperature reaction.)

8. Nanomechanical testing of PMMA colloidal crystals, 3DOM silica films and silica/PMMA colloidal crystal composites by depth-sensing indentation *(This work was carried out in a collaboration with Y. Toivola and R. F. Cook at the Department of Chemical Engineering and Materials Science, University of Minnesota.)*

For many potential applications of 3DOM materials, it is important to know and control the mechanical properties of these macroporous solids. Because currently no good mechanical models exist for porous solids in the pore size regime of a few hundred nanometers, much effort was expended on developing a model describing the response of 3DOM materials to nanoindentation. Depth sensing indentation (DSI) was employed to quantify the mechanical

43

integrity of colloidal crystals and 3DOM samples. The technique involves the measurement of load-displacement curves as an indenting probe is lowered into a sample and subsequently raised. Elastic and plastic deformations can be monitored. Initially tests were carried out on free-standing granular samples and subsequently on thin films of PMMA colloidal crystals and 3DOM silica on flat soda-lime glass substrates. The contact responses of the 3DOM films were captured using two different indentation tips: a diamond Berkovich (three-sided) pyramid (tip radius ca. 50 nm) or sapphire hemisphere (radius = 150 µm) over a load range of 1 mN to 100 mN. Scanning electron microscopy (SEM) was used to image and quantify relevant microstructural features, such as pore diameter and cell wall thickness, in addition to features relevant to dimensions of fabricated devices. The indentation contact responses were interpreted along with the SEM images of residual indentation impressions to develop an understanding of the deformation mechanisms of these ordered silica foams.

Conventional instrumented indentation accomodates elastic and volume-conserving plastic deformation. For Berkovich indentations, models are well developed for dense structures where a quadratic relationship is observed between load (P) and displacement (h): $P = \alpha h^2$. For a spherical indenter, deconvolution models for dense structures follow the relationship $P = \alpha h^{1.5}$. For macroporous solids of the type investigated here, models could not be previously determined experimentally, because suitable materials had not been synthesized. Our ability to prepare 3DOM solids allowed us to develop a better understanding of the mechanical properties of porous materials.

The following materials were tested:
- PMMA colloidal crystal, free-standing piece
- 400 nm pore spacing, free-standing 3DOM SiO_2
- 1000 nm pore spacing 3DOM SiO_2 film on flat soda lime glass, ca. 3.8 µm thick
- 600 nm pore spacing 3DOM SiO_2 film on flat soda lime glass, ca. 2.7 µm thick
- PMMA colloidal crystal film on flat soda lime glass
- composite film of PMMA colloidal crystal infiltrated with silicon tetraethoxide, hardened at room temperature, but not calcined; on flat soda lime glass

Measurements were not well reproduced with free standing pieces; the discussion below therefore refers to film samples. The experimental setup and typical indentation traces are shown in Figure 38.

DEPTH–SENSING INDENTATION OF 3DOM SiO$_2$ FILMS
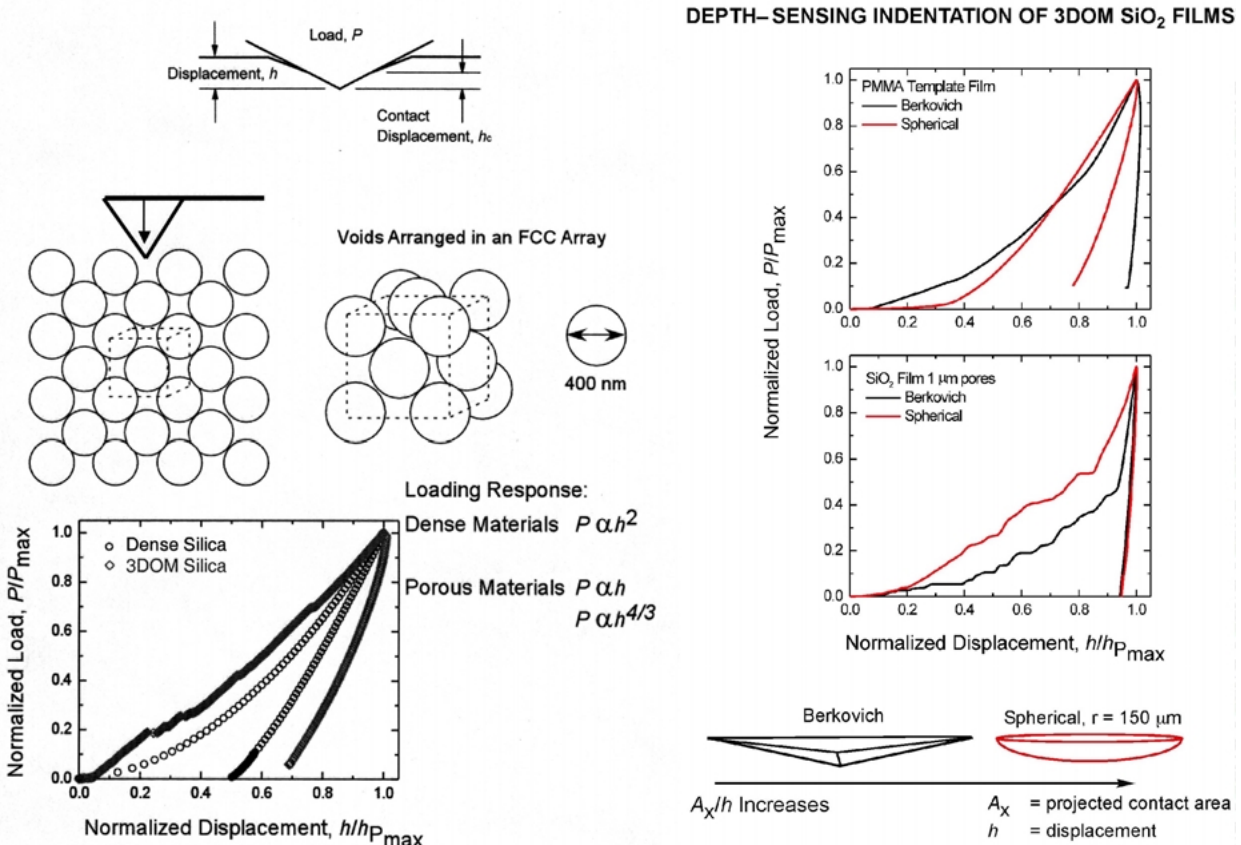
Figure 38. Nanoindentation measurements, showing the geometry of the experiment (top left), normalized load-displacement curves for bulk 3DOM silica compared to dense silica (bottom left), similar curves for thin films of PMMA and 3DOM silica on flat glass supports (top right), and the geometries of the tips employed (bottom right). For 3DOM SiO$_2$, an erratic, "stick-slip" tip response was observed, corresponding to discrete fracture events. By comparison, bulk SiO$_2$ materials and PMMA films displayed a smooth elastic-plastic response in continuous loading traces.

A more detailed discussion of the results for 3DOM silica films follows. This is taken from our publication in *J. Mater. Res.* **2004**, *19*, 260-271.[127]

Figure 39 (left) shows a series of load–displacement (*P*–*h*) indentation responses for peak loads, P_{max}, from 1 mN to 100 mN, using a Berkovich indentation tip for the two 3DOM silica films with average pore spacings of 600 or 1000 nm. For P_{max} = 10 mN, there is a distinction between the two films greater than the variations in *P*–*h* responses. The variations resulted from the fact that microstructural inhomogeneities were larger than or as large as the scale of the indentation. For P_{max} < 10 mN, there is less distinction between the films, and discontinuities in the loading slope are quite apparent. For P_{max} > 10 mN, there is an abrupt change in the slope of the loading trace, from compliant to relatively stiff, as well as a transition in the character of loading slope from discontinuous to continuous (smooth). Distinction between the films was maintained for peak loads through 100 mN. For a hemispherical tip and peak loads of 1 mN to 30 mN, there was no distinction between the two 3DOM silica films.

45
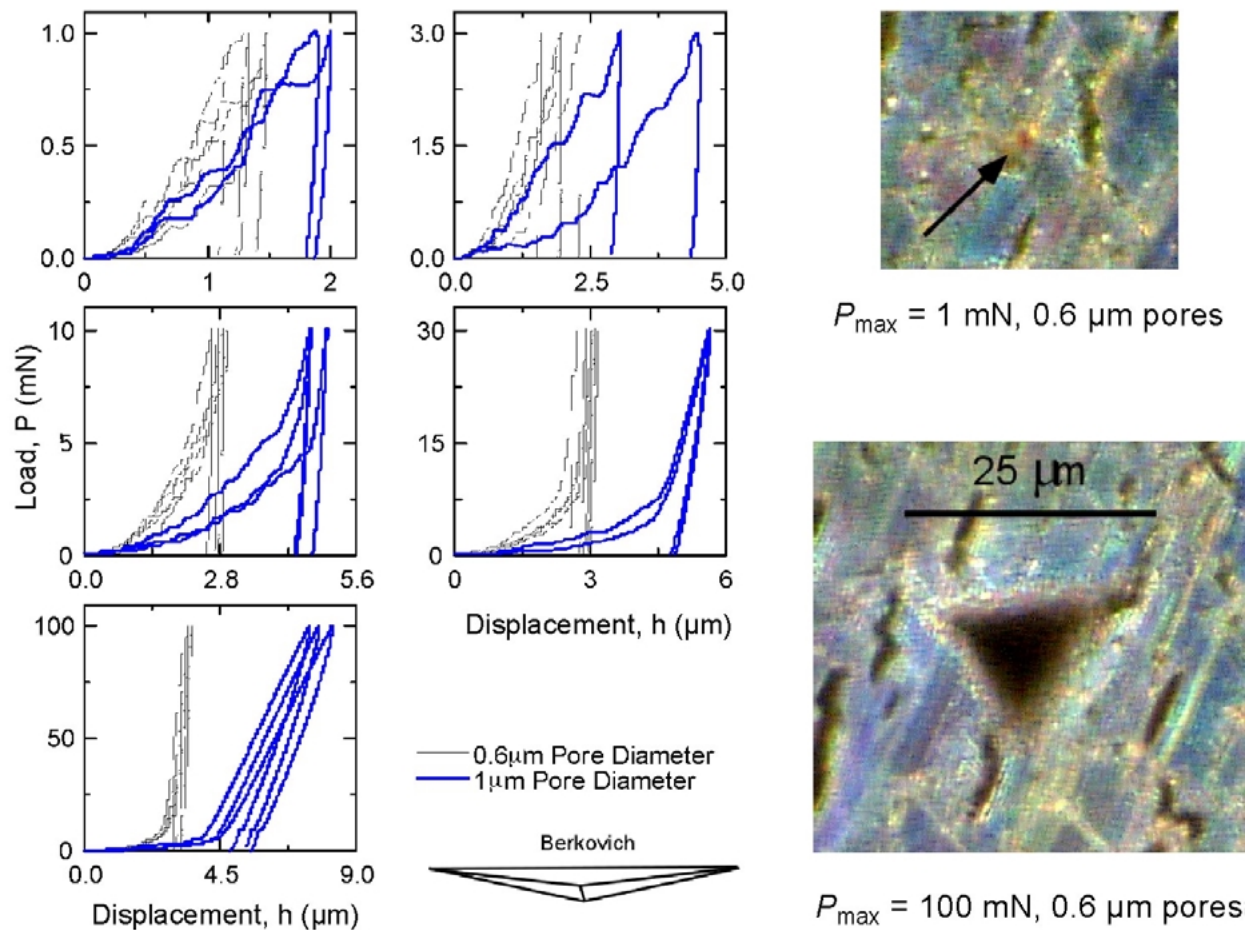
Figure 39. Nanoindentation load-displacement traces for 3DOM silica with 0.6 μm and 1 μm pore diameters under various load ranges. These measurements, which employed a Berkovich indenter, could distinguish between the two samples of different pore sizes. When a spherical indenter which samples a larger area was used, little distinction was possible, especially at lower loads. Optical micrographs for the 0.6 μm pore sample (right) show evidence of plastic deformation.

Figure 40(a) is a plot of a load–displacement contact response of a P_{max} = 1 mN indentation in the 600 nm 3DOM silica film compared to a P_{max} = 100 mN indentation in dense silica. Normalized load and displacement scales are used to highlight differences in the characteristic shape of loading and unloading traces of these porous materials relative to their dense analog. Several discontinuities are apparent in the loading slope of the silica foam, and the unloading slope is nearly vertical. In contrast, the loading slope for dense silica is smooth and continuous with elastic recovery on unloading and much smaller contact hysteresis. Figure 40(b) is an SEM image of the residual indentation impression from a 100 mN peak load Berkovich indentation in dense silica for comparison with that from a 1 mN peak load Berkovich indentation in 3DOM silica shown in Figure 40(c). The residual impressions are comparable in size, although the peak indentation loads are separated in two orders of magnitude. In Figure 40(c) it is apparent that the indentation impression spans several pores and also spans the preexisting cracks in the material remnant from shrinkage during drying and calcination. It is contact with these sorts of microstructural features that probably gives rise to the discontinuities observed in the P–h contact response. Also of note is that the deformation in the impression appears homogeneous as

46

a function of depth (outer to center of indentation impression). Finally, pores adjacent to the contact impression were undeformed, implying that there was no strain transfer to material adjacent to the contact area. This latter observation is in contrast to the image of the indentation in fused silica, in which it is apparent that the residual impression edges are convex, indicating elastic recovery and thus substantial elastic strain beyond the contact impression. Furthermore, in a composite film of PMMA colloidal crystal infiltrated with silica, crack propagation was observed outside the contact, and cracks followed the plane of spheres (Figure 41). The implication is that the modulus/hardness ratio of the 3DOM structure is significantly greater than that of the related denser materials.
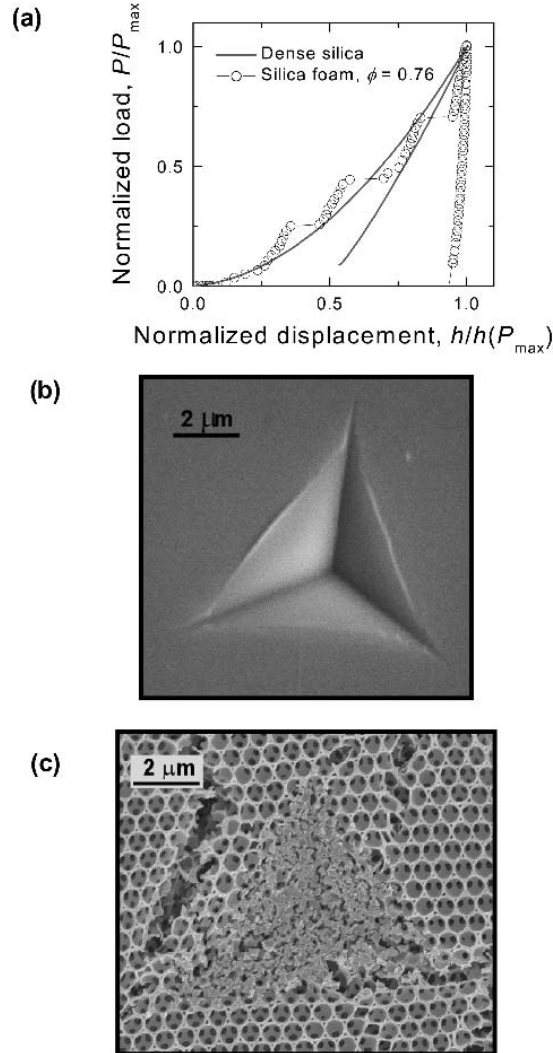
Figure 40. (a) The normalized load-displacement responses of Berkovich indentation in 3DOM silica (P_{max} = 1 mn) and dense silica (P_{max} = 100 mN). The SEM images show residual Berkovich indentation impressions from (b) a 100 mN indentation in dense silica, and (c) a 1 mN indentation in 3DOM silica with a pore spacing of ca. 600 nm. the latter shows homogeneous deformation, which is partly elastic and largely "plastic", predominated by non-volume-conserving cell wall fracture and pore collapse.

47
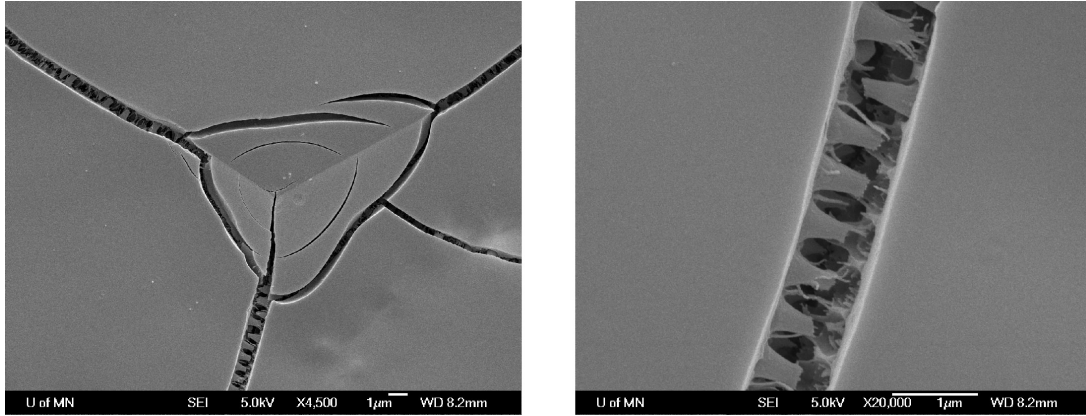
Figure 41. SEM images showing the residual deformation of PMMA sphere/silica composite films on a glass substrate (P_{max} = 30 mN). The film was uncalcined. Cracks propagate outside the contact, following the plane of spheres.

Figure 42 is a schematic cross-sectional diagram of the 1 mN to 100 mN indentations, representing the Berkovich indenter by its equivalent cone and drawn to scale. From this diagram it became apparent that for peak loads of 1 mN and 3 mN, $h(P_{max})$ was less than the film thickness, and thus there was no direct contact with the substrate. For peak loads of 10 mN and 30 mN the average $h(P_{max})$ was very similar and just reached the film–substrate interface. For P_{max}=100 mN, the indentation tip penetrated the substrate. The transitions in the loading slope and character of the P–h traces shown in Figure 39(left) correspond to the onset of densification and compaction of material close to and in contact with the substrate.
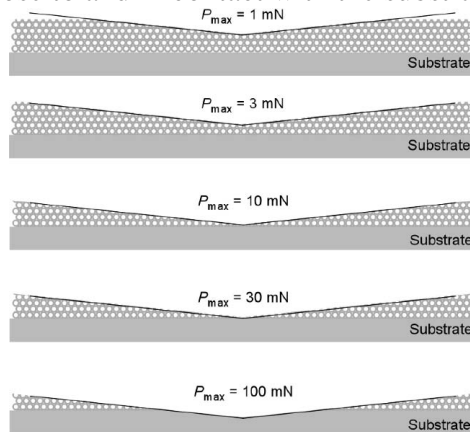
Figure 42. Schematic diagram showing the cross section of indentations with a conical tip into the 600 nm pore spacing 3DOM silica film on a glass substrate with microstructural features, film thickness, indentation tip geometry, and displacements drawn to scale.

8.1 Deformation mechanisms

Observation of the residual contact impression of these 3DOM silica films suggests that the indentation deformation mechanism sequence is (very little) elastic deformation by cell-wall bending, cell-wall fracture, and pore collapse, local densification in a layer adjacent to the indenter face, and, finally, compaction between the indenter and substrate. In reality, the fractured cell wall material accumulates beneath the indentation contact. The materials are highly porous with pore sizes larger than or comparable to the size of the indentation deformations of 1 to 20 µm. The cell wall thickness of the 3DOM materials in this study was of the order approximately 50 nm, and thus indentations could not be contained within a single cell wall

48

(indentation tips typically have a radius of curvature of the order 50 nm). Also important is the fact that 3DOM silica has interconnected porosity, allowing the potential for material to fall not only into the next layer of pores beneath the fractured layer, but also to fall to the layer of pores adjacent to the substrate. It is proposed that the distinction between films observed here at large displacements (>film thickness) is a result of the different amounts of accumulated cell wall material under the indentation contact. The material compacted between the indentation tip and substrate results in a different contact geometry between the indenter–compacted layer system and the substrate, resulting in different *P–h* responses, and thus different geometries will arise from differences in initial film density.

8.2 Definition of a material parameter

The indentation deformation mechanisms in these materials are predominantly nonelastic and nonvolume conserving, rendering the modulus and (especially) hardness obtained from standard *P–h* trace deconvolution methods inapplicable. However, a material parameter that can be used to characterize (and eventually compare) these materials can be obtained from DSI measurements by realizing that these materials lie at a different extreme of idealized mechanical response than that assumed in standard deconvolution methods. In deconvoluting the *P–h* trace, the material is idealized as "elastic–perfectly plastic." For densifying materials here, there is no elastic deformation adjacent to the contact, and the material can be idealized (in compression) as "rigid–perfectly plastic." Of course, the "plasticity" in mind here is the irreversible nonvolume conserving deformation associated with pore collapse, and the characteristic stress associated with the plastic process is the crushing pressure of the structure. Indentation *P–h* traces can be transformed into pressure–volume, *p–V*, traces for the 3DOM films through the shape of the (assumed rigid) Berkovich indenter profile at large contact depths. Figure 43 shows a plot of the resulting *p–V* traces from the 1 mN indentation traces in 3DOM silica, a PMMA opal/silica composite film and several dense reference materials. The indentation pressure is approximately constant over three to four orders of magnitude of swept indenter volume. Notwithstanding the scatter, it also appears that the crushing pressure of the larger pore film is slightly smaller, 0.015 (±0.069) GPa for 1000 nm 3DOM silica compared to 0.026 (±0.081) GPa for 600 nm 3DOM silica, and both are about two orders of magnitude less than that for dense silica (0.01–0.06 GPa compared with 6 GPa). Plots such as Figure 43 should allow property changes generated by processing to be assessed and provide an objective comparison of the mechanical behavior of similar porous brittle materials.
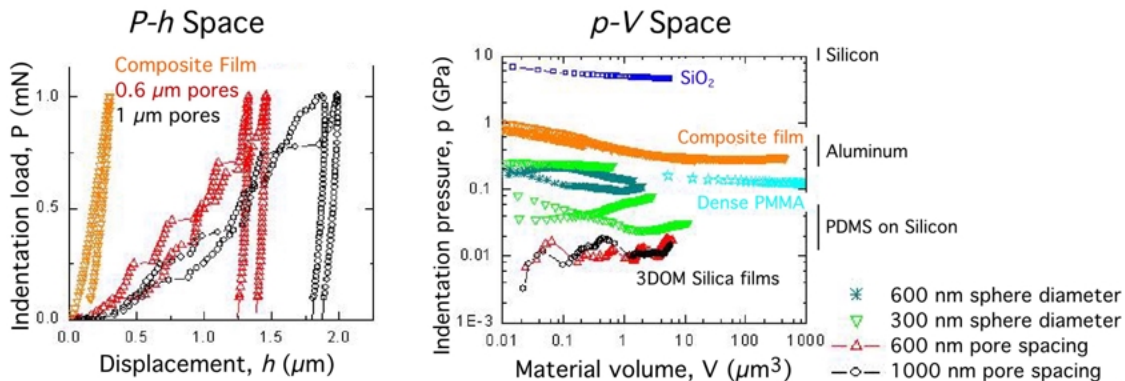
Figure 43. Plots of indentation contact responses in load-displacement (*P-h*) and pressure volume (*p-V*) space for films of the compositions indicated.

This depth-sensing indentation study of 3DOM silica films indicated that the dominant indentation deformation mechanism was cell wall fracture and subsequent pore collapse. Deformation was contained within the contact area; no deformation was observed adjacent to residual contact impressions in the porous films but cracks propagated in denser composite films. For displacements comparable to film thickness, fractured cell wall material accumulated beneath the contact leading to densification and material compaction. Indentations with a Berkovich indentation tip were more sensitive to microstructural features than a hemispherical indentation tip, allowing distinction between films of different pore sizes in load–displacement space during Berkovich indentations. A translation of Berkovich load–displacement responses to pressure–volume space revealed the similarity between the two materials, with similar crushing pressures for shallow indentations. Based on the p-V plots, average crushing pressures followed the order $p_{dense\ silica} > p_{composite} > p_{PMMA\ colloidal\ crystal} > p_{3DOM\ silica}$.

9. An example of a multifunctional system: 3DOM SiO$_2$/TiO$_2$ composites as systems to evaluate photonic crystal effects on photocatalytic activities *(This section is adapted from the Ph.D. thesis of Mohammed A. Al-Daous, University of Minnesota, 2003.)*

The brightly colored 3DOM SiO$_2$/TiO$_2$ nanocomposites described earlier were envisioned to lend themselves to an interesting application, which combines photonic crystal effects of the 3DOM structure with photocatalytic activity of titania. Interaction of the stop band with light is known to cause nonlinear dispersion,[128] where the group velocity of light becomes anomalously small near the wavelength of the stop band.[129] Consequently, light intensity is localized in the low refractive index region when its wavelength is to the blue of the stop band and localized in the high dielectric regions when its wavelength is to the red of the stop band.[6,130] This effect can be used to modify photoemission properties and influence photocatalytic reactions. It has long been known that emission of a lumophore depends on the properties of the lumophore and on its local optical surroundings.[131] A photonic crystal provides unique surroundings, enabling complete inhibition of spontaneous emission in the photonic band gap[5] and suppression of emission in the stop-band range.[132,133] According to the sum rule for modified spontaneous emission rates, inhibition of spontaneous emission for one range of frequencies is accompanied by enhancement of rates at other frequencies.[134] As a result, emission is amplified at the edge of the stop-band, in particular, the long-wavelength portion of the emission is enhanced at the blue edge of the stop-band.[135-140] In a photocatalytic system based on semiconductor particles, coupling the emission produced by recombination between photoinduced charge carriers in semiconductor particles[141,142] with the optical stop band of a photonic crystal[2,5,143] is envisioned to influence the photocatalytic function of the semiconductor. In particular, *if side reactions, such as electron-hole recombination in the bulk of the semiconductor can be suppressed by eliminating certain emissive pathways through nonlinear dispersion effects, one would expect an increase in the charge carrier density near surface or interfacial sites, resulting in enhanced emission intensity from the corresponding states and also in increased photocatalytic reactivity of the system.*[144,145]

We have tested this hypothesis by comparing the photooxidative degradation of a dye in the presence of photonic (3DOM) and chemically identical nonphotonic SiO$_2$/TiO$_2$ nanocomposites. The 3DOM SiO$_2$/TiO$_2$ nanocomposite is an example of a multifunctional system in which titania in the wall skeleton provides photocatalytic sites, silica enhances sorption of the dye, and the

periodic structure may lead to photonic crystal effects. The material was prepared by combining sol-gel[146] and polymer colloidal crystal-templating syntheses.[15,17,18] Titanium dioxide is a well-studied semiconductor photocatalytic material due to its photo-corrosion stability and activity of the photo-generated species.[141,147] The silica medium facilitates the adsorption of organic species and has also been reported to transfer adsorbed organic compounds to active sites on the TiO_2 domains,[148,149] improve the dispersion of the active TiO_2 particles formed in the matrix, and produce materials with a relatively high surface area.[150,151] The resulting catalytically active sites in this composite material are known to include highly dispersed supported-titania domains and/or coordinatively unsaturated surface titanium species, as well as interfacial Ti ions at SiO_2-TiO_2 cross-links.[152,153]

To combine the photonic stop band effects with the photocatalytic action of the TiO_2/SiO_2 composite catalyst, the wavelength of the characteristic first-order stop band of the 3DOM catalyst was designed to overlap with various sections of the luminescence bands of titanium emitting centers in the catalyst by adjusting two parameters: the sphere size of the colloidal crystal template and the refractive index contrast of the material in an aqueous suspension.[7,8] The samples were compared with chemically identical but nonperiodic samples which did not exhibit any stopbands. The photocatalytic reactivity of the material was evaluated in the photodecomposition reaction of rhodamine-6G in aqueous solution, a species that adsorbs on SiO_2 but not on TiO_2.[148,149] Using initial rate kinetics,[154] small differences were observed for absorption and photodecomposition rate constants for crushed materials compared to open porous materials. The open periodic 3DOM structure resulted in a small increase in the dye adsorption rate constant due to improved accessibility to active sites and/or increased surface concentration of the dye in the more open 3DOM catalyst structure with its higher surface area (169 m^2/g vs. 115 m^2/g in the crushed sample). The photodecomposition rate of the dye increased by ca. 50% for a periodic sample compared to a crushed sample. However, the differences are within one to two standard deviations of error and are therefore probably not significant. Thus, while these brightly colored 3DOM SiO_2/TiO_2 composites provided advantages of highly accessible surfaces for large molecules, good sorption of organic dyes and photocatalytic activity, a photonic effect on photocatalysis could not be unambiguously identified. A major reason may be that non-radiative recombination processes predominate in this system.

10. Reactivity of 3DOM solids (bioactive glasses)

Another application of 3DOM materials involves mineralization of bioactive glass compositions with a 3DOM architecture, materials with potential utility as bone graft substitutes. This work was funded mostly from other sources but is of relevance to the current project, because it concerns the reactivity of the open 3DOM structure in fluid systems. Bioactive glasses are materials that form a biologically compatible hydroxycarbonate apatite (HCA) layer at the interface with bone *in vivo*. This layer allows the glass to establish a continuous bond with bone. An HCA layer can be formed on the surface of bioactive materials when they are soaked in simulated body fluid (SBF), an aqueous solution that has approximately the same ion concentration and pH as human blood plasma. Traditionally, bioactive glasses have been prepared from a melt of glass components or from sol-gel precursors. We have investigated the use of colloidal crystal templating to produce 3DOM bioactive glasses (mixed SiO_2/CaO compositions). *In vitro* hydroxycarbonate apatite growth was studied by soaking the bioactive glass in SBF at body temperature. The formation of a hydroxycarbonate apatite layer on the glass

51

was followed by diffraction, microscopic, spectroscopic and chemical analysis. We demonstrated that the 3DOM bioactive glass exhibited faster growth of apatite than a non-templated control sample, probably due to the more accessible surface in the 3DOM material. 3DOM glasses possess several features relevant for bioactive materials that result in their faster dissolution and more rapid growth of HCA in SBF. These features include (1) the size of the overall 3DOM particle (up to mm-size), which should prevent rejection of the particle by the body defense system; (2) the large pores which permit facile transport of SBF and probably also natural body fluids; (3) the thin walls which are generated by filling interstices between close-packed templating spheres; and (4) the relatively large accessible surface. One interesting observation during the mineralization process was the formation of an opal-like HCA structure from the 3DOM parent, which was originally formed from an opal-like latex sphere array. This is not a double templating process but a reactive transformation to a sphere array structure, something which had not been observed before. This unusual transformation is illustrated in Figure 45. The following mechanism for mineralization of 3DOM CaO/silica is proposed, which is based on what is known in the literature on a molecular level[155] and our observations of morphology changes. During the early stages of exposure to SBF, silica was dissolved from the highly accessible walls and then repolymerized on the surface, where it acted as a nucleation site for deposition and growth of amorphous calcium phosphate nodules. Since silica was the predominant phase in the walls, the walls became thinner and eventually disappeared as calcium phosphate grew. This growth occurred mainly from the inside of the voids, which was more accessible to additional ions. This process resulted in the observed sphere-aggregate structure. Additional incorporation of hydroxide and carbonate ions led to crystallization of the apatite product, which continued to grow as long as sufficient nutrients were available. This work has now been published.[156]
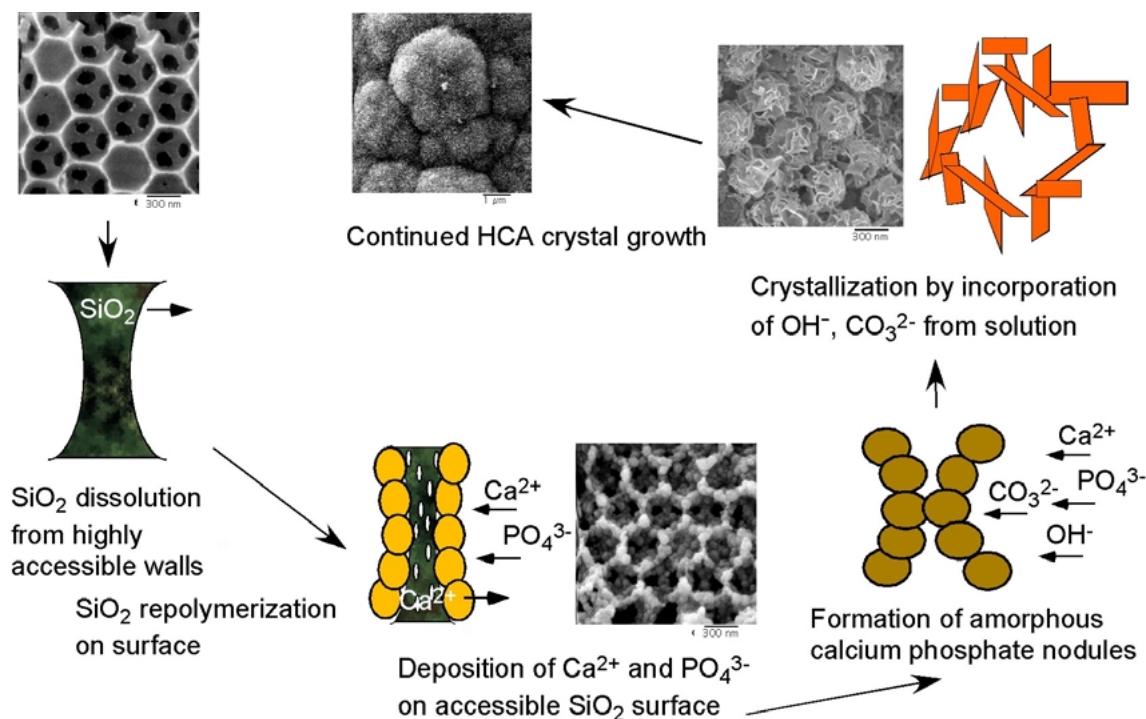
Figure 44. Proposed mechanism for the transformation of a 3DOM bioglass with a 20% CaO/80% SiO$_2$ composition to hydroxycarbonate apatite (HCA) in simulated body fluid (SBF).

52

11. Conclusion

Based on the knowlegde and experience accumulated in this study, as well as on other developments during the project period, it is now possible to synthesize three-dimensionally ordered macroporous oxides in multigram quantities and prepare supported thin films and free-standing monoliths of various 3DOM compositions. Synthesis optimization of the pure inorganic phases has proved to be tantamount to improving the properties of 3DOM solids, in particular optical properties. Materials properties can then be tuned by surface functionalization via small molecules, macromolecules, or inorganic clusters with the techniques developed in this research project. Processing of 3DOM materials is possible using both inorganic and polymeric matrices. By appropriate surface modification, the porous solids can be compatibilized with a specific matrix for applications in pigmenting, coating and camouflage. The nanomechanical testing method can now provide feedback about the effects of composite formation on mechanical properties. When multiple methods outlined in this report are combined, it is possible to create complex multifunctional structures, sometimes with hierarchical feature sizes, including the dual catalyst systems and bioactive host-guest structures described above.

12. List of papers submitted under ARO sponsorship:

(a) Papers published in peer-reviewed journals:
- Schroden, R. C.; Stein, A.; "3D Ordered Macroporous Materials", *Colloids and Colloid Assemblies: Synthesis, Modification, Organization and Utilization of Colloid Particles*, edited by Frank Caruso, Wiley-VCH, Weinheim, Germany, **2004**, 465-493.
- Toivola, Y.; Stein, A.; Cook, R. F.; "Depth-Sensing Indentation Response of Ordered Silica Foam", *J. Mater. Res.* **2004**, *19*, 260-271 (note: this collaborative work was not directly sponsored by ARO, but its content relates closely to this project).
- Stein, A.; "Advances in Microporous and Mesoporous Solids—Highlights of Recent Progress", *Adv. Mater.* **2003**, *15*, 763-775.
- Al-Daous, M. A.; Stein, A.; "Preparation and Catalytic Evaluation of Macroporous Crystalline Sulfated Zirconium Dioxide Templated with Colloidal Crystals", *Chem. Mater.* **2003**, *15*, 2638-2645.
- Sokolov, S.; Bell, D.; Stein, A.; "Preparation and Characterization of Macroporous α-Alumina", *J. Am. Ceram. Soc.* **2003**, *86*,1481-1486.
- Sokolov, S.; Stein, A.; "Preparation and Characterization of Macroporous γ-$LiAlO_2$", *Mater. Letters* **2003**, *57*, 3593-3597.
- Zhang, K.; Yan, H.; Bell, D. C.; Stein, A.; Francis, L. F.; "Effects of Materials Parameters on Mineralization and Degradation of Sol-gel Bioactive Glasses with 3D-ordered Macroporous (3DOM) Structures", *J. Biomed. Mater. Res.* **2003**, 66A, 860-869.
- Yan, H.; Sokolov, S.; Lytle, J. C.; Stein, A.; Zhang, F.; Smyrl, W. H.; "Colloidal-Crystal-Templated Synthesis of Ordered Macroporous Electrode Materials for Lithium Secondary Batteries", *J. Electrochem. Soc.* **2003**, *150*, A1102-A1107.
- Schroden, R. C.; Al-Daous, M.; Sokolov, S.; Melde, B. J.; Lytle, J. C.; Stein, A.; Carbojo, M. C.; Fernández, J. T.; Rodríguez, E. E.; "Hybrid Macroporous Materials for Heavy Metal Ion Adsorption", *J. Mater. Chem.* **2002**, *12*, 3261-3267.
- Melde, B. J.; Stein, A.; "Periodic Macroporous Hydroxyapatite-containing Calcium Phosphates", *Chem. Mater.* **2002**, *14*, 3326-3331.
- Schroden, R. C.; Al-Daous, M.; Blanford, C. F.; Stein, A.; "Optical Properties of Inverse Opal Photonic Crystals", *Chem. Mater.* **2002**, *14*, 3305-3315.

(b) Manuscripts submitted, but not yet published:
- Lytle, J. C.; Yan, H.; Ergang, N. S.; Smyrl, W. H.; Stein, A.; "Structural and electrochemical properties of three-dimensionally ordered macroporous tin(IV) oxide films", *J. Mater. Chem.* **2004**, in press.

(c) Papers presented at meetings or in departments, but not published in conference proceedings:
- Stein, A.; "Colloidal Crystal-Templated Macroporous Solids for Catalytic Applications", Symposium: "Materials Design in Catalysis", International Conference on Materials for Advanced Technologies, Singapore, Dec. 10, 2003.
- Stein, A.; "Functional Nanostructures Prepared by Colloidal Crystal Templating and Pseudomorphic Transformations", Symposium: "Non-traditional methods for patterning", Fall 2003 MRS Meeting, Boston, Dec. 4, 2003.
- Stein, A.; Lytle, J.; Ergang, N.; Sokolov, S.; Yan, N., "Three Dimensionally Nanostructured Anode and Cathode Materials Prepared by Colloidal Crystal Templating", Symposium on 3D Battery Architectures, 204th Meeting of the Electrochemical Society, Orlando, Florida, Oct. 13-15, 2003.
- Stein, A.; "On the Aesthetics and Functionality of Porous Solids". Department of Chemistry, University of Toronto, Toronto, Canada, August 22, 2003.
- Stein, A.; "Colloidal Crystal Templating of Porous Solids for Applications in Photonics and Beyond", Department of Chemistry, Fudan University, Shanghai, China, July 7, 2003.
- Stein, A.; "Fabrication of Microstructured Porous Solids for Applications in Photonics and Biomaterials", Institute of Micro/Nanometer Science & Technology, Shanghai Jiao Tong University, Shanghai, China, July 3, 2003.
- Stein, A.; "Colloidal Crystal Templating of Porous Solids for Applications in Photonics and Beyond", Institute of Fine Chemicals, East China University of Science and Technology, Shanghai, China, July 1, 2003.
- Stein, A.; "Structural Control and Processing of Multifunctional Photonic Crystal Materials Synthesized by Colloidal Crystal Templating", Army Research Laboratory, Aberdeen Proving Grounds, Aberdeen, MD, June 13, 2003.
- Stein, A.; "Colloidal Crystal Templating of Porous Solids for Applications beyond Photonics", Symposium: "Chemical Approaches to Nanostructures and Applications in Photonics, Electronics and Sensing", Spring 2003 MRS Meeting, San Francisco, April 21-24, 2003.
- Stein, A.; "Surface Functionalization of Colloidal-Crystal-Templated Oxides", Symposium: "Synthesis of Nanoparticles and Nanostructured Materials", Spring ACS National Meeting, New Orleans, March 23-27, 2003.
- Stein, A.; "Designing Porous Structures by Colloidal Crystal Templating—Materials for Photonics and Beyond", Second Japan-America Frontiers of Engineering Symposium, National Academy of Engineering, Tokyo, Japan, Oct. 24-26, 2002.
- Stein, A.; "Designing Porous Structures by Colloidal Crystal Templating—Materials for Photonics and Beyond", University of British Columbia, Department of Chemistry, Vancouver, Canada, Oct. 8, 2002.
- Stein, A.; "Designing Porous Structures by Colloidal Crystal Templating—Materials for Photonics and Beyond", University of Minnesota, Department of Chemistry, Minneapolis, MN, Sept. 30, 2002.

- Stein, A.; "Design and Applications of Functionalized Porous Solids Prepared by Colloidal Crystal Templating", Royal Society of Chemistry Materials Discussion on "Porous Materials and Molecular Intercalation" (MD5), Madrid, Spain, Sept. 22-25, 2002.
- Stein, A.; "Colloidal Crystal Templating of Macroporous Metal Oxides", IPRIME Workshop on Photonics: Science and Application, Minneapolis, MN, May 28-29, 2002.
- Stein, A.; "Colloidal Crystal Templating of Macroporous Materials", University of Washington, Seattle, WA, May 14, 2002.
- Stein, A.; "Control of Surface Functionality in Templated Macroporous Oxides", Spring 2002 MRS Meeting, San Francisco, April 3, 2002.

13. Scientific personnel supported:

Professor Andreas Stein (PI)
Dr. Hongwei Yan (postdoc)
Mohammed A. Al-Daous (graduate student, Ph.D. 2003)
Justin C. Lytle (graduate student)
Dan Yu (graduate student)
Sergey Sokolov (graduate student, Ph.D. 2003)

Other scientific personnel involved (external support):
Professor Jinheung Kim (Visiting Professor from Korea)
Mari Carmen Carbajo (visiting graduate student from Universidad Complutense de Madrid, Spain, summer 2001)
Rick Schroden, Brian Melde (graduate students)
Nicholas Stein (high school student, not related)
Collaboration with Professor Robert Cook (U of MN, CEMS) and his graduate student Yvete Toivola for nanomechanical measurements.

14. Report of inventions: not applicable

15. Technology transfer: not applicable

16. Bibliography

1.   John, S. & Busch, K. "Photonic bandgap formation and tunability in certain self-organizing systems." *J. Lightwave Technology* **17**, 1931-1943 (1999).

2.   John, S. "Strong Localization of Photons in Certain Disordered Dielectric Superlattices." *Phys. Rev. Lett.* **58**, 2486-2489 (1987).

3.   Yablonovitch, E. "Photonic band-gap structures." *J. Opt. Soc. Am. B* **10**, 283-295 (1993).

4.   Colvin, V. L. "From Opals to Optics: Colloidal Photonic Crystals." *MRS Bull.* **26**, 637-641 (2001).

5.   Yablonovitch, E. "Inhibited Spontaneous Emission in Solid-State Physics and Electronics." *Phys. Rev. Lett.* **58**, 2059-2062 (1987).

6.   Joannopoulos, J. D., Meade, R. D. & Winn, J. N. *Photonic Crystals* (Princeton Univ. Press, Princeton, NJ, 1995).

7.   Blanford, C. F., Schroden, R. C., Al-Daous, M. & Stein, A. "Tuning Solvent-Dependent Color Changes of Three-Dimensionally Ordered Macroporous (3DOM) Materials Through Compositional and Geometric Modifications." *Adv. Mater.* **13**, 26-29 (2001).

8.   Schroden, R. C., Al-Daous, M., Blanford, C. F. & Stein, A. "Optical Properties of Inverse Opal Photonic Crystals." *Chem. Mater.* **14**, 3305-3315 (2002).

9.   Xia, Y., Gates, B., Yin, Y. & Lu, Y. "Monodispersed Colloidal Spheres: Old Materials with New Applications." *Adv. Mater.* **12**, 693-713 and references therein (2000).

10.   Míguez, H., Mesguer, F., López, C., Blanco, A., Moya, J. S., Requena, J., Mifsud, A. & Fornés, V. "Control of the Photonic Crystal Properties of fcc-Packed Submicrometer SiO_2 Spheres by Sintering." *Adv. Mater.* **10**, 480-483 (1998).

11.   Pieranski, P. "Colloidal Crystals." *Contemp. Phys.* **24**, 25-73 (1983).

12.   Davis, K. E., Russel, W. B. & Glantschnig, W. J. "Settling Suspensions of Colloidal Silica: Observations and X-Ray Measurements." *J. Chem. Soc., Faraday Trans.* **87**, 411-424 (1991).

13.   Mayoral, R., Requena, J., Moya, J. S., López, C., Cintas, A., Míguez, H., Meseguer, F., Vázquez, L., Holgado, M. & Blanco, A. "3D Long-Range Ordering in an SiO_2 Submicrometer-Sphere Sintered Superstructure." *Adv. Mater.* **9**, 257-260 (1997).

14.   Zakhidov, A. A., Baughman, R. H., Iqbal, Z., Cui, C., Khayrullin, I., Dantas, S. O., Marti, J. & Ralchenko, V. G. "Carbon Structures with Three-Dimensional Periodicity at Optical Wavelengths." *Science* **282**, 897-901 (1998).

15.   Velev, O. D., Jede, T. A., Lobo, R. F. & Lenhoff, A. M. "Porous silica via colloidal crystallization." *Nature* **389**, 447-448 (1997).

16.   Velev, O. D., Jede, T. A., Lobo, R. F. & Lenhoff, A. M. "Microstructured Porous Silica Obtained via Colloidal Crystal Templates." *Chem. Mater.* **10**, 3597-3602 (1998).

17.   Holland, B. T., Blanford, C. F. & Stein, A. "Synthesis of Macroporous Minerals with Highly Ordered Three-Dimensional Arrays of Spheroidal Voids." *Science* **281**, 538-540 (1998).

18.   Wijnhoven, J. E. G. J. & Vos, W. L. "Preparation of Photonic Crystals Made of Air Spheres in Titania." *Science* **281**, 802-804 (1998).

19.   Tsunekawa, S., Barnakov, Y. A., Poborchii, V. V., Samoilovich, S. M., Kasuya, A. & Nishina, Y. "Characterization of Precious Opals: AFM and SEM observations, photonic band gap, and incorporation of CdS nano-particles." *Microporous Materials* **8**, 275-282 (1997).

20.   El-Aasser, M. S. & Robertson, A. A. "An Ultracentrifugation Technique for the Study of Latex Coalescence." *J. Colloid Interface Sci.* **93**, 504-512 (1971).

21.   Efremov, I. F. "Periodic Colloid Structures." in *Surface and Colloid Science* (ed. Matijevic, E.) 85-192 (Wiley, New York, 1976).

22.   Holgado, M., García-Santamaría, F., Blanco, A., Ibisate, M., Cintas, A., Míguez, H., Serna, C. J., Molpeceres, C., Requena, J., Mifsud, A., Meseguer, F. & López, C. "Electrophoretic Deposition to Control Artificial Opal Growth." *Langmuir* **15**, 4701-4704 (1999).

23.   Trau, M., Saville, D. A. & Aksay, I. A. "Field-Induced Layering of Colloidal Crystals." *Science* **272**, 706-709 (1996).

24.   Trau, M., Saville, D. A. & Aksay, I. A. "Assembly of Colloidal Crystals at Electrode Interfaces." *Langmuir* **13**, 6375-6381 (1997).

25.   Zhu, J., Li, M., Rogers, R., Meyer, W., Ottewill, R. H., Crew, S.-S. S., Russel, W. B. & Chaikin, P. M. "Crystallization of hard-sphere colloids in microgravity." *Nature* **387**, 883-885 (1997).

26.   van Blaaderen, A., Ruel, R. & Wiltzius, P. "Template-directed colloidal crystallization." *Nature* **385**, 321-324 (1997).

27.   Deckman, H. W. & Dunsmuir, J. H. "Natural lithography." *Appl. Phys. Lett.* **41**, 377-379 (1982).

28.   Burmeister, F., Schäfle, C., Keilhofer, B., Bechinger, C., Boneberg, J. & Leiderer, P. "From Mesoscopic to Nanoscopic Surface Structures: Lithography with Colloid Monolayers." *Adv. Mater.* **10**, 495-497 (1998).

29.   Winzer, M., Kleiber, M., Dix, N. & Wiesendanger, R. "Farbrication of nano-dot- and nano-ring-arrays by nanosphere lithography." *Appl. Phys. A* **63**, 617-619 (1996).

30.   Deckman, H. W. & Dunsmuir, J. H. "Applications of surface textures produced with natural lithography." *J. Vac. Sci. Technol. B* **1**, 1109-1112 (1983).

31.   Hulteen, J. C. & Van Duyne, R. P. "Nanosphere lithography: A materials general fabrication process for periodic particle array surfaces." *J. Vac. Sci. Technol. A* **13**, 1553-1558 (1995).

32.   Denkov, N. D., Velev, O. D., Kralchevsky, P. A., Ivanov, I. B., Yoshimura, H. & Nagayama, K. "Mechanism of Formation of Two-Dimensional Crystals from Latex Particles on Substrates." *Langmuir* **8**, 3183-3190 (1992).

33.   Denkov, N. D., Velev, O. D., Kralchevsky, P. A., Ivanov, I. B., Yoshimura, H. & Nagayama, K. "Two-dimensional crystallization." *Nature* **361**, 26 (1993).

34.   Jiang, P., Bertone, J. F., Hwang, K. S. & Colvin, V. L. "Single-Crystal Colloidal Multilayers of Controlled Thickness." *Chem. Mater.* **11**, 2132-2140 (1999).

35.   Bertone, J. F., Jiang, P., Hwang, K. S., Mittleman, D. M. & Colvin, V. L. "Thickness Dependence of the Optical Properties of Ordered Silica-Air and Air-Polymer Photonic Crystals." *Phys. Rev. Lett.* **83**, 300-303 (1999).

36.   Gates, B., Yin, Y. & Xia, Y. "Fabrication and Characterization of Porous Membranes with Highly Ordered Three-Dimensional Periodic Structures." *Chem. Mater.* **11**, 2827-2836 (1999).

37.   Gates, B., Qin, D. & Xia, Y. "Assembly of Nanoparticles into Opaline Structures over Large Areas." *Adv. Mater.* **11**, 466-469 (1999).

38.   Yang, P., Deng, T., Zhao, D., Feng, P., Pine, D., Chmelka, B. F., Whitesides, G. M. & Stucky, G. D. "Hierarchically Ordered Oxides." *Science* **282**, 2244-2246 (1998).

39.   "Special issue on photonic crystals." *Special Issue on Photonic Crystals: Adv. Mater.* **13**, 369-450 (2001).

40.   Velev, O. D. & Lenhoff, A. M. "Colloidal crystals as templates for porous materials." *Current Opinion in Colloid & Interface Science* **5**, 56-63 (2000).

41.   Velev, O. D. & Kaler, E. W. "Structured porous materials via colloidal crystal templating: From inorganic oxides to metals." *Adv. Mater.* **12**, 531-534 (2000).

42.   Park, S. H. & Xia, Y. "Macroporous membranes with highly ordered and three-dimensionally interconnected spherical pores." *Adv. Mater.* **10**, 1045-1048 (1998).

43.   Blanford, C. F., Yan, H., Schroden, R. C., Al-Daous, M. & Stein, A. "Gems of Chemistry and Physics: Three-Dimensionally Ordered Macroporous (3DOM) Metal Oxides." *Adv. Mater.* **13**, 401-407 (2001).

44.   Stein, A. "Sphere Templating Methods for Periodic Porous Solids." *Micropor. Mesopor. Mater.* **44-45**, 227-239 (2001).

45.   Xia, Y., Gates, B. & Li, Z. Y. "Self-Assembly Approaches to Three-Dimensional Photonic Crystals." *Adv. Mater.* **13**, 409-413 (2001).

46.   Kulinowski, K. M., Jiang, P., Vaswani, H. & Colvin, V. L. "Porous Metals from Colloidal Templates." *Adv. Mater.* **12**, 833-838 (2000).

47.   Norris, D. J. & Vlasov, Y. A. "Chemical Approaches to Three-Dimensional Semiconductor Photonic Crystals." *Adv. Mater.* **13**, 371-376 (2001).

48.   Holland, B. T., Blanford, C. F., Do, T. & Stein, A. "Synthesis of Highly Ordered, Three-Dimensional, Macroporous Structures of Amorphous or Crystalline Inorganic Oxides, Phosphates, and Hybrid Composites." *Chem. Mater.* **11**, 795-805 (1999).

49.   Blanford, C. F., Do, T. N., Holland, B. T. & Stein, A. "Synthesis of Highly Ordered Macroporous Minerals: Extension of the Synthetic Method to other Metal Oxides and Organic-Inorganic Composites." in *Mater. Res. Soc. Symp. Proc.* (eds. Lednor, P. W., Nagaki, D. A. & Thompson, L. T.) 61-66 (MRS, Pittsburgh, 1999).

50.   McComb, D. W., Treble, B. M., Smith, C. J., De La Rue, R. M. & Johnson, N. P. "Synthesis and characterization of photonic crystals." *J. Mater. Chem.* **11**, 142-148 (2001).

51.   Yin, J. S. & Wang, Z. L. "Template-assisted Self-assembly and Cobalt Doping of Ordered Mesoporous Titania Nanostructures." *Adv. Mater.* **11**, 469-472 (1999).

52.   Yan, H., Blanford, C. F., Holland, B. T., Smyrl, W. H. & Stein, A. "General Synthesis of Periodic Macroporous Solids by Templated Salt Precipitation and Chemical Conversion." *Chem. Mater.* **12**, 1134-1141 (2000).

53.   Richel, A., Johnson, N. P. & McComb, D. W. "Observation of Bragg reflection in photonic crystals synthesized from air spheres in a titania matrix." *Appl. Phys. Lett.* **76**, 1816-1818 (2000).

54.   Gundiah, G. & Rao, C. N. R. "Macroporous oxide materials with three-dimensionally interconnected pores." *Solid State Sciences* **2**, 877-882 (2000).

55.   Lei, Z. B., Li, J. M., Zhang, Y. G. & Lu, S. M. "Fabrication and characterization of highly-ordered periodic macroporous barium titanate by the sol-gel method." *J. Mater. Chem.* **10**, 2629-2631 (2000).

56.   Braun, P. V. & Wiltzius, P. "Electrochemically grown photonic crystals." *Nature* **402**, 603-604 (1999).

57.   Braun, P. V. & Wiltzius, P. "Electrochemical Fabrication of 3D Microperiodic Porous Materials." *Adv. Mater.* **13**, 482-485 (2001).

58.   Vlasov, Y. A., Yao, N. & Norris, D. J. "Synthesis of Photonic Crystals for Optical Wavelengths from Semiconductor Quantum Dots." *Adv. Mater.* **11**, 165-169 (1999).

59.   Jiang, P., Cizeron, J., Bertone, J. F. & Colvin, V. L. "Preparation of Macroporous Metal Films from Colloidal Crystals." *J. Am. Chem. Soc.* **121**, 7957-7958 (1999).

60.   Yan, H., Blanford, C. F., Holland, B. T., Parent, M., Smyrl, W. H. & Stein, A. "A Chemical Synthesis of Periodic Macroporous NiO and Metallic Ni." *Adv. Mater.* **11**, 1003-1006 (1999).

61.   Velev, O. D., Tessier, P. M., Lenhoff, A. M. & Kaler, E. W. "A class of porous metallic nanostructures." *Nature* **401**, 548 (1999).

62.   Blanco, A., Chomski, E., Grabtchak, S., Ibisate, M., John, S., Leonard, S. W., Lopez, C., Meseguer, F., Miguez, H., Mondia, J. P., Ozin, G. A., Toader, O. & van Driel, H. M. "Large-scale synthesis of a silicon photonic crystal with a complete three-dimensional bandgap near 1.5 micrometres." *Nature* **405**, 437-440 (2000).

63.   Tessier, P. M., Velev, O. D., Kalambur, A. T., Rabolt, J. F., Lenhoff, A. M. & Kaler, E. W. "Assembly of Gold Nanostructured Films Templated by Colloidal Crystals and Use in Surface-Enhanced Raman Spectroscopy." *J. Am. Chem. Soc.* **122**, 9554-9555 (2000).

64.   Tessier, P. M., Velev, O. D., Kalambur, A. T., Lenhoff, A. M., Rabolt, J. F. & Kaler, E. W. "Structured Metallic Films for Optical and Spectroscopic Applications via Colloidal Crystal Templating." *Adv. Mater.* **13**, 396-400 (2001).

65.   Wijnhoven, J. E. G. J., Zenvenhuizen, S. J. M., Hendriks, M. A., Vanmaekelbergh, D., Kelly, J. J. & Vos, W. L. "Electrochemical Assembly of Ordered Macropores in Gold." *Adv. Mater.* **12**, 888-890 (2000).

66.   Yan, H., Blanford, C. F., Smyrl, W. H. & Stein, A. "Preparation and Structure of 3D Ordered Macroporous Alloys by PMMA Colloidal Crystal Templating." *Chem. Commun.*, 1477-1478 (2000).

67.   Míguez, H., Meseguer, F., López, C., Holgado, M., Andreasen, G., Mifsud, A. & Fornés, V. "Germanium FCC Structure from a Colloidal Crystal Template." *Langmuir* **16**, 4405-4408 (2000).

68.   Park, S. H. & Xia, Y. "Fabrication of Three-Dimensional Macroporous Membranes with Assemblies of Microspheres as Templates." *Chem. Mater.* **10**, 1745-1747 (1998).

69.   Johnson, S. A., Ollivier, P. J. & Mallouk, T. E. "Ordered Mesoporous Polymers of Tunable Pore Size from Colloidal Silica Templates." *Science* **283**, 963-965 (1999).

70.   Jiang, P., Hwang, K. S., Mittleman, D. M., Bertone, J. F. & Colvin, V. L. "Template-Directed Preparation of Macroporous Polymers with Oriented and Crystalline Arrays of Voids." *J. Am. Chem. Soc.* **121**, 11630-11637 (1999).

71.   Deutsch, M., Vlasov, Y. A. & Norris, D. J. "Conjugated-Polymer Photonic Crystals." *Adv. Mater.* **12**, 1176-1180 (2000).

72.   Míguez, H., Meseguer, F., López, C., López-Tejeira, F. & Sánchez-Dehesa, J. "Synthesis and Photonic Bandgap Characterization of Polymer Inverse Opals." *Adv. Mater.* **13**, 393-396 (2001).

73.   Xu, T. B., Cheng, Z. Y., Zhang, Q. M., Baughman, R. H., Cui, C., Zakhidov, A. A. & Su, J. "Fabrication and characterization of three-dimensional periodic ferroelectric polymer-silica opal composites and inverse opals." *J. Appl. Phys.* **88**, 405-409 (2000).

74.   Yoshino, K., Kawagishi, Y., Tatsuhara, S., Kajii, H., Lee, S., Fujii, A., Ozaki, M., Zakhidov, A. A., Vardeny, Z. V. & Ishikawa, M. "Optical properties of conducting polymers in nano-scale periodic structure, microcavities and photonic crystals." *Microelectronic Engineering* **47**, 49-53 (1999).

75.   Schroden, R. C. & Stein, A. "3D Ordered Macroporous Materials." in *Colloids and Colloid Assemblies: Synthesis, Modification, Organization and Utilization of Colloid Particles* (ed. Caruso, F.) 465-493 (Wiley-VCH, Weinheim, 2004).

76.   Al-Daous, M. A. & Stein, A. "Preparation and catalytic evaluation of macroporous crystalline sulfated zirconium dioxide templated with colloidal crystals." *Chem. Mater.* **15**, 2638-2645 (2003).

77.   Holland, B. T., Abrams, L. & Stein, A. "Dual templating of macroporous silicates with zeolitic microporous frameworks." *J. Am. Chem. Soc.* **121**, 4308-4309 (1999).

78.   Sokolov, S., Bell, D. & Stein, A. "Preparation and Characterization of Macroporous alpha-Alumina." *J. Am. Ceram. Soc.* **86**, 1481-1486 (2003).

79.   Sokolov, S. & Stein, A. "Preparation and Characterization of Macroporous Gamma-LiAlO$_2$." *Materials Letters* **57**, 3593-3597 (2003).

80.   Jun, S., Joo, S. H., Ryoo, R., Kruk, M., Jaroniec, M., Liu, Z., Ohsuna, T. & Terasaki, O. "Synthesis of New, Nanoporous Carbon with Hexagonally Ordered Mesostructure." *J. Am. Chem. Soc.* **2000**, 10712-10713 (2000).

81.   Kim, S. S. & Pinnavaia, T. J. "A low cost route to hexagonal mesostructured carbon molecular sieves." *Chem. Commun.*, 2418-2419 (2001).

82.   Li, Z. J. & Jaroniec, M. "Colloidal imprinting: A novel approach to the synthesis of mesoporous carbons." *J. Am. Chem. Soc.* **123**, 9208-9209 (2001).

83.   Li, Z. J., Jaroniec, M., Lee, Y. J. & Radovic, L. R. "High surface area graphitized carbon with uniform mesopores synthesized by a colloidal imprinting method." *Chem. Commun.*, 1346-1347 (2002).

84.   Lukens, W. W. & Stucky, G. D. "Synthesis of mesoporous carbon foams templated by organic colloids." *Chem. Mater.* **14**, 1665-1670 (2002).

85.   Thijssen, M. S., Sprik, R., Wijnhoven, J. E. G. J., Megens, M., Narayanan, T., Lagendijk, A. & Vos, W. L. "Inhibited Light Propagation and Broadband Reflection in Photonic Air-Sphere Crystals." *Phys. Rev. Lett.* **83**, 2730-2733 (1999).

86.   Patton, T. C. (ed.) *Pigment Handbook* (Wiley, N.Y., 1973).

87.   Heald, E. F. & Weiss, C. W. *Am. Miner.* **57**, 10 (1972).

88.   Yoldas, B. E. "Hydrolysis of titanium alkoxide and effects of hydrolytic polycondensation parameters." *J. Mater. Sci.* **21**, 1087-1092 (1986).

89.   Ding, X., Liu, L., Ma, X., Qi, Z. & He, Y. *J. Mater. Sci. Lett.* **13**, 462 (1994).

90.   Bokhimi, X., Morales, A., Novaro, O., Lopaz, T., Sanchez, E. & Gomez, R. *J. Mater. Res.* **10**, 2788 (1995).

91.   Sanchez, E., Lopez, T., Gomez, R., Bokhimi, X., Morales, A. & Novaro, O. *J. Solid State Chem.* **122**, 309 (1996).

92.   Kumar, K. N. P., Keizer, K. & Burggraaf, A. J. *J. Mater. Sci. Lett.* **13**, 59 (1994).

93.   Bokhimi, X., Morales, A., Novaro, O., Lopez, T., Chimal, O., Asomoza, M. & Gomez, R. *Chem. Mater.* **9**, 2616 (1997).

94.   Kumar, K. N., Keizer, K., Burggraaf, A. J., Okubo, T. & Nagamoto, H. *J. Mater. Chem.* **3**, 923 (1993).

95.   Cheng, H., Ma, J., Zhao, Z. & Qi, L. *Chem. Mater.* **7**, 663 (1995).

96.   Arnal, P., Corriu, R. J. P., Lechercq, D., Mutin, P. H. & Vioux, A. *J. Mater. Chem.* **6**, 1925 (1996).

97.   Möckel, H., Giersig, M. & Willig, F. "Formation of uniform size anatase nanocrystals from bis(ammonium lactato) titanium dihydroxide by thermohydrolysis." *J. Mater. Chem.* **9**, 3051-3056 (1999).

98.   Greenstein, L. M. "Pearlescence." in *Pigment Handbook* (ed. Patton, T. C.) 357-390 (Wiley, New York, 1973).

99.   Armanini, L. & Mattin, H. L. "Three Color Effects From Interference Pigments." in *Coloring Technology for Plastics* (ed. Harris, R. M.) 21-33 (Plastics Design Library, Norwich, NY, 1999).

100.   Harris, R. M. *Coloring Technology for Plastics* (Plastics Design Library, Norwich, NY, 1999).

101.   Zachariasen, W. H. *Theory of X-ray Diffraction in Crystals* (John Wiley and Sons, New York, 1946).

102.   Rundquist, P. A., Photinos, P., Jagannathan, S. & Asher, S. A. "Dynamical Bragg diffraction from crystalline colloidal arrays." *J. Chem. Phys.* **91**, 4932-4941 (1989).

103.   Kesavamoorthy, R., Tandon, S., Xu, S., Jagannathan, S. & Asher, S. A. "Self-Assembly and Ordering of Electrostatically Stabilized Silica Suspensions." *J. Colloid Interface Sci.* **153**, 188-198 (1992).

104.   Liu, L., Li, P. & Asher, S. A. "Fortuitously Superimposed Lattice Plane Secondary Diffraction from Crystalline Colloidal Arrays." *J. Am. Chem. Soc.* **119**, 2729-2732 (1997).

105.   Spry, R. J. & Kosan, D. J. "Theoretical Analysis of the Crystalline Colloidal Array Filter." *Appl. Spectrosc.* **40**, 782-784 (1986).

106.   Mittleman, D. M., Bertone, J. F., Jiang, P., Hwang, K. S. & Colvin, V. L. "Optical properties of planar colloidal crystals: Dynamical diffraction and the scalar wave approximation." *J. Chem. Phys.* **111**, 345-354 (1999).

107.   Van de Hulst, H. C. *Light Scattering by Small Particles* (John Wiley and Sons, New York, 1957).

108.   Vos, W. L., Sprik, R., van Blaaderen, A., Imhof, A., Lagendijk, A. & Wegdam, G. H. "Strong effects of photonic band structures on the diffraction of colloidal crystals." *Phys. Rev. B* **53**, 16231-16235 (1996).

109.   Míguez, H., Yang, S. M. & Ozin, G. A. "Colloidal photonic crystal microchannel array with periodically modulated thickness." *Appl. Phys. Lett.* **81**, 2493-2495 (2002).

110.   Astratov, V. N., Adawi, A. M., Fricker, S., Skolnick, M. S., Whittaker, D. M. & Pusey, P. N. "Interplay of order and disorder in the optical properties of opal photonic crystals." *Phys. Rev. B* **66**, 165215/165211-165215/165213 (2002).

111.   Campbell, M., Sharp, D. N., Harrison, M. T., Denning, R. G. & Turberfield, A. J. "Fabrication of photonic crystals for the visible spectrum by holographic lithography." *Nature* **404**, 53-56 (2000).

112.   Vlasov, Y. A., Astratov, V. N., Baryshev, A. V., Kaplyanskii, A. A., Karimov, O. Z. & Limonov, M. F. "Manifestation of intrinsic defects in optical properties of self-organized opal photonic crystals." *Phys. Rev. E* **61**, 5784-5793 (2000).

113.   Goldenberg, L. M., Wagner, J., Stumpe, J., Paulke, B. R. & Görnitz, E. "Optical properties of ordered arrays of large latex particles." *Physica E* **17**, 433-435 (2003).

114.   Schroden, R. C., Al-Daous, M., Sokolov, S., Melde, B. J., Lytle, J. C., Stein, A., Carbojo, M. C., Fernández, J. T. & Rodríguez, E. E. "Hybrid Macroporous Materials for Heavy Metal Ion Adsorption." *J. Mater. Chem.* **12**, 3261-3267 (2002).

115. Vohra, M. S. & Davis, A. P. "Adsorption of Pb(II), NTA, and Pb(II)-NTA onto TiO2." *J. Colloid Interfac. Sci.* **194**, 59-67 (1997).

116. Naber, J., de Jong, K., Stork, W., Kuipers, H. & Post, M. "Industrial applications of zeolite catalysis." *Stud. Surf. Sci. Catal.* **84**, 2197-2219 (1994).

117. Caruso, F. "Nanoengineering of Particle Surfaces." *Adv. Mater.* **13**, 11-22 and references therein (2001).

118. Wang, X. D., Yang, W. L., Tang, Y., Wang, Y., Fu, S. K. & Gao, Z. "Fabrication of hollow zeolite spheres." *Chem. Commun.*, 2161-2162 (2000).

119. Rhodes, K. H., Davis, S. A., Caruso, F., Zhang, B. & Mann, S. "Hierarchical Assembly of Zeolite Nanoparticles into Ordered Macroporous Monoliths Using Core—Shell Building Blocks." *Chem. Mater.* **12**, 2832-2834 (2000).

120. Kuba, S., Lukinskas, P., Grasselli, R. K., Gates, B. C. & Knözinger, H. J. "Structure and properties of tungstated zirconia catalysts for alkane conversion." *J. Catal.* **216**, 353-361 (2003).

121. Caruso, F., Caruso, R. A. & Möhwald, H. "Nanoengineering of Inorganic and Hybrid Hollow Spheres by Colloidal Templating." *Science* **282**, 1111-1114 (1998).

122. Melde, B. J. & Stein, A. "Periodic Macroporous Hydroxyapatite-containing Calcium Phosphates." *Chem. Mater.* **14**, 3326-3331 (2002).

123. Mi-seon, S., Sun, I. K., Nam, G. K., Chul, G. S. & Seon, J. K. *J. Appl. Polym. Sci.* **84**, 2591-2596 (2001).

124. Norman, F., Sheppard, J. R., Robert, C. T. & Samira, S. *Sensors and Actuators B* **10**, 73-77 (1993).

125. Shiel, L. Y. & Peppas, N. A. *J. Appl. Polym. Sci.* **42**, 1579-1587 (1991).

126. Matyjaszewski, K. & Xia, J. "Atom Transfer Radical Polymerization." *Chem. Rev.* **101**, 2921-2990 (2001).

127. Toivola, Y., Stein, A. & Cook, R. F. "Depth-Sensing Indentation Response of Ordered Silica Foam." *J. Mater. Res.* **19**, 260-271 (2004).

128. Kosaka, H., Kawashima, T., Tomita, A., Notomi, M., Tamamura, T., Sato, T. & Kawakami, S. "Superprism Phenomena in Photonic Crystals." *Phys. Rev. B* **58**, R10096-R10099 (1998).

129. Mekis, A., Chen, J. C., Kurland, I., Fan, S., Villeneuve, P. R. & Joannopoulos, J. D. "High Transmission through Sharp Bands in Photonic Crystal Waveguides." *Phys. Rev. Lett.* **77**, 3787-3790 (1996).

130. Nishimura, S., Abrams, N., Lewis, B. A., Halaoui, L. I., Mallouk, T. E., Benkstein, K. D., Van De Lagemaat, J. & Frank, A. J. "Standing Wave Enhancement of Red Absorbance and Photocurrent in Dye-Sensitive Titanium Dioxide Photoelectrodes Coupled to Photonic Crystals." *J. Am. Chem. Soc.* **125**, 6306-6310 (2003).

131. Purcell, E. M. "Spontaneous Emission Probabilities at Radio Frequencies." *Phys. Rev.* **69**, 681 (1946).

132. Schriemer, H. P., van Driel, H. M., Koenderink, A. F. & Vos, W. L. "Modified spontaneous emission spectra of laser dye in inverse opal photonic crystals." *Phys. Rev. A* **63**, 011801-011801-011804 (2000).

133. Blanco, A., López, C., Mayoral, R., Míguez, H. & Meseguer, F. "CdS photoluminescence inhibition by a photonic structure." *Appl. Phys. Lett.* **73**, 1781-1783 (1998).

134. Barnett, S. M. & Loudon, R. "Sum Rule for Modified Spontaneous Emission Rates." *Phys. Rev. Letters* **77**, 2444-2446 (1996).

135.   Vlasov, Y. A., Luterova, K., Pelant, I., Hönerlage, B. & Astratov, V. N. "Enhancement of optical gain of semiconductor embedded in three-dimensional photonic crystal." *Appl. Phys. Lett.* **71**, 1616-1618 (1997).

136.   Eradat, N., Huang, J. D., Vardeny, Z. V., Zakhidov, A. A., Khayrullin, I., Udod, I. & Baughman, R. H. "Optical studies of metal-infiltrated opal photonic crystals." *Synth. Metals* **116**, 501-504 (2001).

137.   Solovyev, V. G., Romanov, S. G., Sotomayor-Torres, C. M., Müller, M., Zentel, R., Gaponik, N., Eychmüller, A. & Rogach, A. L. "Modification of the spontaneous emission of CdTe nanocrystals in TiO$_2$ inverted opals." *J. Appl. Phys.* **94**, 1205-1210 (2003).

138.   Romanov, S. G., Maka, T., Torres, C. M. S., Müller, M. & Zentel, R. "Light emission from thin opaline photonic crystals of low and high dielectric contrast." *Synth. Metals* **124**, 131-135 (2001).

139.   Romanov, S. G., Fokin, A. V. & De La Rue, R. M. "Anisotropic photoluminescence in incomplete three-dimensional photonic band-gap environments." *Appl. Phys. Lett.* **74**, 1821-1823 (1999).

140.   Suzuki, T. & Yu, P. K. L. "Emission power of an electric dipole in the photonic band structure of the fcc lattice." *J. Opt. Soc. Am. B* **12**, 570-582 (1995).

141.   Kamat, P. V. "Photochemistry on nonreactive and reactive (semiconductor) surfaces." *Chem. Rev.* **93**, 267-300 (1993).

142.   Kalyanasundaram, K., Grätzel, M. & Pelizzetti, E. "Interfacial electron transfer in colloidal metal and semiconductor dispersions and photodecomposition of water." *Coord. Chem. Rev.* **69**, 57-125 (1986).

143.   Vos, W. L. & Polman, A. "Optical Probes Inside Photonic Crystals." *MRS Bulletin* **26**, 642-646 (2001).

144.   Anpo, M., Nakaya, H., Kodama, S., Kubokawa, Y., Domen, K. & Onishi, T. "Photocatalysis over Binary Metal Oxides. Enhancement of the Photocatalytic Activity of TiO2 in Titanium-Silicon Oxides." *J. Phys. Chem.* **90**, 1633-1636 (1986).

145.   Miyashita, K., Kuroda, S., Tajima, S., Takehira, K., Tobita, S. & Kubota, H. "Photoluminescence study of electron-hole recombination dynamics in the vacuum deposited SiO$_2$/TiO$_2$ multilayer film with photocatalytic activity." *Chem. Phys. Lett.* **369**, 225-231 (2003).

146.   Yoldas, B. E. "Formation of titania-silica glasses by low temperature chemical polymerization." *J. Non-Cryst. Solids* **38/39**, 81-86 (1980).

147.   Linsebigler, A. L., Lu, G. & Yates, J. T. "Photocatalysis on TiO$_2$ Surfaces: Principles, Mechanisms, and Selected Results." *Chem. Rev.* **95**, 735-758 (1995).

148.   Anderson, C. & Bard, A. J. "An Improved Photocatalyst of TiO$_2$/SiO$_2$ Prepared by a Sol-Gel Synthesis." *J. Phys. Chem.* **99**, 9882-9885 (1995).

149.   Tada, H., Akazawa, M., Kubo, Y. & Ito, S. "Enhancing Effect of SiO$_X$ Monolayer Coverage of TiO$_2$ on the Photoinduced Oxidation of Rhodamine 6G in Aqueous Media." *J. Phys. Chem. B* **102**, 6360-6366 (1998).

150.   Schraml-Marth, M., Walther, K. L., Wokaun, A., Handy, B. E. & Baiker, A. "Porous silica gels and titania/silica mixed oxides prepared via the sol-gel process: characterization by spectroscopic techniques." *J. Non-Cryst. Solids* **143**, 93-111 (1992).

151.   Liu, Z. & Davis, R. J. "Investigation of the Structure of Microporous Ti-Si Mixed Oxides by X-ray, UV Reflectance, FT-Raman, and FT-IR Spectroscopies." *J. Phys. Chem.* **98**, 1253-1261 (1994).

152.   Anpo, M., Suzuki, T., Kubokawa, Y., Tanaka, F. & Yamashita, S. "Photoluminescence evidence for the influence of symmetry of molybdenum ions upon photocatalytic activity." *J. Phys. Chem.* **88**, 5778-5779 (1984).

153.   Anpo, M., Aikawa, N., Kubokawa, Y., Che, M., Louis, C. & Giamello, E. "Photoluminescence and Photocatalytic Activity of Highly Dispersed Titanium Oxide Anchored onto Porous Vycor Glass." *J. Phys. Chem.* **89**, 5017-5021 (1985).

154.   Pruden, A. L. & Ollis, D. F. "Photoassisted heterogeneous catalysis: the degradation of trichloroethylene in water." *J. Catal.* **82**, 404-417 (1983).

155.   Hench, L. L. *J. Am. Ceram. Soc.* **81**, 1705 (1998).

156.   Zhang, K., Yan, H., Bell, D. C., Stein, A. & Francis, L. F. "Effects of Materials Parameters on Mineralization and Degradation of Sol-gel Bioactive Glasses with 3D-ordered Macroporous (3DOM) Structures." *J. Biomed. Mater. Res.* **66A**, 860-869 (2003).